# FROM DUSTY TO DUST-FREE: PANCHROMATIC EXTREME STAR FORMATION IN INTERMEDIATE- TO HIGH-REDSHIFT GALAXIES

By

Logan H. Jones

A dissertation submitted in partial fulfillment of the requirements for the degree of

Doctor of Philosophy
(Astronomy)

at the

UNIVERSITY OF WISCONSIN-MADISON

2021

Date of final oral examination: 6 August 2021

The dissertation is approved by the following members of the Final Oral Committee:
Amy Barger, Professor, Astronomy
Christy Tremonti, Associate Professor, Astronomy
Elena D'Onghia, Associate Professor, Astronomy
Ke Zhang, Assistant Professor, Astronomy
Keith Bechtol, Assistant Professor, Physics

### Abstract

The creation of new stars from cold gas is one of the most fundamental astrophysical processes that can be observed in our own galaxy and in others. At a broad level, the modern phenomenological picture of how stars form is consistent with observations of systems ranging from nearby molecular clouds to the most distant galaxies. Many gaps and limitations in the details of such a picture, however, remain unfilled and unanswered. For example, questions remain about the interplay between star formation and chemical enrichment in blue, metal-poor galaxies and the impact of that relationship in cosmic reionization – one of the final frontiers of observational extragalactic astrophysics. Meanwhile, on the other end of the electromagnetic and metallicity spectrum, there exists a population of high-redshift, far-infrared-bright, and heavily dust-obscured starbursting galaxies that represent a fleeting but possibly integral stage in the growth of massive galaxies and of dense, large-scale structures like (proto)clusters of galaxies. However, the mechanism(s) that trigger such starbursts, especially in dense environments, remains ambiguous.

The research that comprises this dissertation aims to answer two questions that, while both relevant to astronomers' understanding of the birth and evolution of galaxies in the broadest sense, are largely disjoint from one another. These questions are: 1) What are the intermediate- to high-redshift analogs to the sources that reionized the universe at very early times?; and 2) As a function of redshift and/or environment, how common are

massively star-forming, dust-obscured galaxies?

Because these questions are so different from one another, this dissertation will be split into two major parts. In the first, I present a search in two legacy fields (the GOODS-North and the GOODS-South) for galaxies at high redshift that may be sources of ionizing ultraviolet photons. Such objects are expected to be analogs, in various ways, to the first generation of galaxies, and thus provide clues to the nature of very-high-redshift galaxies that will be discovered en masse by future ground- and space-based observatories. In the second part, I present the spectroscopic confirmation of an overdensity of dusty starbursting galaxies at  $z \approx 3.14$ , signposting a protocluster of galaxies near the peak of star formation activity in the universe. Compared to similar recent discoveries in the literature, this new protocluster is relatively late-forming and includes several of the most infrared-luminous starbursts currently known. This makes it an excellent laboratory for testing theories of starburst triggering and the subsequent buildup of stellar mass in dense environments. In the final chapter of this dissertation, I reiterate the key results of the research presented in chapters 2, 3, and 5.

## Contents

	Abs	tract	i
	Con	tents	iii
	List	of Tables	vii
	List	of Figures	viii
	Ack	nowledgments	xi
1	Intr	roduction to the Ultraviolet and Optical High-Redshift Universe	1
	1.1	The Epoch of Reionization (EoR)	1
	1.2	Lyman Continuum Escape	3
	1.3	Sources of Lyman Continuum Flux and Likely Analogs	4
		References	7
2	$z \sim$	2.5 – 3 Ionizers in the GOODS-N Field	13
		Abstract	14
	2.1	Introduction	15
	2.2	Data	19
		2.2.1 F275W Imaging	19
		2.2.2 Optical/NIR Spectroscopy	19
		2.2.3 UV Grism Spectroscopy	20
		2.2.4 X-ray Imaging	91

	2.3	Search	for $z \sim 3$ Candidate LyC Emitters	1
		2.3.1	F275W Sample	1
		2.3.2	Color-Selected Sample	3
		2.3.3	Six Candidate LyC Emitters	4
			2.3.3.1 GN-UVC-1	5
			2.3.3.2 GN-UVC-2	6
			2.3.3.3 GN-UVC-3	9
			2.3.3.4 GN-UVC-4	0
			2.3.3.5 GN-UVC-5	1
			2.3.3.6 GN-UVC-6	1
	2.4	Contri	butions to the Ionizing Flux	2
		2.4.1	Quasar UV Emissivity	3
		2.4.2	Non-quasar UV Emissivity	3
		2.4.3	Comparisons with the Literature	5
	2.5	Summ	ary	6
	A	Staten	nent of Work	9
		Refere	nces	9
3	Can	ndidate	$z\sim 2.5$ Lyman Continuum Sources in the GOODS Fields 40	6
		Abstra	act	7
	3.1	Introd	uction	8
	3.2	Data		2
		3.2.1	F275W Imaging	2
		3.2.2	Optical/NIR Spectroscopy	3
		3.2.3	X-ray Imaging	4

	3.3	Search for Individual $z \sim 3$ Candidate LyC Leakers in the GOODS-S	55
		3.3.1 F275W Measurements in the GOODS-S	56
		3.3.2 Five Candidate LyC Leakers in the GOODS-S	58
	3.4	Mean ionizing emission from an averaging analysis using both GOODS fields	62
	3.5	An Image stacking visualization in both GOODS fields	65
	3.6	Contributions to the Metagalactic Ionizing Background	69
	3.7	Summary	72
	A	Statement of Work	74
		References	74
4	Inti	roduction to the (Sub)-Millimeter High-Redshift Universe	81
	4.1	Phenomenology of Submillimeter Galaxies	81
	4.2	Observational Utility of Submillimeter Galaxies at High Redshift	83
	4.3	Challenges of Observing Submillimeter Galaxies	85
		References	87
5	NO	EMA Redshift Measurements of Extremely Bright Submillimeter	$\mathbf{r}$
	Gal	axies Near the GOODS-N	90
		Abstract	91
	5.1	Introduction	92
	5.2	Data	95
		5.2.1 NOEMA Observations	95
		5.2.2 Multiwavelength Data	97
	5.3	Results	99
	5.4	Discussion	104
		5.4.1 Star Formation Rates, Masses, and Dust Temperatures	104

		6.4.2 Gas Mass and Depletion Timescale
		6.4.3 (Sub)Millimeter Evidence of a Protocluster
		6.4.4 Optical Evidence of a Protocluster
	5.5	Summary
	A	Statement of Work
		References
6	Sun	nary and Future Prospects 11
	6.1	Direct and Indirect Searches for Sources of Ionization
	6.2	A Protocluster of Rare Galaxies at $z = 3.14$
		References 19

# List of Tables

23	Photometric properties of candidate LyC emitters in the GOODS-North .	2.1
60	Photometric properties of candidate LyC emitters in the GOODS-South	3.1
	Error-weighted, summed UV fluxes at the positions of galaxies with	3.2
64	$2.35 < z_{spec} < 3.05$ in the separate and combined GOODS fields	
99	(Sub)millimeter spectral continuum properties of NOEMA targets	5.1
100	(Sub)millimeter spectral line properties of NOEMA targets	5.2
	Physical properties of candidate protocluster members as derived from	5.3
105	spectral energy distribution fitting	

# List of Figures

1.1	Cartoon representation of the chronology of the universe	2
1.2	Optical spectrum of an ultra-strong emission line galaxy in the COSMOS field	5
2.1	B and UV magnitudes vs. spectroscopic redshift for sources in the HDUV	
	GOODS-North	22
2.2	Spectroscopic redshift vs. UV – B color for sources in the HDUV GOODS-	
	North	24
2.4	UV and three-color thumbnails of candidate LyC-emitting objects in the	
	GOODS-North	25
2.5	UV grism spectrum of LyC-luminous AGN GN-UVC-1	26
2.6	Keck/DEIMOS spectrum of candidate LyC emitter GN-UVC-2	27
2.7	UV continuum and [OIII] $\lambda$ 5007 light profiles across GN-UVC-2	28
2.8	Keck/DEIMOS spectrum of candidate LyC emitter GN-UVC-3	29
2.9	Keck/DEIMOS spectrum of candidate LyC emitter GN-UVC-4	30
2.10	Keck/DEIMOS spectrum of candidate LyC emitter GN-UVC-5	32
2.11	Ionizing emissivity vs. redshift with literature comparisons, using only data	
	from the GOODS-North	34

3.1	B and UV magnitudes vs. spectroscopic redshift for sources in the HDUV	
	GOODS-South	55
3.2	Spectroscopic redshift vs. UV – B color for sources in the HDUV GOODS-	
	South	58
3.3	UV and three-color thumbnails of candidate LyC-emitting objects in the	
	GOODS-South	59
3.4	UV flux vs. z magnitude for sources in both GOODS fields	64
3.5	Stacked images of $z > 2.35$ galaxies in the separate and combined GOODS	
	fields	66
3.6	UV flux and mean transmissivity of the intergalactic medium to LyC photons	
	vs. redshift	68
3.7	Ionizing emissivity vs. redshift with literature comparisons, using data from	
	both GOODS-North and South	71
4.1	Observations of the star formation rate density from submillimeter galaxies	82
4.2	Spectral energy distribution of the prototypical dusty starbursting galaxy	
	Arp220	84
4.3	Visualization of atmospheric bands accessible to NOEMA, plus sky frequen-	
	cies of prominent millimeter emission features	86
5.1	SCUBA-2 image of the GOODS-North field, along with $K$ -band images of	
	targeted sources	95
5.2	Full millimeter spectra from NOEMA	98
5.3	Zoom-in of NOEMA spectra with Gaussian fits to strong emission features	101
5.4	Keck/MOSFIRE spectrum of protocluster candidate GN-CL-2	102
5.5	Spectral energy distribution fits of targeted SMGs	106

5.6	Projected source density across the GOODS-North at the redshift of the	
	SMG-rich protocluster	110
6.1	Optical spectrum of an ultra-strong emission line galaxy in the North Ecliptic	
	Pole	123

### Acknowledgments

The list of people to which I owe the privilege of pursuing my astronomy education is too long, and the magnitude of the debt too large, to accurately capture in a brief acknowledgements page, but here I go anyway. Above all, I would not be here without the love and support of my mother Jennifer Jones, my grandfather Larry Jones, and my late grandmother Donna Jones. You did so much when I was young to encourage my desire to learn and have continued to support me in many ways since moving away from home. I will always be grateful, and I love you.

The unwavering companionship of my friends and fellow astronomy students pulled me through coursework, research mental blocks, coffee cravings, fitness journeys, and social shenanigans. Being friends with you all has made me a better person than I was when I moved to Madison. I especially appreciate my partner Melissa, who helped to keep my world spinning during a pandemic that seemed to stop time and who even made my experience of 2020 and 2021 (dare I say it?) happy.

Thank you, as well, to the astronomy faculty whose formal teaching, informal mentorship, and coffee conversations have shown me how far we've come in understanding the Universe, and how much work is still left to be done – and in particular to my advisor Amy Barger, who has provided me with more opportunities than could ever be acted upon in the course of a single PhD program.

Finally, I acknowledge the sacrifices made by the Ho-Chunk, Sauk, Meskwaki, Tohono

O'odham, and Hawaiian peoples, whose lands encompass the spaces where I've lived, where I've worked, and where much of my data were obtained. The sad truth, which I will carry with me for the remainder of my academic career, is that the research I present in this thesis would have been impossible without the theft and colonization of their homes and sacred sites. May this document serve as a reminder to myself – and to all astronomers – to always do what I (we) can to uplift Native voices and repair the harm done to Native people, cultures, and livelihoods in the name of science.

### Chapter 1

# Introduction to the Ultraviolet and Optical High-Redshift Universe

### 1.1 The Epoch of Reionization (EoR)

In many ways, the 8 < z < 20 universe is now the final frontier of extragalactic astronomy. Encompassing the first few hundred Myr of the history of the universe after recombination, it is a critical period for the coalescence of dark matter halos, the start of stellar mass buildup, and the (re)ionization of the vast majority of hydrogen atoms across space. For this reason, the very-high-redshift universe is often referred to as the Epoch of Reionization (EoR) – the era in which the bulk of the intergalactic medium (IGM) was brought from a neutral state to an almost fully ionized one.

The general timeline of reionization is now reasonably constrained and is depicted graphically in Figure 1.1, which illustrates the major periods in the lifetime of the universe. Most evidence points to a scenario in which faint star-forming galaxies (SFGs) produce the majority of hydrogen-ionizing ultraviolet (UV) photons (e.g., Bouwens et al. 2006; Finlator et al. 2009; Fontanot et al. 2014; Robertson et al. 2015; Japelj et al. 2017; Finkelstein et

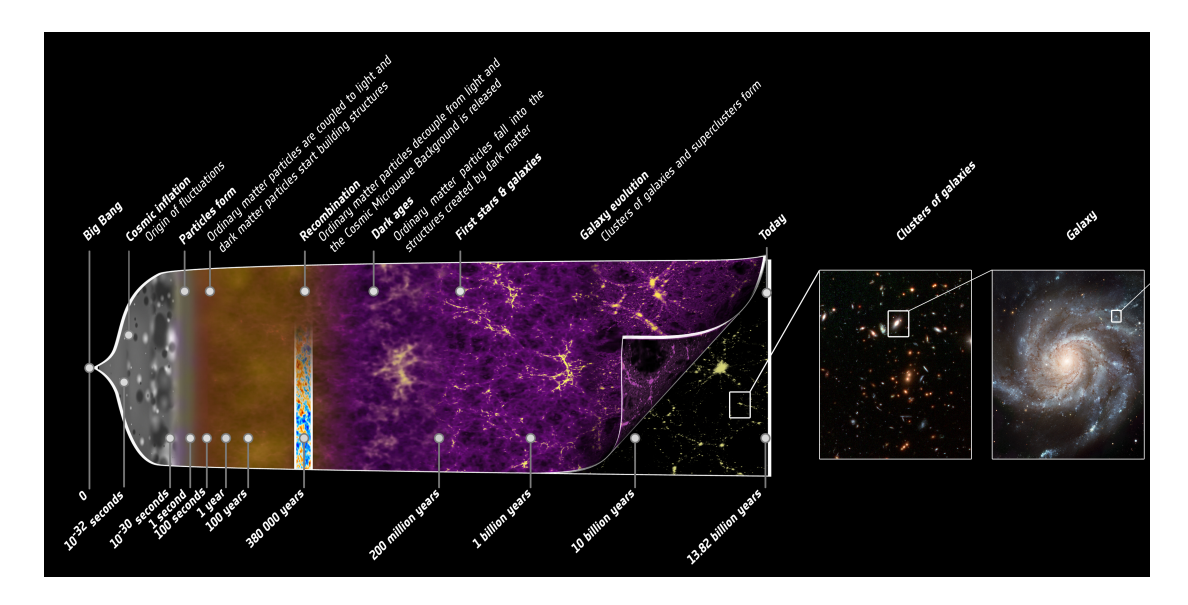


**Figure 1.1**: A graphical representation of major epochs and transitional periods in the history of the universe, reproduced with modifications from an educational post by NASA's *Planck* Project Office. After becoming electrically neutral during recombination, the bulk of baryons in the universe would begin to be reionized as the first stars and galaxies "turn on" 200 million years or so after the Big Bang.

al. 2019). However, some authors have argued that more massive galaxies (Naidu et al. 2020) or active galactic nuclei (AGN, e.g., Fontanot et al. 2012; Madau & Haardt 2015) are dominant or non-negligible contributors to reionization; the plausibility of the AGN scenario will depend on the evolution of AGN number density with redshift (Giallongo et al. 2019; Kulkarni et al. 2019; Cowie et al. 2020; Grazian et al. 2020; Shin et al. 2020).

Even with the most powerful facilities currently available, direct detection and confirmation of galaxies deep into the EoR (z>8) remains exceptionally difficult. For example, Oesch et al. (2018a) compiled over 800 arcmin<sup>2</sup> of deep imaging from the *Hubble* Space Telescope (*HST*) on data-rich legacy fields and only found nine reliable  $z\sim10$  candidates over all of their fields. Similarly, a synthesis of *Spitzer* Space Telescope imaging, near-infrared spectroscopy from Keck, Gemini, and the Very Large Telescopes, and millimeter spectroscopy with the Atacama Large Millimeter Array (ALMA) was able to confirm redshifts for a mere three z>9 candidates (Laporte et al. 2021). The advent

of the James Webb Space Telescope (JWST) and of 30 m-class ground-based observatories will provide much larger samples of EoR galaxies, though much effort is also being directed towards understanding their analogs at  $z \lesssim 3$ , discussed further in the next sections.

### 1.2 Lyman Continuum Escape

Regardless of their production mechanism, reionization of the IGM (or maintaining a highly ionized state) requires that UV photons with energies > 13.6 eV are able to escape their galaxy of origin to interact with intergalactic baryons. Photons in this energy range are referred to as the Lyman continuum (LyC), since they are shorter in wavelength than the Lyman limit at 912 Å. Direct observations of LyC emission remain challenging even for modern facilities and are fundamentally limited by the astrophysics of both the interstellar medium (ISM) and the IGM.

LyC photons are extremely susceptible to absorption by dust, gas-phase metals, and neutral hydrogen. For hydrogen specifically, the probability of absorption rises very quickly as the photon energy approaches 13.6 eV, with the absorption cross section of hydrogen scaling like  $6.8 \times 10^{-18} (E/13.6 \text{eV})^{-3} \text{ cm}^2$  (Wise et al. 2019). Escape of LyC photons requires lines-of-sight through which the HI column density is less than  $10^{17.7} \text{ cm}^2$ ; above this threshold, the ISM of a galaxy becomes optically thick to LyC (Chisholm et al. 2018). Unless their ISM has low-density holes through which LyC photons can travel mostly unhindered, most galaxies are essentially invisible in photometric bands bluer than the redshifted Lyman limit. The level of LyC emission from a galaxy is quantified through the LyC escape fraction  $f_{esc}$ , or the ratio of the observed to the intrinsic LyC luminosity. (Note that the latter quantity is usually estimated from stellar population fitting and therefore quite model-dependent.) Modern models of reionization require a typical  $f_{esc}$  of 10% or greater from SFGs, assuming that SFGs are responsible for most of the LyC photon

production in the early universe (e.g., Vanzella et al. 2012b; Robertson et al. 2015; Feng et al. 2016; Price et al. 2016; Kimm et al. 2017). However, most galaxies in the local universe have escape fractions of, at most, a few percent (Leitherer et al. 1995; Grimes et al. 2009; Rutkowski et al. 2017).

Many lines of evidence show that the IGM was returned to an (almost) fully ionized state no later than z=6 (e.g., Gunn & Peterson 1965; Songaila 2004; Fan et al. 2006; Grieg & Mesinger 2017). However, independent from the problem of LyC escape from individual galaxies is the problem of absorption by residual HI clouds along the line of sight through the IGM. Beyond  $z\sim 3.5-4$ , the column density of HI absorbers rapidly increases, which extinguishes any surviving LyC signal from galaxies above these redshifts (Songaila & Cowie 2010; Inoue et al. 2014). Only a very small number of direct detections of LyC at  $z\sim 4$  have been made to date – for example, the z=3.8 galaxy Ion1 in Ji et al. (2020) and the z=4 galaxy Ion3 in Vanzella et al. (2018). Direct detections of LyC emission at very high redshifts, where such detections would be most useful in constraining the nature of sources that drove reionization, will likely remain challenging even for the next generation of giant optical telescopes.

### 1.3 Sources of Lyman Continuum Flux and Likely Analogs

In the meantime, innumerable works have searched for evidence of LyC leakage from galaxies at  $z \sim 3$  and below, where the problem of IGM transmissivity at extreme UV wavelengths is less of an issue (e.g., Vanzella et al. 2010b, 2012b, 2016; Bergvall et al. 2013; Mostardi et al. 2015; Izotov et al. 2016b; Leitherer et al. 2016; Shapley et al. 2016; Bian et al. 2017; Naidu et al. 2017; Steidel et al. 2018; Fletcher et al. 2019; Rivera-Thorsen et al. 2019; Saha et al. 2020). However, this comes at the cost of pushing the redshifted LyC to near-UV bandpasses to which only a few instruments are sensitive (e.g., the now-decomissioned

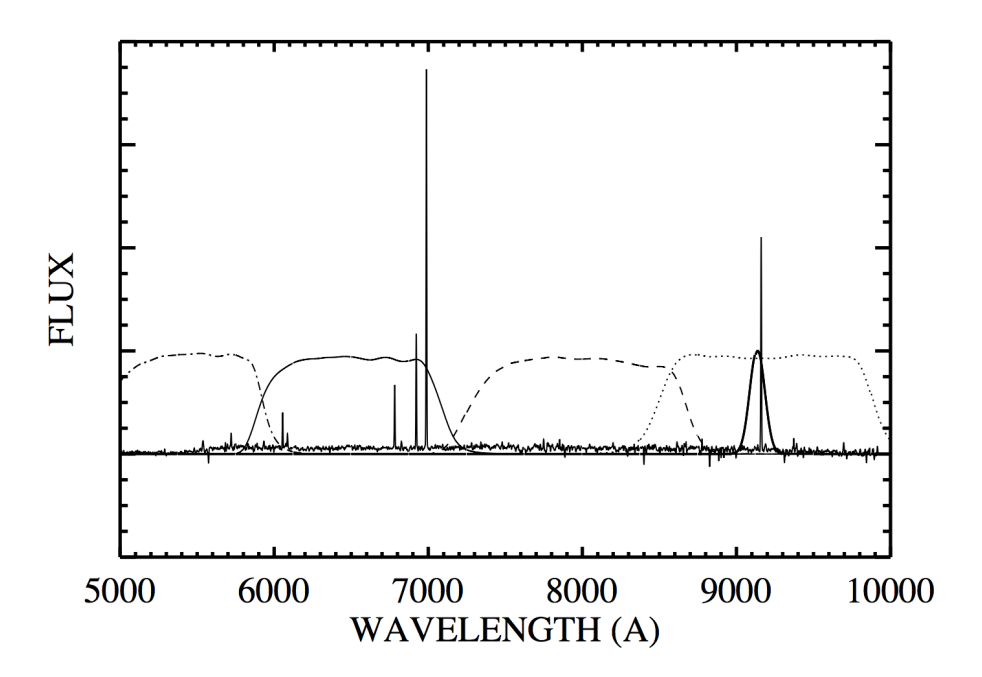


Figure 1.2: A Keck/DEIMOS spectrum of an ELG at z=0.398 in the COSMOS field, reproduced from Kakazu et al. (2007). The narrow solid curve shows the Subaru/SuprimeCam 9140 Å narrowband filter response, and the remaining curves show the relative response of the SuprimeCam V, R, I, and z' filters. Strong Balmer lines out to at least H $\delta$  and [OIII] lines at 4363, 4959, and 5007 Å are clearly visible in the R band. The flux density in the narrowband is dominated by H $\alpha$ , leading to an apparent excess relative to the much broader z' band. Also note that the lack of strong emission features in the I band will cause this galaxy to have unusual optical colors.

GALEX or the UV channel of HST's Wide Field Camera 3 (WFC3)). In Chapters 2 and 3 of this thesis, I will present the results of two searches for candidate sources of LyC emission at z = 2.5 - 3 (Jones et al. 2018, 2021a), which utilize public imaging from one of the deepest HST/WFC3 UV programs currently available (PI P. Oesch, Oesch et al. 2018b).

Another active topic of research is the testing and comparison of proposed *in*direct tracers of LyC emission. To date, some of the proposed tracers include high equivalent width Lyman- $\alpha$  emission (Micheva et al. 2017; Marchi et al. 2018; Steidel et al. 2018; Fletcher et al. 2019); moderate peak separation in multiply-peaked Lyman- $\alpha$  line profiles (Verhamme et al. 2017; Songaila et al. 2018; Vanzella et al. 2020); the flux ratio of the

strong [OIII] lines to the [OII] doublet (Nakajima & Ouchi 2014; Izotov et al. 2016a,b, 2018; Steidel et al. 2018; Fletcher et al. 2019; Tang et al. 2019); a deficiency in [SII] nebular emission (Wang et al. 2021); and flux ratios of lines in the Mg II doublet (Chisholm et al. 2020).

In effect, all of these diagnostics trace some combination of the stellar radiation field, neutral gas column density, and/or the presence of very low-metallicity gas. This is because galaxies in the EoR are expected to be low-mass, compact, highly star-forming, and chemically pristine, being too young to have substantially enriched their ISM. This, in turn, has motivated many searches for emission line galaxies (ELGs) at low, intermediate, and moderately high  $(z\sim3)$  redshifts, which appear to share these properties and thus may represent a population of close EoR analogs. One common method for selecting candidate ELGs is to search for galaxies with unusual broadband colors, with the assumption that the flux density in some filter has been boosted (relative to what would be measured in a line-free region of the spectrum) by a high equivalent-width emission line being redshifted into the bandpass (e.g., Cardamone et al. 2009; van der Wel et al. 2011; Colbert et al. 2013; Labbé et al. 2013; Pirzkal et al. 2013, 2018; Maseda et al. 2014, 2018; Amorín et al. 2015; Roberts-Borsani et al. 2016; Yang et al. 2017; Tang et al. 2021). Another requires that a galaxy shows an excess flux density in a narrowband filter relative to the nearest broadband (Gallego et al. 1995; Kakazu et al. 2007; Ly et al. 2007; Hu et al. 2009; Bayliss et al. 2011, 2012; Sobral et al. 2015; Coughlin et al. 2018; Hayashi et al. 2018; Khostovan et al. 2020).

The former technique is sensitive only to the most extreme line emitters (whose nebular emission must be strong enough to dominate the broadband flux), but can capture a wider swathe of redshift space than the narrowband method. Spectroscopic followup of ELG candidates is also frequently needed to identify exact redshifts and hence the line(s) which cause the observed color excess; see Figure 1.2 for an example spectrum of a narrowband-selected ELG at z=0.398, reproduced from Kakazu et al. (2007). However, the limited redshift coverage of the narrowband technique itself may be useful, as all galaxies of a certain type (e.g., the "H $\alpha$  emitter" or "[OIII] emitter" subsamples of Sobral et al. 2015) can be assumed to lie at virtually identical distances. This, in turn, greatly simplifies the calculation of line luminosity functions and the combined star formation rate of ELGs per comoving volume. I return to the subject of ELGs in Section 6, where I discuss the status of an additional project (not sufficiently complete to present as part of this thesis) that has yielded a large spectroscopic sample of narrowband-selected ELGs.

#### References

Amorín et al. 2015, A&A, 578, A105

Bayliss K. D., McMahon R. G., Venemans B. P., et al. 2012, MNRAS, 413, 2883

Bayliss K. D., McMahon R. G., Venemans B. P., et al. 2012, MNRAS, 426, 2178

Bergvall, N. et al. 2013, A&A, 554, A38

Bian, F., Fan, X., McGreer, I., Cai, Z., & Jiang, L. 2017, ApJ, 837, L12

Bouwens, R. J. et al. 2006, ApJ, 653, 53

Cardamone, C. et al. 2009, MNRAS, 399, 1191

Chisholm, J., Gazagnes, S., Schaerer, D., et al. 2018, A&A, 616, 30

Chisholm, J., Prochaska, J. X., Schaerer, D., et al. 2020, MNRAS, 498, 2554

Colbert J. W., Teplitz, H., Atek, H., et al., 2013, ApJ, 779, 34

Coughlin, A. et al. 2018, ApJ, 858, 96

Cowie, L. L., Barger, A. J., Bauer, F. E., & González-López, J. ApJ, 891, 69

Fan, X., Strauss, M. A., Becker, R. H., et al. 2006, AJ, 132, 117

Feng, Y., Di-Matteo, T., Croft, R. A., et al. 2016, MNRAS, 455, 2778

Finkelstein, S. L., D'Aloisio, A., Paardekooper, J.-P., et al. 2019, ApJ, 879, 36

Finlator, K., Özel, F., Davé, R., & Oppenheimer, B. D. 2009, MNRAS, 400, 1049

Fontanot, F., Cristiani, S., & Vanzella, E. 2012, MNRAS, 425, 1413

Fontanot, F. et al. 2014, MNRAS, 438, 2097

Fletcher, T. J. et al. 2019, ApJ, 878, 87

Gallego J., Zamorano J., Aragon-Salamanca A., & Rego M., 1995, ApJ, 455, 1

Giallongo, E., Grazian, A., Fiore, F. et al. 2019, ApJ, 884, 19

Grazian, A., Giallongo, E., Fiore, F., et al. 2020, ApJ, 897, 94

Grieg, B. & Mesinger, A. 2017, MNRAS, 465, 4838

Grimes, J. P., Heckman, T., Aloisi, A., et al. 2009, ApJS, 181, 272

Gunn, J. E. & Peterson, B. A. 1965, ApJ, 142, 1633

Hayashi, M., Tanaka, M., Shimakawa, R., et al. 2018, PASJ, 70, 17

Hu, E. M. et al. 2009, ApJ, 698, 2014

Inoue, A. K. et al. 2014, MNRAS, 442, 1805

Izotov, Y. I., Orlitová, I., Schaerer, D., et al. 2016, Nature, 529, 178

Izotov, Y. I., Schaerer, D., Thuan, T. X., et al. 2016, MNRAS, 461, 3683

Izotov, Y. I., Thuan, T. X., & Guseva, N. G. 2017, MNRAS, 471, 548

Izotov, Y. I., Worseck, G., Schaerer, D., et al. 2018, MNRAS, 478, 4851

Japelj, J. et al. 2017, MNRAS, 468, 389

Ji, Z. et al. 2020, ApJ, 888, 109

Jones, L. H., Barger, A. J., Cowie, L. L., et al. 2018, ApJ, 862, 142

Jones, L. H., Barger, A. J., & Cowie, L. L. 2021a, ApJ, 908, 222

Kakazu, Y. et al. 2007, ApJ, 668, 853

Kimm, T., Katz, H., Haehnelt, M. G., et al. 2017, MNRAS, 466, 4826

Khostovan, A. A., Malhotra, S., Rhoads, J. E., et al. 2020, MNRAS, 493, 3966

Kulkarni, G., Worseck, G., & Hennawi, J. F. 2019, MNRAS, 488, 1035

Labbé, I., Oesch, P. A., Bouwens, R. J., et al. 2013, ApJ, 777, L19

Laporte, N., Meyer, R. A., Ellis, R. S., et al. 2021, MNRAS, 505, 3336

Leitherer, C., Ferguson, H. C., Heckman, T. M., & Lowenthal, J. D. 1995, ApJ, 454, 19L

Leitherer, C. et al. 2016, ApJ, 823, L64

Ly, C., Malkan, M. A., Kashikawa, N., et al., 2007, ApJ, 657, 738

Ly, C., Lee, J. C., Dale, D. A., et al. 2011, ApJ, 726, 109

Madau, P. & Haardt, F. 2015, ApJ, 813, L8

Marchi, F., Pentericci, L., Guaita, L., et al. 2018, A&A, 614, A11

Maseda, M. V., van der Wel, A., Rix, H.-W., et al. 2014, ApJ, 791, 17

Maseda, M. V., van der Wel, A., Rix, H.-W., et al. 2018, ApJ, 854, 29

Micheva, G., Iwata, I., & Inoue, A. K. 2017, MNRAS, 465, 302

Mostardi, R. E., Shapley, A. E., et al. 2015, ApJ, 810, 107

Nakajima, K., & Ouchi, M. 2014, MNRAS, 442, 900

Naidu, R. P., Oesch, P. A., Reddy, N., et al. 2017, ApJ, 847, 12

Naidu, R. P., Tacchella, S., Mason, C. A., et al. 2020, ApJ, 892, 109

Oesch, P. A., Bouwens, R. J., Illingworth, G. D., et al. 2018, ApJ, 855, 1050

Oesch, P. A. et al. 2018, ApJS, 237, 12

Pirzkal N., Rothberg, B., Ly, C., et al., 2013, ApJ, 772, 48

Pirzkal N., Rothberg, B., Ryan, R. E., et al., 2018, ApJ, 868, 61

Price, L. C., Trac, H., & Cen, R. 2016, arXiv:1605.03970

Rivera-Thorsen, T. E., Dahle, H., Chisholm, J., et al. 2019, Science, 366, 738

Roberts-Borsani, G. W., Bouwens, R. J., Oesch, P. A., et al. 2016, ApJ, 823, 143

Robertson, B. E. et al. 2015, ApJ, 802, L19

Rutkowski, M. J., Scarlata, C., Henry, A., et al. 2017, ApJ, 841, 27

Saha, K., Tandon, S. N., Simmonds, C., et al. 2020, Nature Astronomy, 193

Shapley, A. E., Steidel, C. C., Strom, A. L., et al. 2016, ApJ, 826, L24

Shin, S., Im, M., Kim, Y., et al. 2020, ApJ, 893, 45

Sobral, D. et al. 2015, MNRAS, 451, 2303

Songaila, A., 2004, AJ, 127, 2598

Songaila, A., & Cowie, L. L. 2010, ApJ, 721, 1448

Songaila, A., Hu, E. M., Barger, A. J., et al. 2018, ApJ, 859, 91

Steidel, C. C. et al. 2018, ApJ, 869, 123

Tang, M., Stark, D. P., Chevallard, J., & Charlot, S. 2019, MNRAS, 489, 2572

Tang, M., Stark, D. P., Chevallard, J., et al. 2021, MNRAS, 501, 3238

Taylor, A. J., Barger, A. J., Cowie, L. L., et al. 2020, ApJ, 895, 132

Taylor, A. J., Cowie, L. L., Barger, A. J., et al. 2021, ApJ, 914, 79

van der Wel, A., Straughn, A. N., Rix, H.-W., et al. 2011, ApJ, 742, 111

Vanzella, E., Giavalisco, M., Inoue, A. K., et al. 2010, ApJ, 725, 1011

Vanzella, E., Guo, Y., Giavalisco, M., et al. 2012, ApJ, 751, 70

Vanzella, E. et al. 2016, ApJ, 825, 41

Vanzella, E., Nonino, M., Cupani, G., et al. 2018, MNRAS, 476, 15

Vanzella, E., Caminha, G. B., Calura, F., et al. 2020, MNRAS, 491, 1093

Verhamme, A., Orlitová, I., Schaerer, D., et al. 2017, A&A, 597, 13

Wang, B., Heckman, T. M., Amorín, R., et al. 2021, ApJ, 916, 3

Wise, J. C. 2019, Contemporary Physics, 40, 145

Huan Yang, H., Malhotra, S., Rhoads, J. E., & Wang, J. 2017, ApJ, 847, 38

## Chapter 2

## $z \sim 2.5 - 3$ Ionizers in the GOODS-N Field

A version of this chapter has previously appeared in the Astrophysical Journal Jones, L. H. et al. 2018, ApJ, 862, 142 and is cited as J18 throughout this dissertation.

### Abstract

We use deep F275W imaging from the Hubble Deep UV Legacy Survey (HDUV) and G280 grism spectroscopy from HST/WFC3, along with new and archival optical spectra from Keck/DEIMOS, to search for candidate ionizing sources in the GOODS-N field at  $z \sim 2.5$  – 3. Spectroscopic identification of our UV-selected sources are 99% complete to F275W = 25.5 in the region of the UV imaging, and we identify 6 potential ionizing galaxies or AGNs at  $z \sim 3$ . By far the brightest of these is a z = 2.583 AGN that totally dominates the ionizing flux in the region, with a specific ionizing volume emissivity at 912 Å of  $\epsilon_{912} = 8.3_{1.4}^{27} \times 10^{24}$  erg s<sup>-1</sup> Hz<sup>-1</sup> Mpc<sup>-3</sup>. Based on our spectroscopic data, we find four candidates are contaminated by foreground galaxies at  $z \sim 0.5$  – 0.7. At  $\epsilon_{912} = 2.2_{0.4}^{7.2} \times 10^{23}$  erg s<sup>-1</sup> Hz<sup>-1</sup> Mpc<sup>-3</sup>, the remaining candidate galaxy's contribution to the ionizing background lies well below the flux required to ionize the intergalactic medium at  $z \sim 2.5$  – 3, consistent with previous observations that show AGNs provide the bulk of the ionizing background at these redshifts.

#### 2.1 Introduction

One of the most pressing issues in modern observational cosmology is the identification of sources that contribute to the metagalactic ionizing background, particularly in the era of cosmic reionization — an important epoch in the history of the Universe that saw the formation of the first stars and galaxies at  $z \gtrsim 6$  (e.g., Bouwens et al. 2006, 2012, 2015; Ouchi et al. 2009; Robertson et al. 2015). Star-forming galaxies and active galactic nuclei (AGNs) both contribute to the production of ionizing photons, though their relative importance appears to evolve with cosmic time. Most evidence currently favors a scenario in which low-luminosity star-forming galaxies are the primary driver of hydrogen reionization (Riccoti & Shull 2000; Bouwens et al. 2006; Fontanot et al. 2007, 2014; Robertson et al. 2010, 2015; Japelj et al. 2017), while AGN contributions to the ionizing background are small until  $z \sim 2-3$  (Barger et al. 2003; Bolton et al. 2005; Cowie, Barger, & Trouille 2009; Cristiani et al. 2016; Smith et al. 2017; Puchwein et al. 2019). However, some authors have argued that quasars/AGNs could remain important at very high redshifts, producing a non-negligible or even dominant fraction of UV photons during the era of reionization (e.g., Fontanot et al. 2012; Giallongo et al. 2015, Madau & Haardt 2015).

One motivation for these latter studies is to relax constraints on the escape fraction,  $f_{esc}$ , needed to produce the observed ionizing background at high redshift; these constraints are imposed by a faint galaxy dominated reionization scenario. Indeed, determining a value for  $f_{esc}$ , which is the fraction of all Lyman continuum (LyC, rest frame  $\lambda < 912$  Å) photons that manage to escape their galaxy of origin to ionize the intergalactic medium (IGM), has been a major focal point of research on reionization. Most theoretical and semi-analytical models of reionization require an average  $f_{esc}$  of about 10% or greater for

star-forming galaxies (e.g., Bolton & Haehnelt 2007; Vanzella et al. 2012a; Feng et al. 2016; Price et al. 2016; Kimm et al. 2017; see, however, Faucher-Giguère et al. 2008 and Matthee et al. 2017), though at the highest redshifts  $f_{esc}$  remains largely unconstrained by observations. For sources at  $z \gtrsim 4$ , the low transmissivity of the IGM effectively prohibits direct measurements of  $f_{esc}$  (Madau 1995; Songaila 2004; Inoue et al. 2014). Thus, observations focused on analogous objects at slightly lower redshifts are used to constrain the ionization history of the Universe.

Previous individual detections or stacked data analyses suggest small values of  $f_{esc}$  in the local universe, at most  $\sim 1-3\%$  (e.g., Leitherer et al. 1995; Steidel et al. 2001; Grimes et al. 2009; Cowie et al. 2010; Leitet et al. 2013; Rutkowski et al. 2016), with some indications that the escape fraction increases with decreasing UV luminosity and/or increasing redshift (e.g., Mitra et al. 2013; Fontanot et al. 2014; Faisst 2016; Khaire et al. 2016; Japelj et al. 2017). Significant object-to-object variance and differences in the average  $f_{esc}$  between types of sources (i.e.,  $f_{esc} \gtrsim 0.5$  for AGNs versus a few percent for galaxies) further complicates the quest for a reliable measurement of the global ionizing escape fraction (Fernandez-Soto et al. 2003; Ma et al. 2015; Cristiani et al. 2016; Grazian et al. 2016; Guaita et al. 2016).

Much effort has thus been expended in building up a statistically significant population of LyC-emitting sources across a range of redshifts. A handful of strong LyC emitters have been detected in the local universe using data from the Sloan Digital Sky Survey (SDSS), the COS spectrograph on the *Hubble Space Telescope* (HST), and other facilities (e.g., Bergvall et al. 2013; Borthakur et al. 2014; Izotov et al. 2016a,b, 2018; Leitherer et al. 2016). Additional individual detections at redshifts  $\sim 2-3$  have been made, albeit with some contamination from foreground objects (e.g., Vanzella et al. 2010a,b, 2012b; Mostardi et al. 2015; Siana et al. 2015; Grazian et al. 2016; Shapley et al. 2016), while

stacking analyses tend to give a relatively weak average LyC signal at  $z \gtrsim 3$  (e.g., Marchi et al. 2017; Rutkowski et al. 2017; Naidu et al. 2018; Steidel et al. 2018).

The GOODS-North and South fields (Giavalisco et al. 2004) are particularly attractive targets for LyC-emitter searches due to the abundance of ancillary data, including thorough spectroscopic coverage. For example, Cowie, Barger, & Trouille (2009) (hereafter CBT09) used a sample of X-ray selected broad-line AGNs in the GOODS-N to estimate the contributions of AGNs and galaxies to the ionizing background over 0 < z < 5. They found a  $2\sigma$  upper limit of 0.008 for the escape fraction for galaxies at  $z \sim 1.15$  and, interestingly, that the AGN contribution at similar redshifts is dominated by a small number of far-UV (FUV)-bright quasars. Siana et al. (2010) used HST imaging of the GOODS fields to search for LyC emission at  $z \sim 1.3$  and constrain the relative escape fraction ( $f_{esc,rel}$ , the LyC flux relative to the UV continuum flux, typically at 1500 Å). They found a stacked upper limit of  $f_{esc,rel} < 0.02$  with no galaxies in their sample detected individually. More recently, Grazian et al. (2017) used U- and R-band imaging from the Large Binocular Telescope to constrain the escape of LyC photons at  $z \sim 3.3$  in several deep fields, including the GOODS-N field, and found  $f_{esc,rel}$  is at most 1.7% for their stacked image of 69 star-forming galaxies. Meanwhile, a particularly strong LyC candidate at  $z\sim3.2$  in the GOODS-S, known as Ion2, was discovered by Vanzella et al. (2015) and later confirmed by Vanzella et al. (2016) and de Barros et al. (2016), who found it to be a compact, low-metallicity source with an absolute escape fraction upwards of 50%.

Naidu et al. (2017) identified another six candidate LyC sources in the GOODS fields at  $z \sim 2$  (all with  $f_{esc} \gtrsim 13\%$ ) using HST/WFC3 imaging in the F275W and F336W bands from the Hubble Deep UV (HDUV) Legacy Survey (GO13872; Oesch et al. 2018). At the redshifts probed by Naidu et al. (2017), the Lyman break lies at  $\sim 2750$  Å, such that both ionizing and non-ionizing photons fall within the F275W window. To determine the true

contribution of LyC photons to the F275W flux then requires somewhat sophisticated and correspondingly uncertain modeling, along with Monte Carlo simulations of UV color and IGM attenuation. At redshifts greater than ~2.4, however, the F275W filter exclusively probes LyC photons, making the HDUV data a valuable asset for identifying ionizing sources at high redshifts.

In this paper, we combine new and preexisting optical spectroscopy on the GOODS-N field with the deep, high spatial resolution F275W data from the HDUV survey to obtain limits on the contributions of candidate LyC-emitting galaxies at  $z\sim3$ , where the HDUV filter set probes only the Lyman continuum, to the overall ionizing emissivity from star-forming galaxies and low-luminosity AGNs. We also present a new UV grism spectroscopic observation from HST/WFC3 of a  $z\sim2.6$  FUV-bright quasar.

In Section 2.2, we describe the data we used to select and characterize possible high-redshift LyC emitters, including UV and X-ray imaging, optical spectra from Keck/DEIMOS, and G280 grism spectroscopy. In Section 2.3, we describe our search for candidate LyC emitters and discuss the properties of the sources we found, along with potential sources of contamination by foreground galaxies. In Section 2.4, we estimate the associated contributions (or limits thereof) to the ionizing background at  $z \sim 3$  and compare to the flux required to maintain an ionized IGM at this redshift. In Section 2.5, we summarize our findings and discuss future prospects for the field.

We assume  $\Omega_M = 0.3$ ,  $\Omega_{\Lambda} = 0.7$ , and  $H_0 = 70 \text{ km s}^{-1} \text{ Mpc}^{-1}$  throughout this work. All magnitudes are given in the AB system, defined as  $m_{AB} = -2.5 \log f_{\nu} - 48.60$  for flux density,  $f_{\nu}$ , in units of erg s<sup>-1</sup> cm<sup>-2</sup> Hz<sup>-1</sup>.

### 2.2 Data

#### 2.2.1 **F275W** Imaging

The HDUV survey (GO13872; Oesch et al. 2018) is a 132-orbit WFC3 imaging program centered on the GOODS-North and South fields. Designed to capitalize on existing WFC3/UVIS imaging from the CANDELS (Grogin et al. 2011; Koekemoer et al. 2011) and UVUDF (Teplitz et al. 2013; Rafelski et al. 2015) surveys, the HDUV survey imaged both of these fields in the F275W and F336W filters around or within the existing CANDELS and UVUDF footprints. When combined with imaging from each of these surveys, the reduced HDUV images achieve depths of  $\approx 27.5$  and 27.9 mag in the F275W and F336W filters, respectively (5 $\sigma$  detection, 0.4 diameter aperture). Since the Lyman continuum is redshifted into the F275W bandpass at z > 2.4, the deep and relatively wide F275W coverage provided by the HDUV survey enables us to search for potential sources of ionizing radiation at high redshift.

### 2.2.2 Optical/NIR Spectroscopy

Secure spectroscopic redshifts are required for reliable identification of candidate LyC emitters within our F275W sample. The GOODS-N field is one of the most heavily-studied regions of the sky, with a wealth of existing spectroscopic data from DEIMOS on Keck I and LRIS and MOSFIRE on Keck II (e.g., Cohen et al. 2000; Cowie et al. 2004, 2016; Swinbank et al. 2004; Wirth et al. 2004, 2015; Chapman et al. 2005; Reddy et al. 2006; Barger et al. 2008; Trouille et al. 2008; Cooper et al. 2011; Kriek et al. 2015; U et al. 2015; Cowie et al. 2016). We crossmatched our sample (defined in Section 2.3.1) to existing Keck spectroscopic catalogs to determine redshifts, then used DEIMOS to target any F275W source in our sample without existing spectroscopic identifications, or to obtain additional spectra of

candidate LyC emitters to check for possible contamination by foreground galaxies (see Sections 2.3.3.1 - 2.3.3.6).

For our new DEIMOS observations, we used the 600 line mm<sup>-1</sup> grating, giving a  $d\lambda$  of 3.5 Å and a wavelength coverage of 5300 Å. We centered the spectra at an average wavelength of 7200 Å, but the exact wavelength range for each spectrum depends on the position of the slit in the mask. We broke each  $\sim 1$  hr exposure into three sub-exposures positioned at a central position and two offset positions stepped 1".5 in each direction along the slit. Our dithering procedure provides extremely high-precision sky subtraction. We reduced the spectra following the procedures described in Cowie et al. (1996).

#### 2.2.3 UV Grism Spectroscopy

The HST/WFC3 grism spectrum from program GO12479 (PI: Hu) was based on 5 dithered observations with the G280 grism. Each observation was 475 s, giving a total exposure time of 2375 s. We also obtained a 120 s imaging exposure with the F2000LP filter to set the zero point for computing the shape of the spectrum and the wavelength calibration. The G280 grism extends to a short wavelength of 1900 Å with a resolution of 70 at 3000 Å, giving coverage down to a rest wavelength of 530 Å. We measured the flux from the first order spectrum using the calibrations of the spatial distortion and wavelength relative to the zeroth order given in Kuntschner et al. (2009). We extracted the spectrum as a function of wavelength with a 6 pixel (0"24) boxcar centered on the central position of the spectrum. Finally, we flux calibrated the spectrum in units of microJansky, though the absolute calibration is not critical in the present analysis.

#### 2.2.4 X-ray Imaging

To identify probable AGNs in our F275W sample, we used X-ray data from the 2 Ms Chandra X-ray Observatory exposure of the Chandra Deep Field-North (Alexander et al. 2003; Xue et al. 2016). This image reaches a limiting flux of  $f_{0.5-2\text{keV}} \approx 1.5 \times 10^{-17} \text{ erg cm}^{-2} \text{ s}^{-1}$  near the central aim point. We used a 1".5 search radius to identify X-ray counterparts to sources in our F275W sample; 60 had X-ray counterparts. We computed the rest-frame 2 – 8 keV luminosities,  $L_X$ , of these counterparts from the 0.5 – 2 keV fluxes with an assumed  $\Gamma = 1.8$  and no absorption correction using

$$L_X = 4\pi d_L^2 f_{0.5-2\text{keV}} \left(\frac{1+z}{4}\right)^{\Gamma-2} \text{erg s}^{-1}.$$
 (2.1)

We classify any source with an X-ray luminosity  $L_X > 10^{44}$  erg s<sup>-1</sup> as a quasar (red squares enclosed by a purple open square in Figure 2.1).

### 2.3 Search for $z \sim 3$ Candidate LyC Emitters

#### 2.3.1 F275W Sample

We started with all  $z_{850} < 26$  galaxies from the 140 arcmin<sup>2</sup> GOODS-N observations of Giavalisco et al. (2004) obtained with HST's Advanced Camera for Surveys (ACS). At  $z \sim 3$ , the ACS F850LP filter probes the rest-frame FUV at  $\sim 2300$  Å, providing a good selection of likely star-forming galaxies at these redshifts. We then restricted to the 68 arcmin<sup>2</sup> area where there is F275W coverage with rms errors fainter than 27 mag. There are 5712 sources with  $z_{850} < 26$  in this area. In the left panel of Figure 2.1, we plot redshift versus F435W (B) magnitude for this area. The spectroscopic identifications are 98% complete to B = 24.5, 95% in B = 24 - 24.5, and 82% in B = 24.5 - 25.

We next measured the F275W magnitudes within 1" diameter apertures at the positions of each  $z_{850} < 26$  source using a customized IDL routine and subtracting the

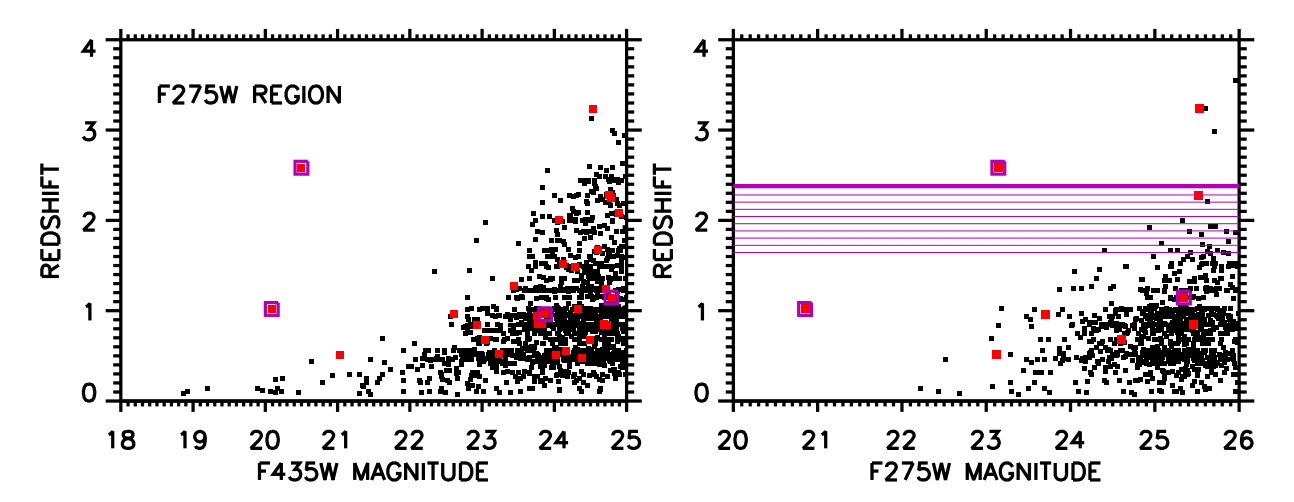


Figure 2.1 : Spectroscopic redshift vs. F435W (B) magnitude (left) and F275W magnitude (right) for the 68 arcmin² area covered by the HDUV GOODS-N F275W image. Sources with no X-ray counterpart are denoted by black squares, while sources with an X-ray detection are denoted by red squares, and those with quasar X-ray luminosities are enclosed in purple open squares. The spectroscopic identifications only start to become significantly incomplete (82% identified) at B magnitudes of 24.5-25. In the right panel, the thick purple line marks the redshift above which the F275W filter is sampling solely below the Lyman continuum break (z=2.36). The purple hatched region shows the redshift range where the break falls within the filter bandpass. The spectroscopic identifications only start to become significantly incomplete (68% identified) at F275W magnitudes of 25.5-26.

background using the median in a 3-6'' annulus. Magnitude errors were measured from the associated rms noise files. We hereafter consider the 1063 sources with F275W magnitudes brighter than 26 ( $4\sigma$ ) as our UV sample.

In the right panel of Figure 2.1, we show redshift versus F275W magnitude for this sample. Our spectroscopic identifications are 99% complete to F275W = 25.5, 98% in F275W = 25 - 25.5 (seven objects missing or unidentified), and 77% complete in F275W = 25.5 - 26.

Only five sources in the right panel of Figure 2.1 lie above the  $z \sim 2.4$  threshold (thick purple line) where the F275W flux consists solely of LyC photons (assuming no contamination from foreground sources). One of these sources is an X-ray AGN, and another is an X-ray quasar.

 $\mathrm{ID}^a$ R.A. Dec.  $z^b_{spec}$  $L_X$ F275W  $F435W_{AB}$  $F606W_{AB}$  $f_{ion}^d$  $z_{grism}^c$  $GN-UVC-1^{1,2}$ +62.257492 $2.583^{I}$  $3.44 \times 10^{44}$ 20.50 189.095581 2.597 23.14 20.49 0.087  $GN-UVC-2^1$  $5.66 \times 10^{42}$ 189.179535+62.185806 $3.236^{I}$ 3.299 25.5324.5423.40 $3.239^{I,II}$ GN-UVC-3<sup>1,2</sup> 189.275543+62.25046225.6025.2124.46 $2.984^{I,II}$  $GN-UVC-4^1$ +62.271030189.14875825.7125.0524.58 $GN-UVC-5^1$  $3.546^{I,III}$ 189.296936+62.27098925.96 25.77 25.44GN-UVC-6<sup>2</sup>  $2.439^{II}$ 189.201889 +62.26668226.53 24.93 24.740.193

Table 2.1: Summary of Six Candidate LyC Emitters

Note—  $^a$ Superscripts indicate if a candidate was selected by (1) its F275W magnitude, (2) its F275W-F435W color, or both.

<sup>b</sup>Spectroscopic redshifts from (I) this work; (II) Reddy et al. (2006); and (III) U et al. (2015).

<sup>c</sup>Determined from G280 grism data from *HST*/WFC3 (GO12479, PI: Hu) for GN-UVC-1, and from G141 grism data from the 3D-HST survey (Momcheva et al. 2016) for GN-UVC-2.

<sup>d</sup>Ratio of F275W flux to F606W flux (rest-frame  $\sim 675$  Å to 1500 Å; see Section 2.4).

#### 2.3.2 Color-Selected Sample

Alternatively, we can utilize a color selection to search for candidate ionizing sources. In order to have a substantially complete spectroscopic sample, we start with sources with B < 25 (see Figure 2.1). We then use  $V - z_{850} < 1$  to select galaxies with relatively flat UV continua (i.e., likely star-forming galaxies) at high redshifts. We plot F275W-F435W versus redshift in Figure 2.2 for the sources that meet these criteria. We indicate with purple hatching the redshift range where the F275W filter straddles the Lyman break. The typical color becomes noticeably redder around  $z \sim 2$  as the LyC break moves into this window, with most objects at  $z \gtrsim 2$  having so little F275W flux that we can measure only lower limits on the color. We find three z > 2.36 sources that have measured F275W-F435W colors at the  $> 2\sigma$  level. We show these with error bars and enclosed in green circles in Figure 2.2. Two of these color-selected sources also fall into our F275W-selected sample (see Section 2.3.1) and appear in Figure 2.1 (one is the X-ray quasar), while the third is detected at the  $2.9\sigma$  level in F275W.

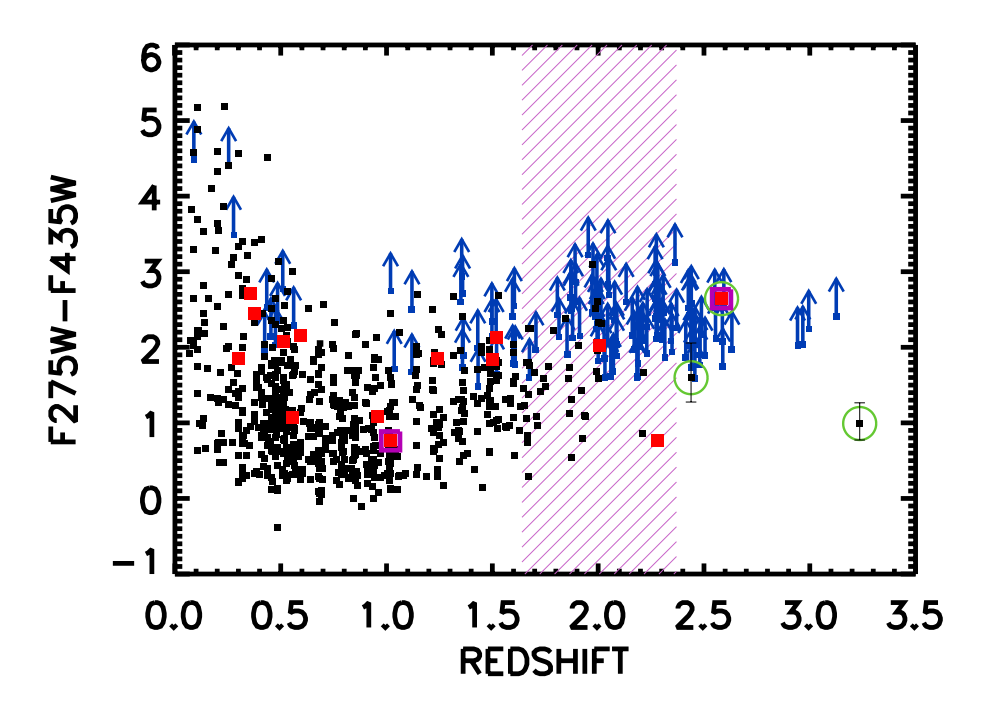


Figure 2.2 : Observed F275W-F435W vs. redshift for B < 25 galaxies with flat rest-frame UV continua (i.e., selected using  $V - z_{850} < 1$ ). Sources with no X-ray counterpart are denoted by black squares, while sources with an X-ray detection are denoted by red squares, and those with quasar X-ray luminosities are enclosed in purple open squares. Sources with lower limits on F275W-F435W are plotted at their  $2\sigma$  values with blue upward pointing arrows. The purple hatched region marks the redshift range where the F275W filter straddles the Lyman break. The three sources enclosed in green open circles have measured F275W-F435W colors at  $> 2\sigma$  significance and are shown with error bars that reflect the  $1\sigma$  uncertainties in the F275W magnitudes.

#### 2.3.3 Six Candidate LyC Emitters

In Table 2.1, we list the basic properties of our six candidate LyC emitters, including ID number, decimal coordinates, ground-based spectroscopic and (when available) HST grism redshifts, X-ray luminosities, F275W, B, and V magnitudes, and ionization fraction  $f_{ion}$  (see Section 2.4). We show in Figure 2.4 both the F275W thumbnail (left) and three-color thumbnail (right; red = F160W, green = F606W, blue = F435W) images of each source. In the following subsections, we briefly discuss for each of the six sources individually our efforts to try and confirm the LyC emission from the  $z \sim 3$  sources.

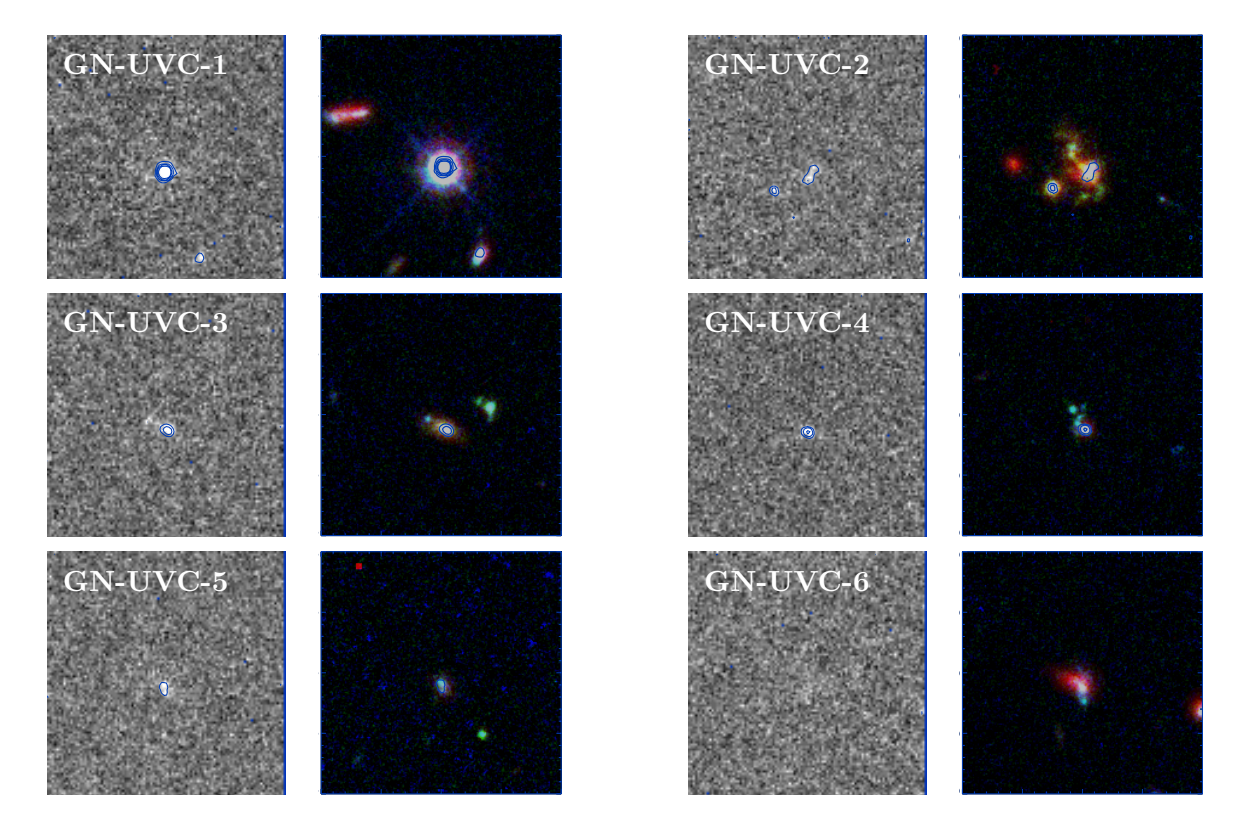
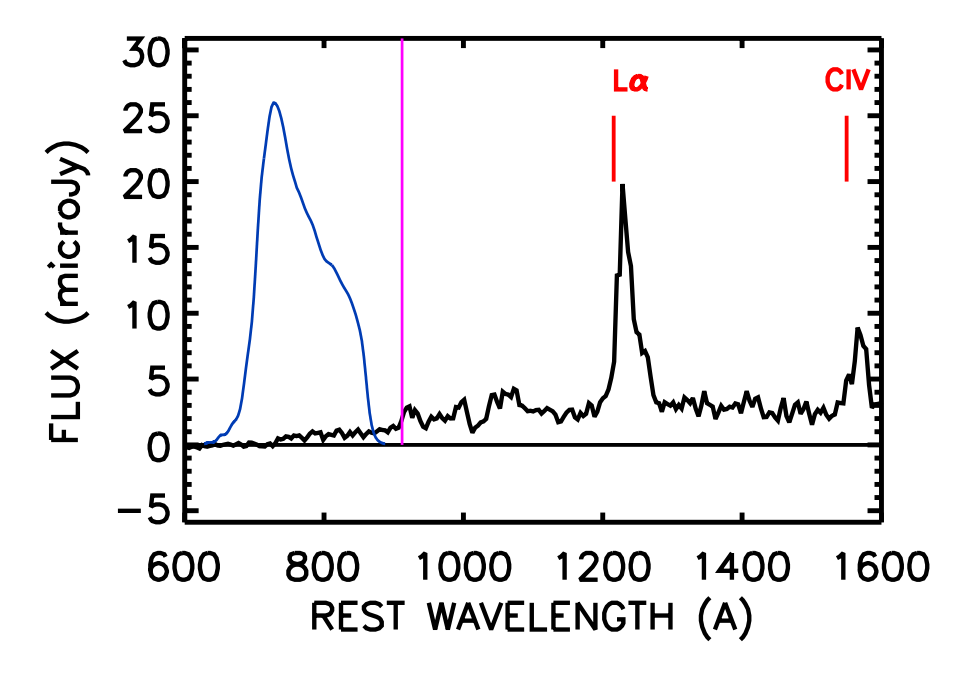


Figure 2.4: F275W thumbnails (left) and three-color images (red = F160W, green = F606W, and blue = F435W) of our six candidate LyC emitters. Blue contours show F275W emission for sources detected at or above the  $4\sigma$  level in the HDUV F275W imaging. (Note that GN-UVC-6 is detected at the 2.9 $\sigma$  level in F275W and was selected based on its relatively blue F275W-F435W color; see Section 2.3.) Images are 6" on a side. North is up and East is to the left. The sources appear slightly below center in y to allow for the labels at the top.

#### 2.3.3.1 GN-UVC-1

The broad-line quasar GN-UVC-1 at z=2.583 with an F275W magnitude of 23.14 is easily the brightest of our six candidate LyC emitters. The smaller F275W source to its lower right (see Figure 2.4) is likely a star-forming galaxy at low redshift. GN-UVC-1 is one of two objects in our candidate sample (the other being GN-UVC-3) that was selected both by its F275W flux alone and by its relatively blue F275W-F435W color ( $\approx 2.6$  mag). As shown in Figure 2.5, the HST/WFC3 G280 grism spectrum of GN-UVC-1 (GO12479, PI: Hu) directly confirms its identification as a high-redshift LyC emitter.



**Figure 2.5**: G280 grism spectrum from *HST*/WFC3 for GN-UVC-1. The blue curve shows the relative response of the F275W filter shifted into the rest frame of GN-UVC-1, and the pink vertical line marks the LyC edge.

#### 2.3.3.2 GN-UVC-2

GN-UVC-2 illustrates particularly well the difficulties of trying to confirm LyC emission from high-redshift galaxies. There are two positions in the F275W image (see Figure 2.4) that show significant UV flux: one coinciding with a somewhat extended star-forming galaxy/possible weak AGN ( $L_X \sim 6 \times 10^{42} \text{ erg s}^{-1}$ ) roughly at image center, and one coinciding with a neighboring source about 1" away. In Figure 2.6, we show our DEIMOS spectrum with a total exposure time of  $\sim$ 6 hours. In the individual exposures, we used a 1" wide slit and slit position angles ranging from 41° to 59°. We visually identify two redshift systems in the spectrum. Absorption features from the extended, central z=3.236 source (L $\alpha$ , CIV1550, and AlIII1670, marked in blue on the spectrum) are clearly present, but so are emission lines ([OII]3727, H $\beta$  and [OIII]4959,5007) from a z=0.512 foreground source (marked in red). We note that at the position angles of the individual spectra, the

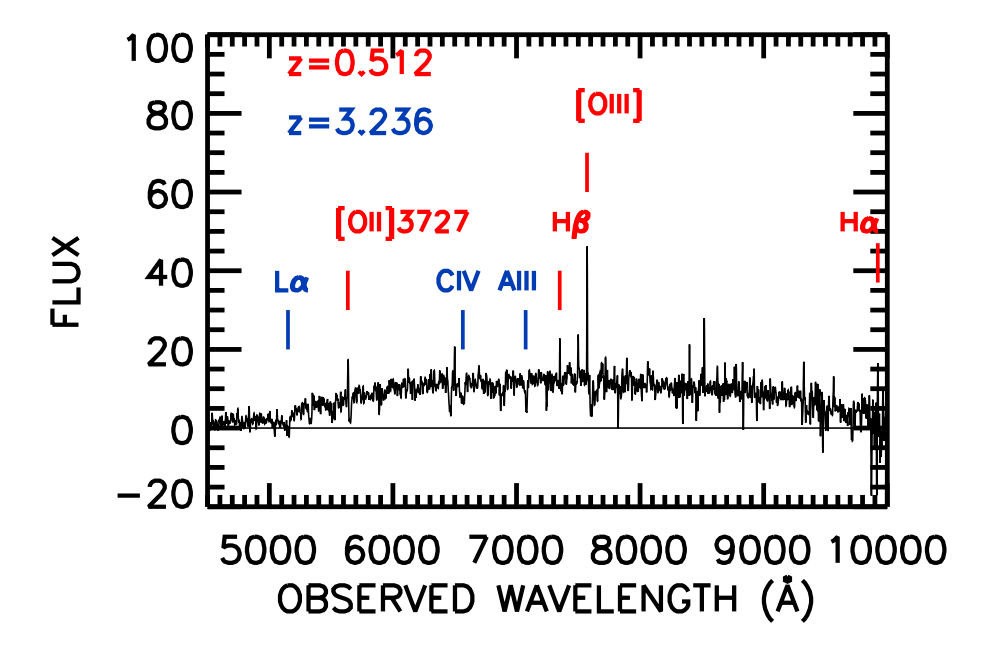


**Figure 2.6**: Our DEIMOS spectrum of GN-UVC-2. In addition to absorption features from a z = 3.236 galaxy (marked in blue), emission lines from a foreground galaxy at z = 0.512 (marked in red) are clearly present.

neighboring source is located just outside the slit. Thus, it is unlikely that it could be the source of the emission lines, since the lines would have to be extraordinarily strong to overflow into the slit at these position angles. Moreover, the emission lines seen in the individual spectra are invariant from exposure to exposure, despite changes in position angle. This suggests that the low-redshift emission lines come from a source superposed more or less directly on top of the z=3.236 galaxy, calling into question the origin of the measured F275W flux.

In Figure 2.7(a), we show the F275W (blue curve) and F160W (red curve) continuum light profiles as they would appear in a 1" wide slit at a position angle of 116° that covers both the central and neighboring sources (the relative normalization of the profiles is arbitrary). There is significant UV continuum flux at both positions.

We next obtained an additional 1 hour DEIMOS spectrum (1" wide slit and 0".6

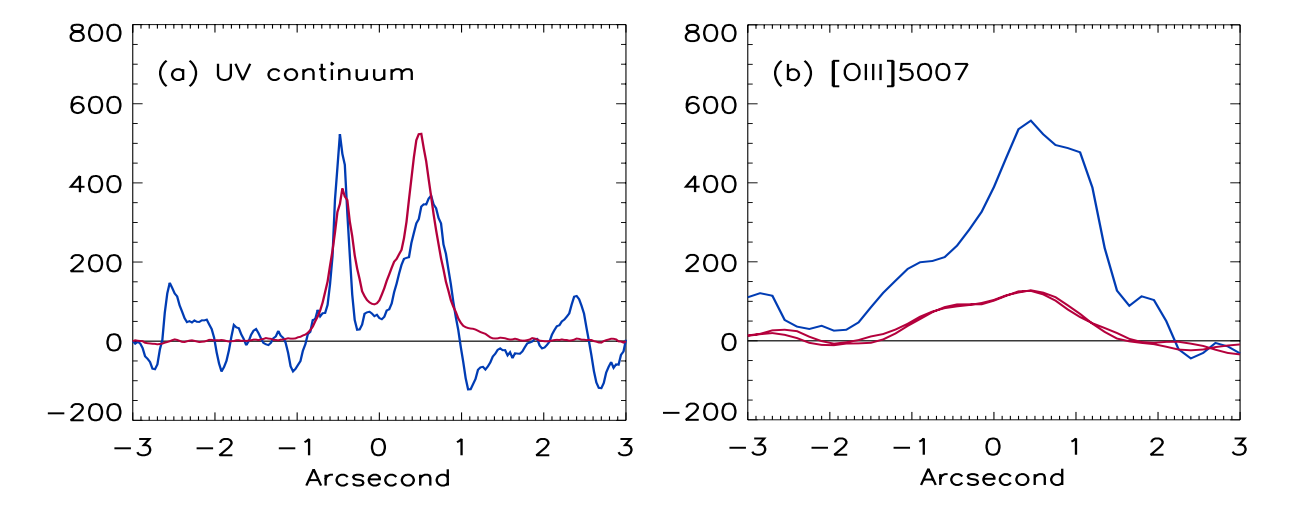
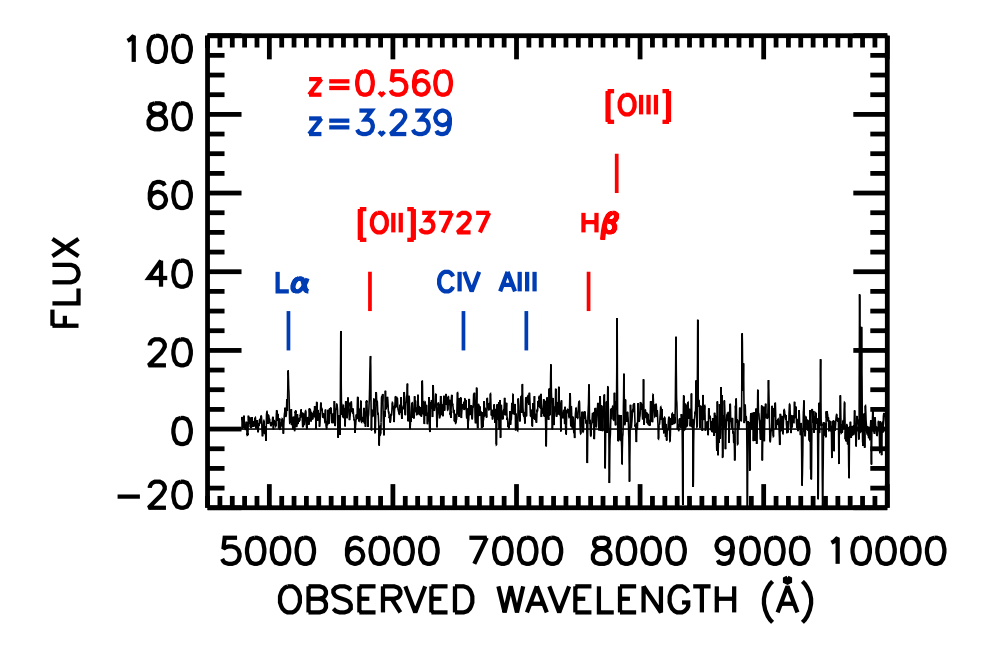


Figure 2.7: (a) The F275W (blue curve) and F160W (red curve) light profiles as they would appear in a 1" wide slit at a position angle of 116° that crosses both the LBG and the neighboring source in the GN-UVC-2 image (upper-right thumbnail in Figure 2.4). The relative normalization of the two profiles in this panel is arbitrary. (b) The light profile of the z = 0.512 [OIII]  $\lambda 5007$  Å line (blue curve) and the continuum measured both 300 Å redward and blueward of the line (red curves) as seen in a 1 hour Keck/DEIMOS spectrum taken at a position angle of 116°. The 0".6 seeing smooths the profile considerably relative to the HST continuum data, but the [OIII] profile lies above the continuum throughout the profile and is clearly present at the positions of both the LBG and the neighboring source.

seeing) at this position angle. If we examine the [OIII]  $\lambda 5007$  light profile from this new spectrum (Figure 2.7(b)), we see that there is [OIII] emission (blue curve) at both positions. The [OIII] profile is somewhat smoothed relative to the HST continuum data in Figure 2.7(a) due to the seeing. However, at the positions of both the central and neighboring sources, it is significantly brighter than the continuum measured both 300 Å redward and blueward of the line center (red curves). This confirms that the neighboring source is also at  $z \sim 0.5$ .

We consequently interpret the low-redshift emission lines as coming from a  $z \sim 0.5$  galaxy with two spatially separated star-forming components (i.e., similar to the chain galaxies of Cowie et al. (1995) and references therein), one of which lies directly along the line of sight to the high-redshift Lyman-break galaxy (LBG). Thus, the bulk of the



**Figure 2.8**: Our DEIMOS spectrum of GN-UVC-3, which shows features from sources at z = 3.239 (blue) and z = 0.56 (red).

measured F275W flux probably comes from the low-redshift galaxy, meaning GN-UVC-2 should not be used when constraining the ionizing background at  $z \sim 3$ . We exclude it from our analysis in Section 2.4.

#### 2.3.3.3 GN-UVC-3

We show in Figure 2.8 our DEIMOS spectrum of GN-UVC-3. As with GN-UVC-2, spectral features from a z=3.239 source (Ly $\alpha$  emission and CIV1550 absorption marked in blue) and from a foreground z=0.56 source ([OII]3727, H $\beta$ , and [OIII]4959,5007 emission marked in red) are visually identified. The high-redshift system was previously identified by Reddy et al. (2006). The low-redshift interloper is almost certainly the source of the F275W flux. Thus, we also exclude GN-UVC-3 from our analysis in Section 2.4.

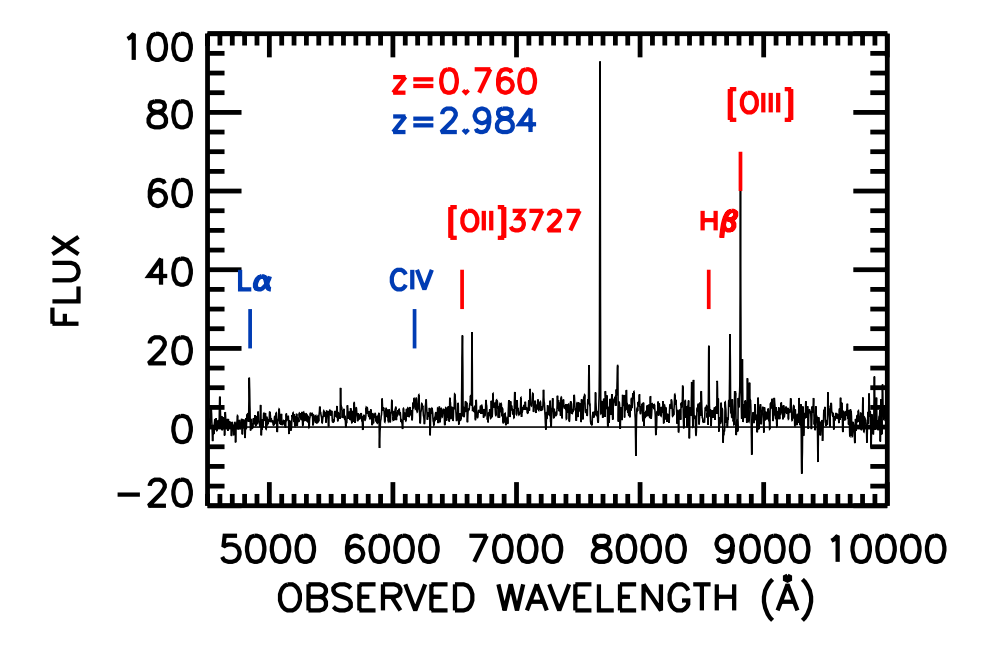


**Figure 2.9**: Our DEIMOS spectrum of GN-UVC-4, which shows features from sources at z = 2.984 (blue) and z = 0.76 (red).

#### 2.3.3.4 GN-UVC-4

GN-UVC-4 is peculiar, because its BVH thumbnail in Figure 2.4 shows at least two differently-colored components (a redder source at image center and an elongated, clumpy, blue source extending northward). However, the UV emission corresponds only to the central redder source. Our DEIMOS spectrum confirms the source as a projection of two emission line galaxies at very different redshifts (see Figure 2.9). The high-redshift identification at z = 2.984 is based on Ly $\alpha$  and CIV1550 emission and confirms the redshift obtained by Reddy et al. (2006). The low-redshift identification at z = 0.760 is based on [OII]3727, H $\beta$ , and [OIII]4959,5007 emission. We conclude that the UV emission probably comes from the low-redshift galaxy. Thus, we exclude GN-UVC-4 from our analysis in Section 2.4.

#### 2.3.3.5 GN-UVC-5

The F275W detection of GN-UVC-5 is quite surprising, because by z=3.546, the F275W bandpass probes rest-frame wavelengths well below the LyC break (at  $\sim$ 590 Å), where we expect virtually no transmission of ionizing radiation from the galaxy due to attenuation by the IGM (e.g., Inoue et al. 2014). U et al. (2015) label this object as having a very secure redshift identification (quality code 'A'), while photometric redshift estimates given in the 3D-HST catalog (Momcheva et al. 2016) put GN-UVC-5 (their GN-26359) at  $z_{phot}=0.74$ . These conflicting redshift estimates, together with the apparently singular nature in F275W of GN-UVC-5 (see Figure 2.4), suggest that this source may be yet another chance projection of two galaxies at vastly different redshifts. Indeed, our DEIMOS spectrum shows weak Ly $\alpha$  emission and CIV1550 in absorption (see Figure 2.10), confirming the redshift of U et al. (2015), while also showing [OII]3727, H $\beta$ , and [OIII]4959,5007 emission from a low-redshift galaxy at z=0.789. Since the UV emission probably comes from the low-redshift galaxy, we exclude GN-UVC-5 from our analysis in Section 2.4.

#### 2.3.3.6 GN-UVC-6

Of our six candidate LyC emitters, this is the sole object selected only based on its relatively blue F275W-F435W color ( $\approx 1.6$  mag, bluer even than the bright quasar GN-UVC-1), though we note that it is detected at the  $2.9\sigma$  level in F275W. We find a possible far-infrared counterpart to this source in the GOODS-Herschel catalog of Elbaz et al. (2011) (separation < 0.5''). This may indicate the presence of an AGN, though with only one detection from Herschel (in the PACS 160  $\mu$ m band) and negligible X-ray flux, this is somewhat tentative. The complicated morphology and multiple BVH colors seen in GN-UVC-6's three-color thumbnail (see Figure 2.4) suggests there may be superposed

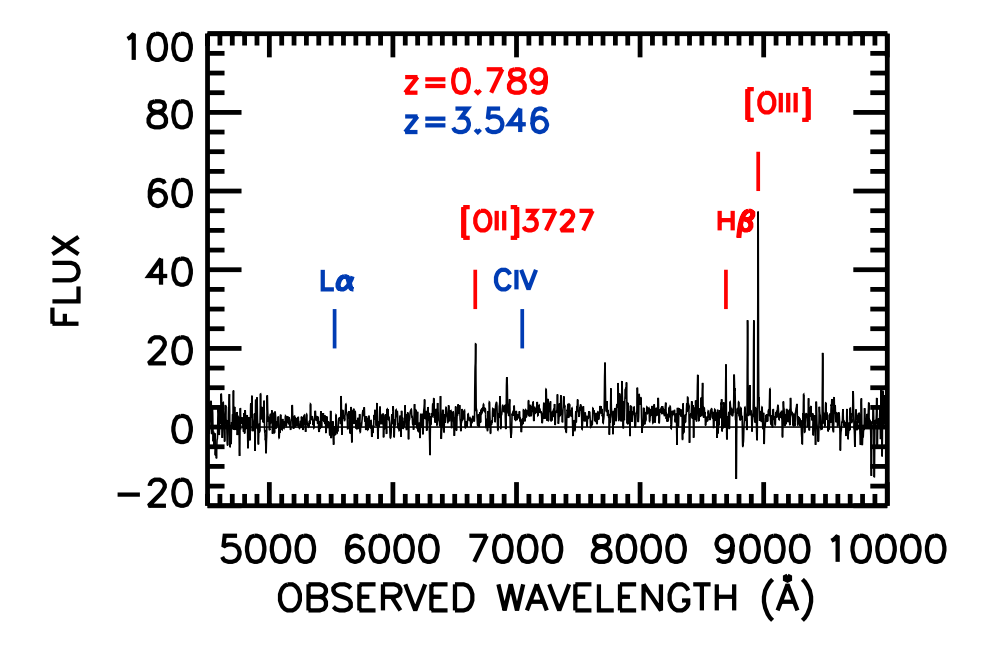


**Figure 2.10**: Our DEIMOS spectrum of GN-UVC-5, which shows features from sources at z = 3.546 (blue) and z = 0.789 (red).

sources that could lie at different redshifts. However, the photometric redshift of z=2.38 from Rafferty et al. (2011) is in good agreement with the spectroscopic redshift of z=2.439 from Reddy et al. (2006), which argues against contamination from foreground objects. We recently obtained a DEIMOS spectrum of this source and confirm that there are no features in the 4500-10,000 Å range that would indicate the presence of a superposed foreground object. We conclude that GN-UVC-6 remains a good candidate LyC emitter and can be used to obtain limits on the contribution of galaxies to the ionizing background at  $z\sim 3$ .

#### 2.4 Contributions to the Ionizing Flux

Determining the absolute escape fraction for each of our candidate LyC emitters is challenging, if not impossible, without knowledge of each source's intrinsic spectral energy distribution (SED) and degree of reddening. Instead, we compute the ionization fraction from  $f_{ion} = f_{LyC}/f_{1500}$ ; that is, the ratio of the flux at the rest-frame LyC wavelength

( $\sim$ 675 Å at z=3) to the flux at rest-frame 1500 Å, ignoring the small differential Kcorrection as a function of redshift. We use the F606W flux as a rough estimate of the
rest-frame 1500 Å flux, assuming a flat  $f_{\nu}$  SED. We note that this approximation is most
accurate for sources very near z=3. We give our measured ionization fractions in the last
column of Table 2.1 for the two sources that do not have clear spectroscopic evidence for
contamination by foreground galaxies.

#### 2.4.1 Quasar UV Emissivity

GN-UVC-1 is brighter than any other candidate in our sample by approximately two magnitudes. Since it is also the only quasar, we consider its contribution to the ionizing background separately from our other candidates. We measured its flux density at 912 Å directly from its UV grism spectrum after renormalizing the spectrum to match the total flux detected in the F275W imaging data. We then converted this to an ionizing volume emissivity,  $\epsilon_{912}$ , defined as the luminosity density per unit frequency divided by the comoving volume over the redshift range z=2.439-3.546 (the lowest and highest redshifts of our candidates). We hereafter quote measurements and uncertainties of  $\epsilon_{912}$  in units of  $10^{24}$  erg s<sup>-1</sup> Hz<sup>-1</sup> Mpc<sup>-3</sup>. For the single source in our "quasar sample", the Poisson noise dominates; from Gehrels (1986), the 68% confidence range for one object is 0.173 to 3.300. We find a quasar UV emissivity,  $\epsilon_{912,q}$ , of  $8.3_{1.4}^{27}$ .

#### 2.4.2 Non-quasar UV Emissivity

With four of five non-quasar candidates showing clear contamination from foreground objects, our "star-forming galaxy" sample considered here consists of GN-UVC-6 only. We estimated an ionizing emissivity  $\epsilon_{912,g}$  for this likely star-forming galaxy/possible low-luminosity AGN by assuming that GN-UVC-6's F275W flux is entirely at the filter's

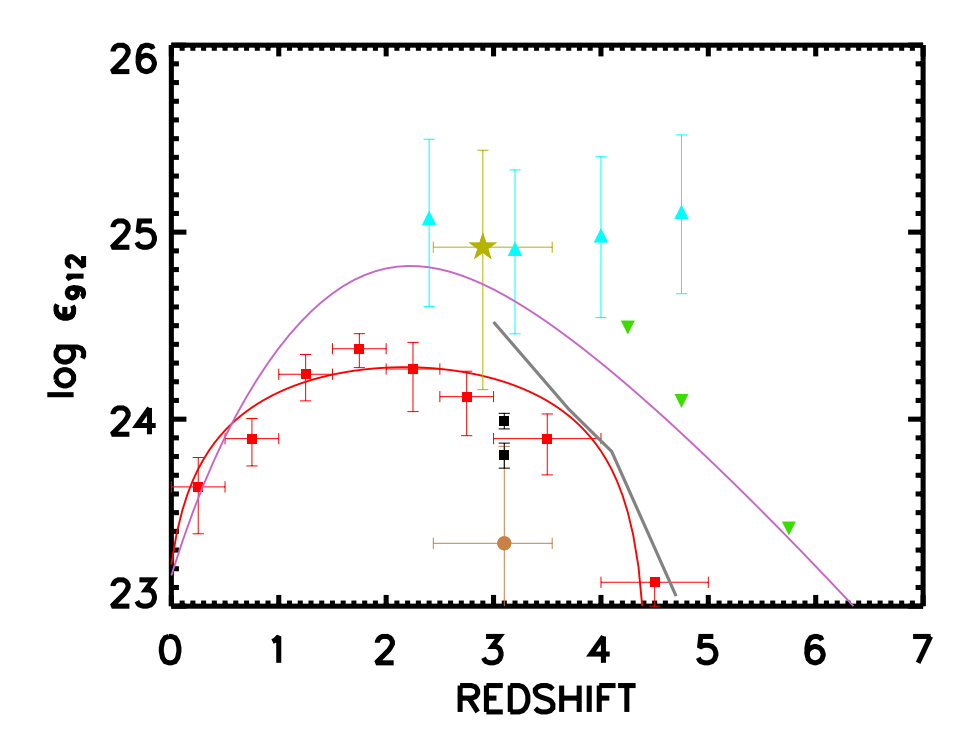


Figure 2.11: Ionizing volume emissivity at z=3 estimated from the quasar GN-UVC-1 (gold star) and compared to literature results for quasar/AGN contributions to the ionizing background at similar redshifts. Red, green, and black symbols show data from CBT09, Parsa et al. (2018), and Micheva et al. (2016), respectively, and the red, purple, and grey curves are from CBT09, Haardt & Madau (2012), and Meiksin (2005), respectively. The bronze circle shows the ionizing emissivity from star-forming galaxies and low-luminosity AGNs identified in this work (e.g., GN-UVC-6). Horizontal error bars on our data points reflect the range of redshifts in our candidate sample; the symbols have been splayed around the mean redshift of 3 for clarity. Cyan triangles show the observed ionizing emissivity from Becker & Bolton (2013).

effective wavelength of  $\sim 2704$  Å, or rest-frame  $\sim 786$  Å. To allow for a simpler and more direct comparison with literature results, which mostly consider the ionizing volume emissivity at or near the LyC edge, we scaled the measured flux density to that at 912 Å following the results of Lusso et al. (2015). They used a sample of 53 quasars at  $z \sim 2.4$  to construct a stacked UV spectrum between 600 and 2500 Å (rest frame), correcting for both intergalactic Lyman forest and Lyman continuum absorption, and found a  $\lambda < 912$  Å continuum slope of  $\alpha_{\nu} = -1.70$ . We used this power law slope to do our scaling.

We find that GN-UVC-6 contributes  $\epsilon_{912,g} = 0.22_{0.04}^{0.72}$  to the ionizing background at  $z \sim 3$ , where the total error is again dominated by the Poisson noise (in the 68% confidence range).

#### 2.4.3 Comparisons with the Literature

In Figure 2.11, we put our measurements in the context of other  $z \sim 3$  measurements from the literature. The level of ionizing volume emissivity that we estimated from our single quasar (gold star) is a factor  $\sim 38$  larger than our  $\epsilon_{912,g}$  (bronze circle). Though our small sample size makes quantitative comparisons difficult, our  $\epsilon_{912,g}$  is consistent, within the very large uncertainties, with the contribution measured by CBT09 from their much larger sample of broad-line AGNs (their Equation 1; red curve and points in Figure 2.11). It is also roughly consistent with quasar ionizing emissivity results from Meiksin (2005) (grey curve) and Haardt & Madau (2012) (purple curve).

Becker & Bolton (2013) used Ly $\alpha$  forest observations to infer the total ionizing background from 2 < z < 5. They obtained a nominal  $\epsilon_{912} = 8.15$  at z = 3.2, again a factor of  $\sim 38$  larger than our upper-limit estimate of  $\epsilon_{912,g}$  but consistent with our measured contribution from quasars. This suggests that quasars alone contribute virtually all of the metagalactic ionizing background at these redshifts. However, we caution that GN-UVC-1-like quasars are likely quite rare. The presence of such a LyC-luminous source in the relatively small comoving volume studied here is probably serendipitous, and a wider survey area (such as that used in CBT09) is needed to mitigate the effects of cosmic variance.

Meanwhile, for galaxies and/or low-luminosity AGNs like GN-UVC-6 to contribute significantly to the UV background, numerous fainter contributions would be required. We note, for example, that even with the high rate of contamination by foreground galaxies, the right panel of Figure 2.1 only starts to become significantly populated at  $z \gtrsim 2.4$  for

apparent magnitudes approaching our cutoff of F275W = 26.

We may also think about the limits of our sample selection in terms of the UV continuum absolute magnitudes  $M_{UV}$ , usually measured at 1500 or 1600 Å when deriving rest-frame UV luminosity functions (LFs) at various redshifts. Again using the observed F606W magnitudes of our candidate sources as an estimate of the rest-frame 1500 Å flux, we find that our  $z \sim 3$  candidate LyC emitters probe as faint as  $M_{UV} \approx -22.3$ . This is  $\sim 1.5$  magnitudes brighter than the characteristic luminosities of the  $z \sim 7$  rest-frame UV LFs derived in, e.g., Bouwens et al. (2015)  $(M_{1600}^* = -20.87)$  or Livermore et al. (2017)  $(M_{1500}^* = -20.80)$ . If our candidate LyC sources are taken to be analogs to the high-redshift galaxies that are responsible for reionization, these sources would thus still lie firmly on the bright end of the  $z \sim 7$  UV LF. Further, even though the very deep HST imaging used to construct these high-redshift UV LFs have detection limits as faint as  $M_{UV} \sim -14.5$ , even this is unable to detect the ultra-faint galaxies that appear to be required to complete hydrogen reionization by  $z \sim 6$  (e.g., Finkelstein et al. 2015; Livermore et al. 2017). A more accurate census of  $z \sim 3$  analogs to the very-high-redshift sources that drove reionization will require deeper F275W imaging and corresponding spectroscopic follow-up, though at such faint magnitudes, redshift identifications are quite difficult.

#### 2.5 Summary

We have presented a search for candidate LyC emitters at  $z \sim 3$  in the GOODS-North field using deep HST/WFC3 F275W imaging data and highly complete Keck/DEIMOS spectroscopic follow-up. We found five candidate ionizing sources brighter than F275W = 26, plus one additional source with blue F275W-F435W colors selected from a B < 25 sample with colors  $V - z_{850} < 1$ . One candidate (GN-UVC-1) is a  $z \sim 2.5$  quasar which, at F275W  $\sim 23.1$ , is exceptionally bright at rest-frame wavelengths blueward of the Lyman

limit. UV grism spectroscopy from HST/WFC3 confirms the presence of significant LyC flux. Four candidates each appear to be contaminated by a foreground  $z \sim 0.5-0.7$  galaxy based on deep optical spectroscopy.

The contribution of the quasar GN-UVC-1 to the ionizing background at  $z \sim 3$  totally dominates over the contributions from candidate LyC-emitting galaxies and faint AGNs (that is, GN-UVC-6, the sole non-quasar candidate source with no obvious contamination). Modulo potential currently-undetected contamination by lower redshift sources and the effects of cosmic variance, together they could account for the total ionizing background at  $z \sim 3$ . However, for galaxies and low-luminosity AGNs alone to account for all (or even a non-negligible portion of) the total ionizing background at  $z \sim 3$ , significant additional contributions from fainter sources would be needed. This will require deeper and wider area surveys to probe.

We gratefully acknowledge support from NASA grant NNX14AJ66G and NSF grant AST-1715145, the Trustees of the William F. Vilas Estate, and the University of Wisconsin-Madison Office of the Vice Chancellor for Research and Graduate Education with funding from the Wisconsin Alumni Research Foundation (A. J. B.). Support for program number GO-12479 was provided by NASA through a grant from the Space Telescope Science Institute, which is operated by the Association of Universities for Research in Astronomy, Inc., under NASA. Based in part on data obtained at the W. M. Keck Observatory, which is operated as a scientific partnership among the California Institute of Technology, the University of California, and NASA and was made possible by the generous financial support of the W. M. Keck Foundation. The authors wish to recognize and acknowledge the very significant cultural role and reverence that the summit of Mauna Kea has always had within the indigenous Hawaiian community. We are most fortunate to have the opportunity

to conduct observations from this mountain.

Facilities: DEIMOS (Keck II), Hubble

Software: astropy (Astropy Collaboration et al. 2018)

#### A Statement of Work

Here are briefly outlined the contributions of all listed authors for this publication, in order of their listing in the journal article.

- Logan H. Jones: Devised methodology for the photometry and sample selection; led analysis of optical spectra and of the contribution of HDUV sources to the LyC luminosity density at  $z \sim 3$ ; primary contributor to the writing of this manuscript.
- Amy J. Barger: Provided spectroscopic data for candidate LyC sources; suggested tests of the methodology; proofreading and revisions.
- Lennox L. Cowie: Provided spectroscopic data for candidate LyC sources; suggested tests of the methodology; proofreading and revisions.
- Pascal Oesch: Provided early access to the HDUV GOODS-North imaging data; proofreading and revisions.
- Esther M. Hu: Provided *HST* UV grism spectrum of GN-UVC-1; proofreading and revisions.
- Antoinette Songaila: Proofreading and revisions.
- Rohan P. Naidu: Provided checks on the candidate selection quality and final list of candidates; proofreading and suggested revisions.

#### References

Alexander, D. M., Bauer, F. E., Brandt, W. N., et al. 2003, AJ, 126, 539

Astropy Collaboration, Price-Whelan, A. M., Sipőcz, B. M., et al. 2018, AJ, 156, 123

Barger, A. J., Cowie, L. L., Capak, P., et al. 2003, ApJ, 584, L61

Barger, A. J., Cowie, L. L., & Wang, W.-H. 2008, ApJ, 689, 687

Becker, G. D. & Bolton, J. S., 2013, MNRAS, 436, 1023

Bergvall, N., Leitet, E., Zackrisson, E., & Marquart, T. 2013, A&A, 554, A38

Bolton, J. S., Haehnelt, M. G., Viel, M., & Springel, V. 2005, MNRAS, 357, 1178

Bolton, J. S. & Haehnelt, M. G. 2007, MNRAS, 382, 325

Bouwens, R. J., Illingworth, G. D., Blakeslee, J. P., & Franx, M. 2006, ApJ, 653, 53

Bouwens, R. J., Illingworth, G. D., Oesch, P. A., et al. 2012, ApJ, 752, L5

Bouwens, R. J., Illingworth, G. D., Oesch, P. A., et al. 2015, ApJ, 811, 140

Bouwens, R. J., Illingworth, G. D., Oesch, P. A., et al. 2015, ApJ, 803, 34

Borthakur, S., Heckman, T. M., Leitherer, C., & Overzier, R. A. 2014, Science, 346, 216

Chapman, S. C., Blain, A. W., Smail, I., & Ivison, R. J. 2005, ApJ, 622, 772

Cohen, J. G., Hogg, D. W., Blandford, R., et al. 2000, ApJ, 538, 29

Cooper, M. C., Aird, J. A., Coil, A. L., et al. 2011, ApJS, 193, 14

Cowie, L. L., Barger, A. J., Hu, E. M., Capak, P., & Songaila, A. 2004b, AJ, 127, 3137

Cowie, L. L., Barger, A. J., & Trouille, L. 2009, ApJ, 692, 1476

Cowie, L. L., Barger, A J., & Hu, E. M. 2010, ApJ, 711, 928

Cowie, L. L., Barger, A J., & Songaila, A. 2016, ApJ, 817, 57

Cowie, L. L. Hu, E. M., & Songaila, A. 1995, AJ, 110, 1576

Cowie, L. L., Songaila, A., Hu, E. M., & Cohen, J. G. 1996, AJ, 112, 839

Cristiani, S., Serrano, L. M., Fontanot, F., Vanzella, E., & Monaco, P. 2016, MNRAS, 462
2478

de Barros, S., Vanzella, E., Amorín, R., et al. 2016, A&A, 585, 51

Elbaz, D., Dickinson, M., Hwang, H. S., et al. 2011, A&A, 533, 119

Faisst, A. L. 2016, ApJ, 829, 99

Faucher-Giguère, C.-A., Lidz, A., Hernquist, L., & Zaldarriaga, M. 2008, ApJ, 688, 85

Feng, Y., Di-Matteo, T., Croft, R. A., et al. 2016, MNRAS, 455, 2778

Fernandez-Soto, A., Lanzetta, K. M., & Chen, H.-W. 2003, MNRAS, 342, 1215

Finkelstein, S. L., Papovich, C., Ryan, R. E., et al. 2015, ApJ, 758, 93

Fontanot, F., Cristiani, S., Monaco, P., et al. 2007, A&A, 461, 39

Fontanot, F., Cristiani, S., & Vanzella, E. 2012, MNRAS, 425, 1413

Fontanot, F., Cristiani, S., Pfrommer, C., Cupani, G., & Vanzella, E. 2014, MNRAS, 438, 2097

Gehrels, N. 1986, ApJ, 303, 336

Giallongo, E., Grazian, A., Fiore, F. et al. 2015, A&A, 578, A83

Giavalisco, M., Ferguson, H. C., Koekemoer, A. M., et al. 2004, ApJ, 600, L93

Grazian, A., Giallongo, E., Gerbasi, R., et al. 2016, A&A, 585, A48

Grazian, A., Giallongo, E., Paris, D., et al. 2017, A&A, 602, A18

Grogin, N. A., Kocevski, D. D., Faber, S. M., et al. 2011, ApJS, 197, 35

Guaita, L., Pentericci, L., Grazian, A., et al. 2016, A&A, 587, A133

Grimes, J. P., Heckman, T., Aloisi, A., et al. 2009, ApJS, 181, 272

Haardt, F. & Madau, P. 2012, ApJ, 746, 125

Inoue, A. K., Shimizu, I., Iwata, I., & Tanaka, M. 2014, MNRAS, 442, 1805

Izotov, Y. I., Orlitová, I., Schaerer, D., et al. 2016, Nature, 529, 178

Izotov, Y. I., Schaerer, D., Thuan, T. X., et al. 2016, MNRAS, 461, 3683

Izotov, Y. I., Worseck, G., Schaerer, D., et al. 2018, MNRAS, 478, 4851

Japelj, J., Vanzella, E., Fontanot, et al. 2017, MNRAS, 468, 389

Khaire, V., Srianand, R., et al. 2016, MNRAS, 457, 4051

Kimm, T., Katz, H., Haehnelt, M. G., et al. 2017, MNRAS, 466, 4826

Koekemoer, A. M., Faber, S. M., Ferguson, H. C., et al. 2011, ApJS, 197, 36

Kriek, M., Shapley, A. E., Reddy, N. A., et al. 2015, ApJS, 218, 15

Kuntschner, H., Bushouse, H., Kummel, M, & Walsh, J. R. 2009, ST-ECF Instrument Science Report WFC3 2009-01

Leitet, E., Bergvall, N., Hayes, M., et al. 2013, A&A, 553, A106

Leitherer, C., Ferguson, H. C., Heckman, T. M., & Lowenthal, J. D. 1995, ApJ, 454, 19L

Leitherer, C., Hernandez, S., Lee, J. C., & Oey, M. S. 2016, ApJ, 823, 64L

Livermore, R. C., Finkelstein, S. L., & Lotz, J. M. 2017, ApJ, 835, 113

Lusso, E., Worseck, G., Hennawi, J. F., et al. 2015, MNRAS, 449, 4204

Ma, X., Kasen, D., Hopkins, P. F., et al. 2015, MNRAS, 453, 960

Madau, P. 1995, ApJ, 441, 18

Madau, P. & Haardt, F. 2015, ApJ, 813, L8

Marchi, F., Pentericci, L., Guaita, L., et al. 2018, A&A, 614, A11

Matthee, J., Sobral, D., Best, P., et al. 2017, MNRAS, 465, 3637

Meiksin, A. 2005, MNRAS, 356, 596

Micheva, G., Iwata, I., & Inoue, A. K. 2016, MNRAS, 465, 302

Mitra, S., Ferrara, A., & Choudhury, T. R. 2013, MNRAS, 428, L1

Momcheva, I. G., Brammer, G. B., van Dokkum, P. G., et al. 2016, ApJS, 225, 27

Mostardi, R. E., Shapley, A. E., et al. 2015, ApJ, 810, 107

Naidu, R. P., Oesch, P. A., Reddy, N., et al. 2017, ApJ, 847, 12

Naidu, R. P., Forrest, B., Oesch, P. A., et al. 2018, MNRAS, 478, 791

Oesch, P. A., Montes, M., Reddy, N., et al. 2018, ApJS, 237, 12

Ouchi, M., Mobasher, B., Shimasaku, K., et al. 2009, ApJ, 706, 1136

Parsa, S., Dunlop, J. S., & McLure, R. J. 2018, MNRAS, 474, 2904

Price, L. C., Trac, H., & Cen, R. 2016, arXiv:1605.03970

Puchwein, E., Haardt, F., Haehnelt, M. G., & Madau, P. 2019, MNRAS, 485, 47

Rafelski, M., Teplitz, H. I., Gardner, J. P., et al. 2015, AJ, 150, 31

Rafferty, D. A., Brandt, W. N., Alexander, D. M., et al. 2011, ApJ, 742, 3

Reddy, N. A., Steidel, C. C., Erb, D. K., Shapley, A. E., & Pettini, M. 2006, ApJ, 653, 1004

Riccoti, M., & Shull, J. M. 2000, ApJ, 542, 548

Robertson, B. E., Ellis, R. S., Dunlop, J. S., McLure, R. J., & Stark, D. P. 2010, Nature, 468, 49

Robertson, B. E., Ellis, R. S., Furlanetto, S. R., & Dunlop, J. S. 2015, ApJ, 802, L19

Rutkowski, M. J., Scarlata, C., Haardt, F., et al. 2016, ApJ, 819, 81

Rutkowski, M. J., Scarlata, C., Henry, A., et al. 2017, ApJ, 841, 27

Shapley, A. E., Steidel, C. C., Strom, A. L., et al. 2016, ApJ, 826, L24

Siana, B., Teplitz, H. I., Ferguson, H. C., et al. 2010, ApJ, 723, 241

Siana, B., Shapley, A. E., Kulas, K. R., et al. 2015, ApJ, 804, 17

Smith, B. M., Windhorst, R. A., Jansen, R. A., et al. 2017, arXiv:1602.01555v2

Songaila, A., 2004, AJ, 127, 2598

Steidel., C. C., Pettini, M., & Adelberger, K. L. 2001, ApJ, 546, 665

Steidel, C. C., Bogosavlevic, M., Shapley, A. E., et al. 2018, ApJ, 869, 123

Swinbank, A. M., Smail, I., Chapman, S. C., et al. 2004, ApJ, 617, 64

Teplitz, H. I., Rafelski, M., Kurczynski, P., et al. 2013, AJ, 146, 159

Trouille, L., Barger, A. J., Cowie, L. L., Yang, Y., & Mushotzky, R. F. 2008, ApJ, 179, 1

U, V., Hemmati, S., Darvish, B., et al. 2015, ApJ, 815, 57

Vanzella, E., Siana, B., Cristiani, S., & Nonino, M. 2010, MNRAS, 404, 1672

Vanzella, E., Giavalisco, M., Inoue, A. K., et al. 2010, ApJ, 725, 1011

Vanzella, E., Nonino, M., Cristiani, S., et al. 2012, MNRAS, 424, 54

Vanzella, E., Guo, Y., Giavalisco, M., et al. 2012, ApJ, 751, 70

Vanzella, E., de Barros, S., Castellano, M., et al. 2015, A&A 576, A116

Vanzella, E., de Barros, S., Vasei, K., et al. 2015, ApJ, 825, 41

Wirth, G. D., Willmer, C. N. A., Amico, P., et al. 2004, AJ, 127, 3121

Wirth, G. D., Trump, J. R., Barro, G., et al. 2015, AJ, 150, 153

Wold, I. G. B., Barger, A. J., & Cowie, L. L. 2014, ApJ, 783, 119

Xue, Y. Q., Luo, B., Brandt, W. N., et al. 2016, ApJS, 224, 15

### Chapter 3

# Candidate $z \sim 2.5$ Lyman Continuum Sources in the GOODS Fields

A version of this chapter has previously appeared in the Astrophysical Journal Jones, L. H. et al. 2021, ApJ, 908, 222 and is cited as J21a throughout this dissertation.

#### Abstract

We use the wealth of deep archival optical spectroscopy on the GOODS-South field from Keck, the VLT, and other facilities to select candidate high-redshift Lyman continuum (LyC) leakers in the Hubble Deep UV Legacy Survey (HDUV) dataset. We select sources at 2.35 < z < 3.05, where the HST/WFC3 F275W filter probes only the redshifted LyC. We find five moderately F275W-bright sources (four detected at  $\gtrsim 3\sigma$  significance) in this redshift range. However, two of these show evidence in their optical spectra for contamination by foreground galaxies along the line-of-sight. We then perform an F275W error-weighted sum of the fluxes of all 129 galaxies at 2.35 < z < 3.05 in both the GOODS-N and GOODS-S HDUV areas to estimate the total ionizing flux. The result is dominated by just five candidate F275W-bright LyC sources. Lastly, we examine the contributions to the metagalactic ionizing background, finding that, at the sensitivity of the HDUV F275W data and allowing for the effects of LyC transmission in the intergalactic medium (IGM), star-forming galaxies can match the UV flux required to maintain an ionized IGM at  $z \sim 2.5$ .

#### 3.1 Introduction

For the past few decades, one of the most active areas of research in observational astronomy has been the identification of sources that contribute to the metagalactic ionizing This has been particularly important for building a cohesive picture of background. reionization — an important epoch in the history of the Universe in which the first galaxies formed and the bulk of hydrogen in the intergalactic medium (IGM) transitioned from neutral to ionized (e.g., Bouwens et al. 2006, 2012, 2015; Ouchi et al. 2009; Robertson et al. 2015). Massive stars and quasars/active galactic nuclei (AGN) both produce ionizing photons, though their relative importance to the global ionizing background appears to evolve over time. Most evidence currently favors a scenario in which dwarf star-forming galaxies (SFGs) are the primary driver of hydrogen reionization (Riccoti & Shull 2000; Bouwens et al. 2006; Fontanot et al. 2007, 2014; Robertson et al. 2010, 2015; Japelj et al. 2017), while AGN contributions to the ionizing background are small until  $z\sim 2$  – 3 (Barger et al. 2003; Bolton et al. 2005; Cowie, Barger, & Trouille 2009; Cristiani et al. 2016; Smith et al. 2020). However, because these scenarios typically rely on an extrapolation of observed galaxy counts to faint absolute magnitudes unobtainable even in the deepest HSTimaging, some authors have argued that quasars/AGN could produce a non-negligible or even dominant fraction of UV photons during the era of reionization (e.g., Fontanot et al. 2012; Madau & Haardt 2015). Of course, arguments for or against this alternate scenario depend critically on the assumed number density of AGN at high redshift, which is still a subject of significant debate (see, e.g., Giallongo et al. 2019; Cowie et al. 2020; Grazian et al. 2020; and Shin et al. 2020 for some recent analyses).

Another major uncertainty in determining the relative importance of SFGs and AGN

to reionization is constraining the escape fraction  $f_{esc}$ , defined as the fraction of all Lyman continuum (LyC, rest frame  $\lambda < 912$  Å) photons that manage to escape their galaxy of origin to interact with the IGM. Most theoretical and semi-analytical models of reionization require an average  $f_{esc}$  for SFGs of about 10% or greater, if SFGs are to be the primary driver of reionization (e.g., Bolton & Haehnelt 2007; Vanzella et al. 2012a; Feng et al. 2016; Price et al. 2016; Kimm et al. 2017; see, however, Faucher-Giguère et al. 2008 and Matthee et al. 2017), though at the highest redshifts,  $f_{esc}$  remains largely unconstrained by observations. For sources at  $z \gtrsim 4$ , the rising density of intervening neutral hydrogen absorption systems leads to much lower transmissivity of the IGM to LyC photons (Madau 1995; Songaila 2004; Inoue et al. 2014). This effectively prohibits direct detections of LyC emission (and hence estimates of  $f_{esc}$ ) along most sightlines at redshifts where such measurements are most needed, though some exceptions have been reported in recent years (e.g., the z = 4 source Ion3 in Vanzella et al. 2018 and the z = 3.8 source Ion1 in Ji et al. 2020). Thus, observations focused on analogous objects at slightly lower redshifts are often used to constrain the ionization history of the Universe.

Literature reports of individual or stacked LyC detections suggest that most galaxies have small values of  $f_{esc}$ , at most  $\sim 1-3\%$  (e.g., Leitherer et al. 1995; Steidel et al. 2001; Grimes et al. 2009; Cowie et al. 2010; Leitet et al. 2013; Rutkowski et al. 2016), and that the typical escape fraction increases with redshift (e.g., Mitra et al. 2013; Fontanot et al. 2014; Faisst 2016; Khaire et al. 2016; Japelj et al. 2017). The latter observation is based on a growing number of LyC detections at  $z \sim 2-3$  (e.g., Vanzella et al. 2010b, 2012b, 2018; Mostardi et al. 2015; Grazian et al. 2016; Shapley et al. 2016; Jones et al. 2018; Steidel et al. 2018; Fletcher et al. 2019; Rivera-Thorsen et al. 2019; Saha et al. 2020), though it is now well known that direct LyC searches can be affected by contamination from foreground galaxies (e.g., the projections from Vanzella et al. 2010a or the reexamination of sources

first reported in Shapley et al. 2006 by Siana et al. 2015). Stacking analyses also tend to give a relatively weak average LyC signal at these redshifts (e.g., Siana et al. 2010; Grazian et al. 2017; Rutkowski et al. 2017; Marchi et al. 2018; Naidu et al. 2018; Fletcher et al. 2019; see, however, Steidel et al. 2018).

However, some studies have suggested that particular subgroups of galaxies are more likely to have significant LyC escape. For example, moderately large Ly $\alpha$  equivalent width in emission (e.g., Micheva et al. 2017; Marchi et al. 2018; Steidel et al. 2018; Fletcher et al. 2019) or multiply-peaked Ly $\alpha$  line profiles (Verhamme et al. 2017; Vanzella et al. 2020) appear to be signposts of nonzero  $f_{esc}$ ; see, however, the confirmed LyC leaker Ion1, which shows Ly $\alpha$  in absorption only (Ji et al. 2020). A high flux ratio of [OIII] $\lambda\lambda$ 4959, 5007 to [OII] $\lambda\lambda$ 3727, 3729 (O32) has also recently been proposed as an optical marker of LyC escape (e.g., Nakajima & Ouchi 2014; Izotov et al. 2016a,b, 2018; Steidel et al. 2018; Fletcher et al. 2019; Tang et al. 2019). However, this connection remains tenuous, with several studies reporting that large O32 by itself is insufficient to guarantee significant LyC escape (e.g., Reddy et al. 2016b; Izotov et al. 2017; Rutkowski et al. 2017; Naidu et al. 2018; Barrow et al. 2020).

Legacy fields like the GOODS-North and South (Giavalisco et al. 2004) tend to be especially attractive targets for LyC leaker searches, due to the abundance of deep multiwavelength imaging and thorough spectroscopic coverage. In particular, the advent of the Hubble Deep UV (HDUV) Legacy Survey (Oesch et al. 2018) has now made it possible to perform direct photometric searches for LyC leakers at high redshift. Using the HDUV's deep HST/WFC3 imaging in the F275W and F336W bands, Naidu et al. (2017) identified six candidate LyC sources in the GOODS fields at  $z \sim 2$ , all with  $f_{esc} \gtrsim 13\%$ . However, at the redshifts probed by Naidu et al. (2017), the Lyman break sits squarely in the middle of the F275W bandpass. Since both ionizing and non-ionizing photons contribute to each

object's F275W photometry, a number of modeling assumptions are needed to sift out the contribution of just the LyC to the F275W flux.

However, if one were to push to slightly higher redshifts, say  $z \gtrsim 2.4$ , as we did in the GOODS-N in Jones et al. (2018, hereafter J18), then the F275W filter becomes sensitive to LyC photons *only*. In that work, we identified a raw total of six sources with spectroscopic redshifts  $z \gtrsim 2.4$  that remained bright in F275W. However, four of these were then shown via optical spectroscopy to be line-of-sight blends of low- and high-redshift galaxies.

In this paper, we turn our attention to the GOODS-S, using the wealth of optical/IR spectroscopy in this field in concert with deep F275W imaging from the HDUV survey, to search for individual candidate LyC-leaking galaxies at z > 2.35. We place constraints on the mean LyC signal at this redshift using an averaging analysis and on the contributions to the overall ionizing luminosity density from SFGs. In Section 3.2, we describe the data we used to select and characterize potential high-redshift LyC leakers, including optical/IR redshift catalogs and spectra, and UV, X-ray, and optical imaging. We present our search for individual candidate LyC leakers in Section 3.3 and discuss the properties of our candidate sources, along with evidence for or against contamination by foreground galaxies for each. In Section 3.4, we perform an averaging analysis of all z=2.35-3.05sources with F275W coverage in the GOODS-N, in the GOODS-S, and in the two fields combined, from which we measure their total F275W contributions. In Section 3.5, we stack the F275W and F336W images for each GOODS field and for the two fields combined—first for z = 2.35 - 3.05, and then for three redshift bins for the combined images to look for differences that might arise due to "dilution" from Lyman absorption along the line-ofsight, which increases with redshift. In Section 3.6, we estimate the metagalactic ionizing background at 2.35 < z < 3.05 and compare to the flux required to maintain an ionized IGM at these redshifts. Finally, we summarize our findings in Section 3.7.

We assume  $\Omega_M = 0.3$ ,  $\Omega_{\Lambda} = 0.7$ , and  $H_0 = 70 \text{ km s}^{-1} \text{ Mpc}^{-1}$  throughout this work. All magnitudes are given in the AB system; magnitude zero-points for the HDUV F275W and F336W observations are given in Oesch et al. (2018).

#### 3.2 Data

#### 3.2.1 **F275W** Imaging

The HDUV survey (GO13872; Oesch et al. 2018) is a 132-orbit WFC3 imaging program centered on the GOODS-North and South fields. Designed to capitalize on existing WFC3/UVIS imaging from the CANDELS (Grogin et al. 2011; Koekemoer et al. 2011) and UVUDF (Teplitz et al. 2013; Rafelski et al. 2015) programs, the HDUV survey imaged both of the GOODS fields in the F275W and F336W filters around or within the existing CANDELS and UVUDF footprints.

We explored the HDUV GOODS-N dataset in J18. Here we focus on the HDUV GOODS-S dataset, which includes one science image per filter and corresponding maps of the per-pixel rms, all drizzled to a 60 mas pixel resolution. The final HDUV images incorporate data from the UVUDF survey, which substantially deepens this region of the field. We do not include data from the region of the CDF-S field observed by the Early Release Science (ERS; Windhorst et al. 2011). This area is almost a magnitude shallower in F275W than the regions that we use, and it contains significantly more artifacts; thus, we are unable to construct a high-significance < 26 magnitude sample for that region.

When measuring our F275W fluxes (see Section 3.3.1), we smoothed the F275W and F336W images using the scipy.ndimage.gaussian\_filter function with a standard deviation of 2 to minimize the impact of residual noise on our measurements, though as we will show, these residuals still contribute significantly to our flux uncertainties.

#### 3.2.2 Optical/NIR Spectroscopy

Secure spectroscopic redshifts are required for reliable identification of LyC-leaking candidates, as photometric redshift estimates and by-eye inspections are frequently contaminated by galaxies along the line-of-sight (e.g., Vanzella et al. 2010a; Siana et al. 2015; J18). We therefore narrow our search only to those galaxies with robust spectroscopic redshifts between 2.35 and 3.05. At the lower redshift bound, the Lyman limit sits at 3055.2 Å, at which point the total throughput of the F275W filter has declined to 2.3% on the red side. Adopting a slightly stricter redshift minimum of z = 2.37, at which point the Lyman limit sits at 3073.4 for a total F275W throughput of 1%, does not remove any of our candidates, nor does it substantially change the results of our stacking analyses in Section 3.4.

Similarly, the upper redshift bound relates to the wavelength at which the F336W filter probes only the redshifted LyC. Although we considered F275W-bright candidates with redshifts up to z=3.55 in the GOODS-N in J18, in this work we use z=3.05 as the upper redshift bound in both the GOODS-N and GOODS-S subsamples for consistency. In principle, ionizing sources at z>3.05 could also be detected in F336W using the methods described below, though the rapidly increasing opacity of the IGM to LyC photons at z=3-4 would make such a search somewhat more difficult (e.g., Inoue et al. 2014). Since the LyC is redshifted fully into the F275W bandpass at 2.35 < z < 3.05, the deep and relatively wide F275W coverage provided by the HDUV survey enables us to search for potential sources of ionizing radiation at high redshift.

We consulted spectroscopic catalogs from the literature (Popesso et al. 2009; Balestra et al. 2010; Cowie et al. 2012; Kurk et al. 2013; Morris et al. 2015; Bacon et al. 2017; Inami et al. 2017; Pentericci et al. 2018; Barger et al. 2019; Urrutia et al. 2019), along with

unpublished spectra that we have obtained with Keck/DEIMOS, to identify sources in the GOODS-S in the redshift range of interest. We limited ourselves to objects with redshifts marked as high-quality/confidence by the respective authors. For example, we only included spectroscopic redshifts from the MUSE-Deep and MUSE-Wide surveys that are flagged as confidence level 3, which represent unambiguous, multiple-line detections (for MUSE-Deep; Bacon et al. 2017 and Inami et al. 2017) or identifications with "very high certainty" (for MUSE-Wide; Urrutia et al. 2019).

Our final list of candidates (see Section 3.3.1) has spectroscopic redshifts from the MUSE-Deep program and from the catalogs of Balestra et al. (2010) and Kurk et al. (2013).

#### 3.2.3 X-ray Imaging

To identify X-ray counterparts to our F275W sample (see Section 3.3.1) and to weed out probable AGN, we used X-ray data and catalogs from the 7 Ms Chandra X-ray Observatory exposure of the Chandra Deep Field-South (Luo et al. 2017), which reaches a limiting flux of  $f_{0.5-2\text{keV}} \approx 6.4 \times 10^{-18} \text{ erg cm}^{-2} \text{ s}^{-1}$  near the image center. There are 95 F275W sources with X-ray counterparts within a 1".5 search radius. We computed the rest-frame 2 – 8 keV luminosities,  $L_X$ , of these counterparts from the 0.5 – 2 keV fluxes with an assumed  $\Gamma = 1.8$  and no absorption correction using

$$L_X = 4\pi d_L^2 f_{0.5-2\text{keV}} \left(\frac{1+z}{4}\right)^{\Gamma-2} \text{erg s}^{-1}.$$
 (3.1)

Of the sources with X-ray counterparts, four have  $L_X > 10^{42}$  erg s<sup>-1</sup>, which classifies them as AGN. One of these is a BALQSO. However, none of our candidate high-redshift LyC-leaking sample (defined below) have X-ray counterparts.

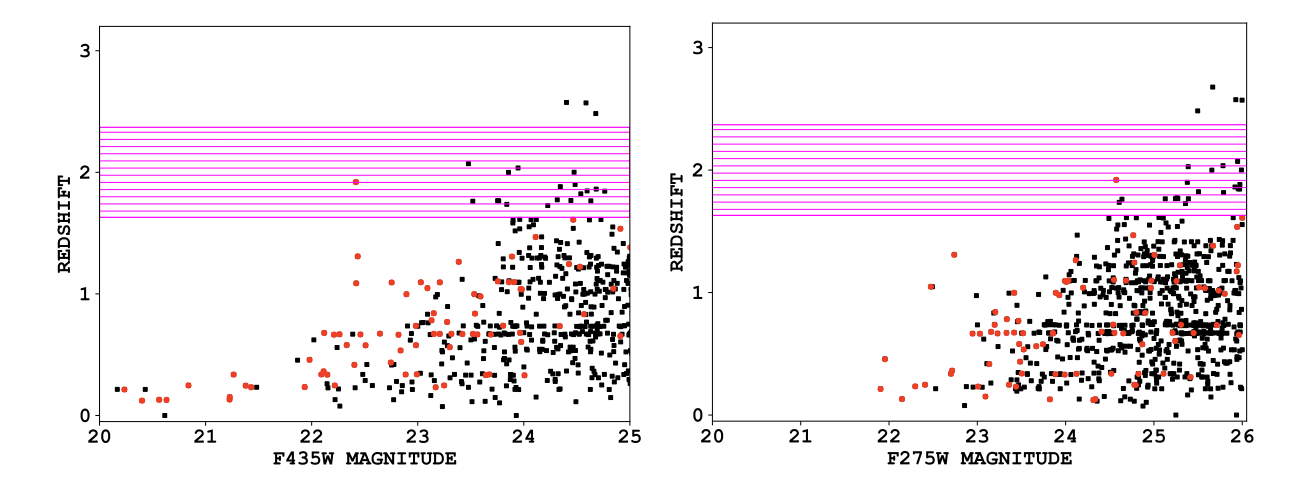


Figure 3.1: Top: Spectroscopic redshift vs. HST/ACS F435W magnitude for all galaxies in the 43.5 arcmin<sup>2</sup> footprint of the HDUV GOODS-S with F850LP < 26, which defines our parent sample. Bottom: Spectroscopic redshift vs. HST/WFC3 F275W magnitude for our primary UV sample of 1115 sources in the GOODS-S with F275W magnitudes < 26 and total errors fainter than 27.19, corresponding to a  $3\sigma$  detection. Red circles mark sources with an X-ray counterpart in the Chandra Deep Field South 7 Ms catalog. The purple shaded region shows the redshift interval where the F275W bandpass straddles the Lyman limit. The four >  $3\sigma$  LyC-leaking candidates lie above this region.

## 3.3 Search for Individual $z\sim 3$ Candidate LyC Leakers in the GOODS-S

J18 describes our search for LyC-leaking candidates in the HDUV GOODS-N field. In the GOODS-S, we begin with all F850LP < 26 galaxies that are covered by the  $43.5 \text{ arcmin}^2$  footprint of the HDUV observations. This area lies entirely within the GOODS-S observations of Giavalisco et al. (2004) obtained with HST's Advanced Camera for Surveys (ACS). At  $z \sim 2.5$ , the ACS F850LP filter probes the rest-frame FUV at  $\sim 2500$  Å, providing a reasonable selection of star-forming galaxies at these redshifts. In the top panel of Figure 3.1, we plot redshift versus F435W magnitude for this area. Spectroscopic identifications are 97% complete below F435W = 24, 85% from F435W = 24-24.5, and 63% from F435W = 24.5-25.

#### 3.3.1 F275W Measurements in the GOODS-S

Using the Python Source Extraction and Photometry (SEP) library<sup>1</sup> (Barbary 2016), which is based on the SExtractor program of Bertin & Arnouts (1996), we measured F275W fluxes in 2" and 4" diameter apertures at the position of each F850LP < 26 source with UV coverage. We also estimated the local median background at each source position in a 4-8" diameter annulus and subtracted this from the aperture fluxes. Comparing background-subtracted small- and large-aperture magnitudes (for extended objects with 21 < F275W < 25, to avoid saturated or low S/N sources) reveals a median offset of -0.18 mag, which we added back to the 2" magnitudes as an aperture correction.

We initially measured magnitude errors in 2" apertures from the associated rms noise files, with the same -0.18 mag aperture correction applied. However, this resulted in the selection of objects that, though they are detected nominally at moderate (>  $3\sigma$ ) significance in F275W, appeared to be pure noise upon visual inspection.

To estimate the effect of residual noise in the science maps on our flux measurements, we performed the same aperture photometry methods described above at  $\sim 10,000$  random positions across the HDUV field in both the F275W science and rms images, with the same smoothing applied for consistency with our source flux measurements. If we were to use only the rms image to determine uncertainties, we would underestimate the true noise by a factor of 2. This translates to an offset of -0.376 mag, which we added to our initial magnitude errors.

Our primary UV sample consists of 1115 sources with F275W magnitudes brighter than 26 and total errors fainter than 27.19, corresponding to a  $> 3\sigma$  detection. In the bottom panel of Figure 3.1, we show redshift versus F275W magnitude for this sample.

<sup>&</sup>lt;sup>1</sup>https://github.com/kbarbary/sep

Spectroscopic identifications are nearly fully complete to F275W = 24.5 (with only two sources out of 248 missing or unidentified), 92% complete from F275W = 24.5 – 25, and 57% complete from F275W = 25 – 26. The rapid drop-off in spectroscopic completeness at fainter UV magnitudes is a major motivation for our F275W = 26 cutoff, even though one might expect the number of candidate  $z \sim 2.5 - 3$  LyC leakers to increase at very faint UV magnitudes. We have four LyC-leaking candidates in the redshift range 2.35 < z < 3.05 from this selection.

Requiring a >  $3\sigma$  detection in F275W at the depth of the HDUV imaging will necessarily miss UV-fainter sources that otherwise may merit further consideration as LyC-leaking candidates. We therefore used the following color selection as a secondary way of selecting potential LyC leakers. We required (1) F435W < 25; (2) F606W - F850LP < 1 mag; and (3) F275W signal-to-noise ratio (SNR) > 2. The first condition ensures that this color-selected sample remains fairly spectroscopically complete, while the other conditions select sources with at least marginal F275W detections and relatively flat rest-frame, non-ionizing UV continua. As shown in Figure 3.2, this selection yields four candidates above our minimum redshift threshold, three of which were already selected directly using our >  $3\sigma$  criterion. The remaining source (enclosed in the green circle in Figure 3.2) is detected at 2.6 $\sigma$  in F275W.

In summary, we have identified five candidate high-redshift LyC leakers in the redshift range 2.35 < z < 3.05 in the GOODS-S, four of which are detected at  $> 3\sigma$  significance in F275W. With a total of 46 sources with UV coverage and secure redshifts in the redshift range, this leads to a  $\sim 10.9\%$  raw success rate in identifying candidate LyC-leaking galaxies. However, after removing two candidates contaminated by foreground galaxies (see Section 3.3.2), this success rate drops to  $\sim 6.5\%$ .

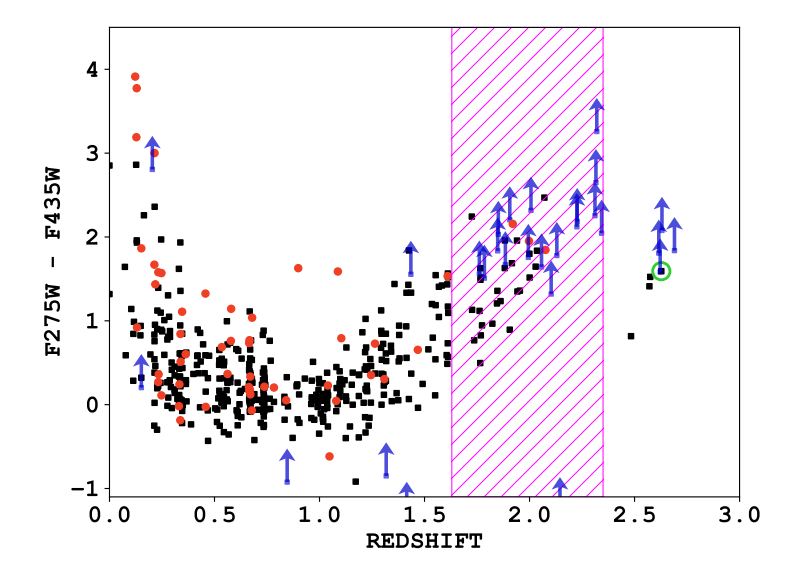


Figure 3.2: F275W – F435W color vs. spectroscopic redshift for sources with relatively flat rest-frame UV continua. Red circles mark sources with an X-ray counterpart in the Chandra Deep Field South 7 Ms catalog. Sources with lower limits on F275W – F435W are plotted at their  $2\sigma$  values with blue arrows. The open green circle marks the single 2.35 < z < 3.05 source detected at  $> 2\sigma$  significance in F275W that was not already selected with our  $> 3\sigma$  significance criterion. The purple hatched region shows the redshift interval where the F275W bandpass straddles the Lyman limit.

#### 3.3.2 Five Candidate LyC Leakers in the GOODS-S

In Table 3.1, we list the basic properties of our five candidate LyC leakers in the GOODS-S. This includes an ID number, identical to those given in Table 3 of Guo et al. (2013); decimal coordinates; a spectroscopic redshift from ground-based observations; the F275W magnitude and error (including the -0.18 mag aperture correction and -0.376 mag noise correction); F435W magnitude; and F606W – F850LP color. In Figure 3.3, we show both a three-color thumbnail (left; red = F160W, green = F850LP, blue = F435W) and the F275W thumbnail (right) of each source.

Although we selected our candidates to have high-quality spectroscopic redshifts from 2.35 < z < 3.05, the optical spectra for two sources (objects 9890 and 20277 in Table 3.1) show evidence of an intermediate redshift galaxy along the line-of-sight to the high-redshift galaxy. In source 9890, this is betrayed by the presence of an  $[OIII]\lambda\lambda4959, 5007/H\beta$ 

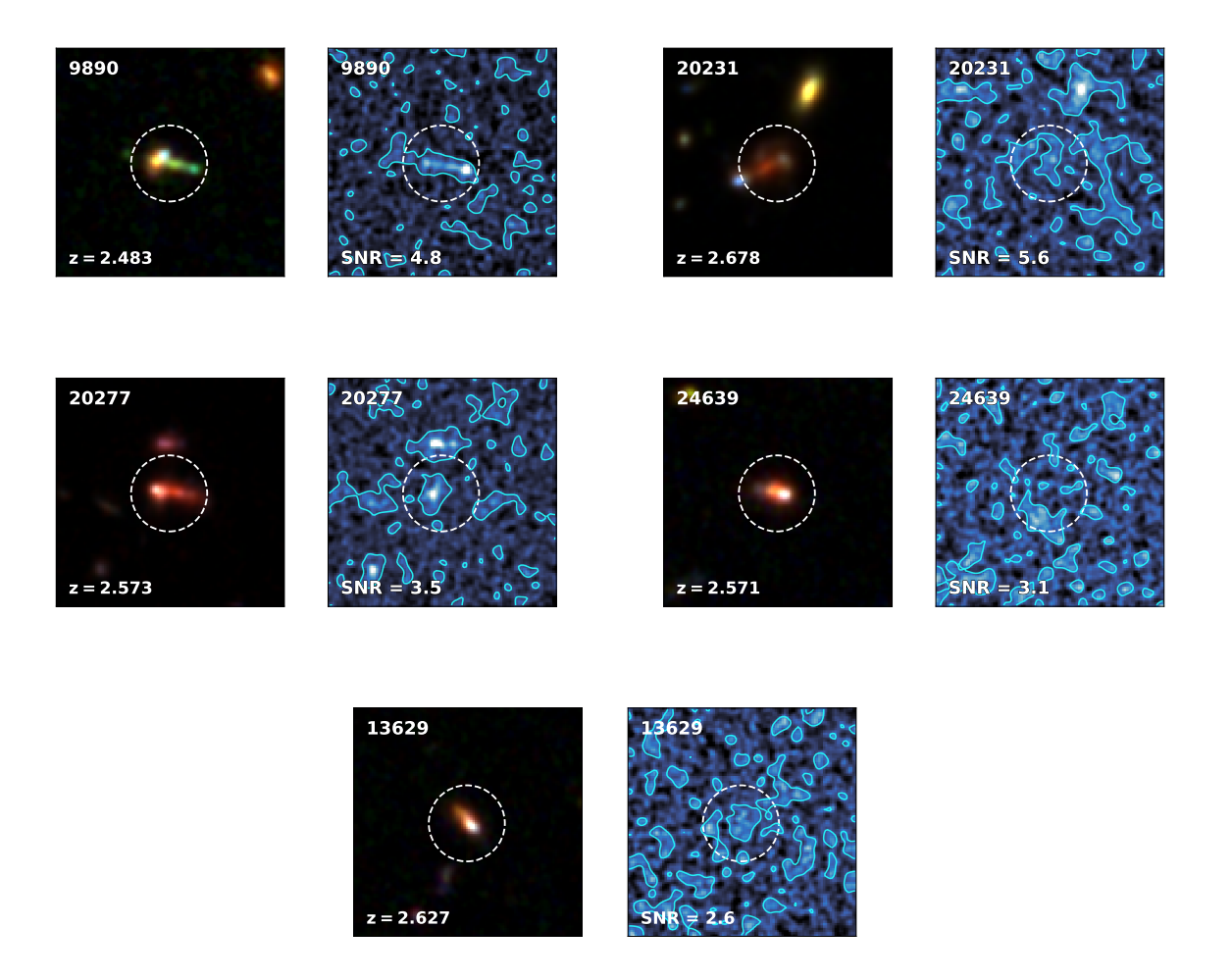


Figure 3.3: Three-color images (left; red = F160W, green = F850LP, and blue = F435W) and F275W thumbnails (right) of our five candidate LyC leakers. Cyan contours show regions where the F275W per-pixel SNR exceeds  $5\sigma$ , and the white dashed circle shows the 2" diameter aperture used in measuring the magnitudes. Images are 6" on a side; North is up and East is to the left. For each source, the redshift (F275W SNR) is given at the bottom of the left (right) image. Sources 9890 and 20277 were found to be contaminated by low-redshift interlopers.

complex at z=0.784. In source 20277, we see a strong [OII] $\lambda\lambda 3727,3729$  doublet at z=1.094. At these intermediate redshifts, the F275W filter probes the rest-frame FUV at  $\sim 1300-1500$  Å, well above the Lyman limit. The UV fluxes for these two sources are almost certainly dominated by the foreground galaxies and hence cannot be used to measure the ionizing flux output at  $z\sim 2.5$ .

 $ID^a$ R.A. Dec. F275W (Error) F435W F606W - F850LP $9890^{1}$ -27.772339 25.50 (27.21) 53.096661 2.48324.680.57 $20231^{2}$ 53.157532 -27.798981 2.678 25.67 (27.54) 25.49 0.33  $20277^3$ 53.157845 -27.814756 2.573 25.93 (27.30) 24.40 0.39  $24639^3$ -27.829344 53.188301 2.57126.00 (27.22) 24.58 0.21 $13629^1$ 53.118439 -27.805323 2.62726.18 (27.24) 24.590.16

Table 3.1 : Summary of Candidate LyC Leakers

Note—<sup>a</sup>Object IDs are the same as in Table 3 of Guo et al. (2013). Sources with ID numbers in bold were later confirmed to be contaminated by foreground galaxies upon inspecting their spectra.

We note that these contaminated galaxies, particularly object 9890, reinforce the need for deep optical and NIR spectroscopy to confirm the nature of any proposed LyC leakers. In the case of object 9890, the photometric redshift without HDUV data ( $z_{phot} = 0.698$ ; Momcheva et al. 2016) is more consistent with the spectroscopic redshift of the foreground, low-redshift galaxy. Yet once the HDUV data are included, the photometric redshift better matches the spectroscopic redshift of the background galaxy ( $z_{phot} = 2.36$ ; Oesch et al. 2018), meaning a selection based only on photometric redshifts would falsely label this source as a LyC leaker.

We now briefly discuss our remaining three candidate LyC leakers in the GOODS-S and the foreground contamination rate in our overall candidate sample. First, three distinct components are seen in the three-color thumbnail for source 20231 (upper-right of Figure 3.3): a generally red galaxy with two clumps, both of which are at almost-identical spectroscopic redshifts (R. Bacon, private communication), though it is unclear whether they constitute a single galaxy or an interacting pair. In any case, the F275W flux is not coincident with the blue clump to the southeast, but instead with the relatively red knot of emission near the image center.

<sup>&</sup>lt;sup>b</sup>Spectroscopic redshifts from (1) GMASS (Kurk et al. 2013), (2) MUSE-Deep (Bacon et al. 2017; Inami et al. 2017), or (3) Balestra et al. 2010.

Second, in source 24639 (middle-right of Figure 3.3), the F275W emission is offset from the position of the non-ionizing flux from this galaxy by  $\sim 0''.8$ , which corresponds to about 6.4 proper kpc at z=2.571. Though regions of LyC escape may not always be fully coincident with the bulk of the stellar emission, the lack of non-ionizing flux at the position of the F275W emission in this source is unusual. We do not remove this object from the list of LyC candidates, but in subsequent sections we note the effects of excluding it from our calculations.

Third, there is a similar off-center clump of F275W emission to the east of source 13629. However, unlike the case for source 24639, object 13629 also shows hints of F275W emission coincident with the position of the non-ionizing flux from this galaxy.

To estimate the expected level of foreground contamination, we ran Monte Carlo simulations to randomize the positions of all galaxies in the HDUV GOODS-S field, regardless of redshift identification or F275W magnitude. This assumes a spatially uniform foreground F275W population with a surface density of around 486,900 deg<sup>-2</sup> (the number of galaxies within the HDUV GOODS-S footprint divided by its 43.5 arcmin<sup>2</sup> area), similar to the assumptions in Vanzella et al. (2010a). For a sample size of 5, at least one galaxy is contaminated in 27% of our 500 simulations, with a mean of  $0.3 \pm 0.6$  contamination events. This is consistent with expectations from a simple binomial probability distribution, in which the probability of any single contamination event is proportional to the source surface density and the aperture size (Nestor et al. 2013). For the surface density given above and an aperture of radius 1", an average of  $0.48 \pm 0.66$  contamination events are expected in a sample of size 5.

Finally, we must also be concerned about the limitations of our sample selection in that we are only using sources with known spectroscopic redshifts. As we have argued above, it is dangerous to use photometric redshifts, which may be biased against continuum leakers, and where sources with incorrect high redshifts may also result in incorrect high fluxes. However, we have inspected the 185 SFGs that would be placed in the z=2.35-3.05 redshift range by the Straatman et al. (2016) catalog of photometric redshifts in the field and do not have spectroscopic redshifts. These have only two  $3\sigma$  F275W detections and no significant total signal ( $-0.25 \pm 0.58 \mu Jy$ ).

Although the apparent offsets between the ionizing and non-ionizing radiation in some of these sources (particularly object 24639) are peculiar, we retain all of these objects as candidate LyC leakers. We emphasize that an absence of evidence for contamination by foreground galaxies does not equate to positive evidence that such foreground contaminants are absent. For this reason and out of an abundance of caution, we assert that our three remaining sources in the GOODS-S should only be considered LyC-leaking candidates.

# 3.4 Mean ionizing emission from an averaging analysis using both GOODS fields

In addition to searches for individual LyC leakers, the depth and breadth of UV coverage offered by the HDUV data enable a robust measurement of the "typical" ionizing flux output of  $z\sim 2.5$  galaxies via averaging.

We select all 2.35 < z < 3.05 galaxies with high-quality spectra that lie within the F275W footprint of the HDUV survey in both GOODS fields. For each field and band subsample, we applied the same photometric procedure that we used in our search for individual candidate LyC leakers in Section 3.3.1 in order to determine the flux and error for all the sources, including those not detected individually. In Figure 3.4, we show F275W flux versus F850LP magnitude for our F275W subsamples in the GOODS-S and the GOODS-N.

We next excluded sources with X-ray counterparts and sources whose spectra clearly

include emission features from a line-of-sight foreground contaminant. The X-ray non-detection criterion precludes any major contributions from AGNs to our stacks. For the GOODS-S, we use the 7 Ms *Chandra* Deep Field-South catalog (Luo et al. 2017; see Section 3.2.3). For the GOODS-N, we use the 2 Ms *Chandra* Deep Field-North catalog (Alexander et al. 2003; Xue et al. 2016). We also searched for any objects with very nearby (< 2") projected neighbors that might affect our aperture flux measurements, but we did not find any. Our upper redshift bound is approximately the redshift at which the F336W filter begins to probe only rest-frame wavelengths < 912 Å.

We then computed the error-weighted mean flux of all the sources in each subsample and multiplied that value by the number of sources in the subsample. Because the flux errors for our sources are very similar to one another, this is quite similar to computing an unweighted sum. In the GOODS-S, this selection yielded 38 sources. In the GOODS-N, where the areal coverage in F275W is wider than in F336W, this yielded 91 sources with F275W coverage and 69 sources with coverage in both bands. In Table 3.2, we summarize the measured properties for the individual and combined GOODS fields.

In the GOODS-S, the overwhelming majority of the total contribution at F275W (0.46  $\mu$ Jy of 0.51  $\mu$ Jy) comes from the three candidate LyC leakers listed in Table 3.1. If we remove individual candidates from the stack (specifically, source 24639, which appears to have no non-ionizing emission coincident with its F275W detection), the total F275W flux drops to 0.42  $\mu$ Jy, of which 0.32  $\mu$ Jy is attributable to the remaining two candidates. Removing all three candidates from the stack reduces the error-weighted mean to 0.002  $\pm$  0.006  $\mu$ Jy, giving a total contribution of only 0.070  $\pm$  0.21  $\mu$ Jy.

In order to check the background, we randomized the positions of the GOODS-S subsample and measured the magnitudes at these positions. We then processed the sample in the same way as the real sample, i.e., by eliminating low redshift sources, X-ray sources,

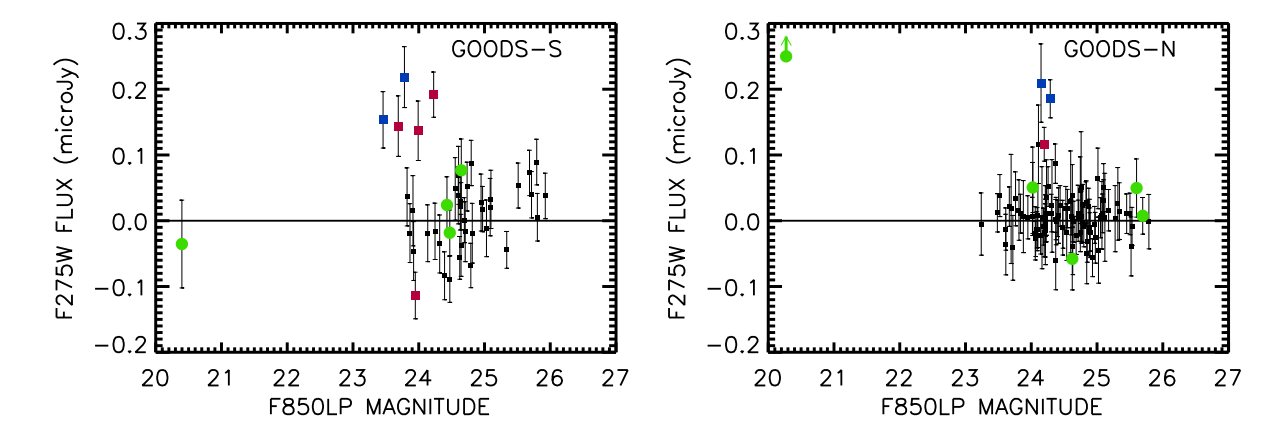


Figure 3.4: F275W flux vs. F850LP magnitude for all 2.35 < z < 3.05 galaxies with high-quality spectra that lie within the F275W footprint of the HDUV survey in the GOODS-S (top) and GOODS-N (bottom). Sources with X-ray counterparts are marked in green, while  $> 3\sigma$  detections, both positive and negative, are marked in either red or blue (the latter is used to indicate sources contaminated by foreground galaxies). Note that GN-UVC-6 is a  $2.9\sigma$  source and hence not marked in red in the lower panel. GN-UVC-1, the GOODS-N quasar shown in the lower panel, is marked in green with an upward pointing arrow, since its measured flux is much higher than the y-axis limit.

Table 3.2: Properties of the Error-Weighted Summed Fluxes

Field	F275W	(SNR)	F336W	(SNR)
	$(\mu Jy)$		$(\mu Jy)$	
GOODS-S	0.51	(2.3)	2.83	(21)
GOODS-N	0.52	(1.5)	6.74	(23)
Both	1.00	(2.5)	9.10	(30)

NOTE—The area covered in the GOODS-N in F336W is smaller than that in F275W.

or very nearby bright neighbors. We measured 120 random samples and found a mean background of  $0.070 \pm 0.023~\mu$ Jy, which is negligible compared with the measured value in the real sample. 15% of the random samples had mean backgrounds that exceeded the total contribution of the real sample, which may suggest that we are slightly underestimating the true noise. However, it should be emphasized that we did not carefully curate the random samples in the same way that we did the real sample, and, thus, we may have a higher degree of unrecognized foreground contamination, which could result in an overly

large dispersion.

Despite the greater number of sources in the GOODS-N, the total contribution at F275W is similarly small at just 0.52  $\mu$ Jy. As with the GOODS-S, a large fraction of the total contribution comes from just a small number of sources; here  $\sim 40\%$  (0.21  $\mu$ Jy) is attributable to just two sources. These are GN-UVC-6, a color-selected LyC-leaking candidate at z=2.439 that we discussed in J18 (a 2.9 $\sigma$  detection in F275W), and a z=2.98 galaxy with an F275W magnitude of  $\sim$ 26.21 (an  $\sim 3\sigma$  detection). The latter object was not discussed in J18 because we considered only high-redshift objects detected at  $\geq 4\sigma$  significance in constructing our F275W sample, and the source also did not turn up in our color-selected sample, which probed to lower significance. In any case, this leaves  $\sim 0.3 \ \mu$ Jy of F275W unaccounted for, which must come from the remaining 89 sources.

Finally, if we combine the two fields, we calculate a total contribution of 1.00  $\pm$  0.41  $\mu$ Jy at F275W, of which about 0.67  $\mu$ Jy is directly attributable to the five LyC-leaking candidates discussed above (3 in the GOODS-S and 2 in the GOODS-N). Removing an individual candidate from this calculation (specifically source 24639, for the reasons mentioned in Section 3.3.2) does not substantially change this result: the remaining 128 galaxies combined contribute 0.87  $\pm$  0.39  $\mu$ Jy, of which 0.53 is directly attributable to the remaining candidates. Given the error on the total contribution, both cases are consistent with the remainder of our sample contributing little or nothing to the overall ionizing flux output at  $z \sim 2.5$ .

## 3.5 An Image stacking visualization in both GOODS fields

For visualization purposes, in Figure 3.5, we show stacked images in each band for the sample in each GOODS field, as well as for both fields combined. Bright points more than 1" away from the image center (for example, the bright spot to the upper right in the

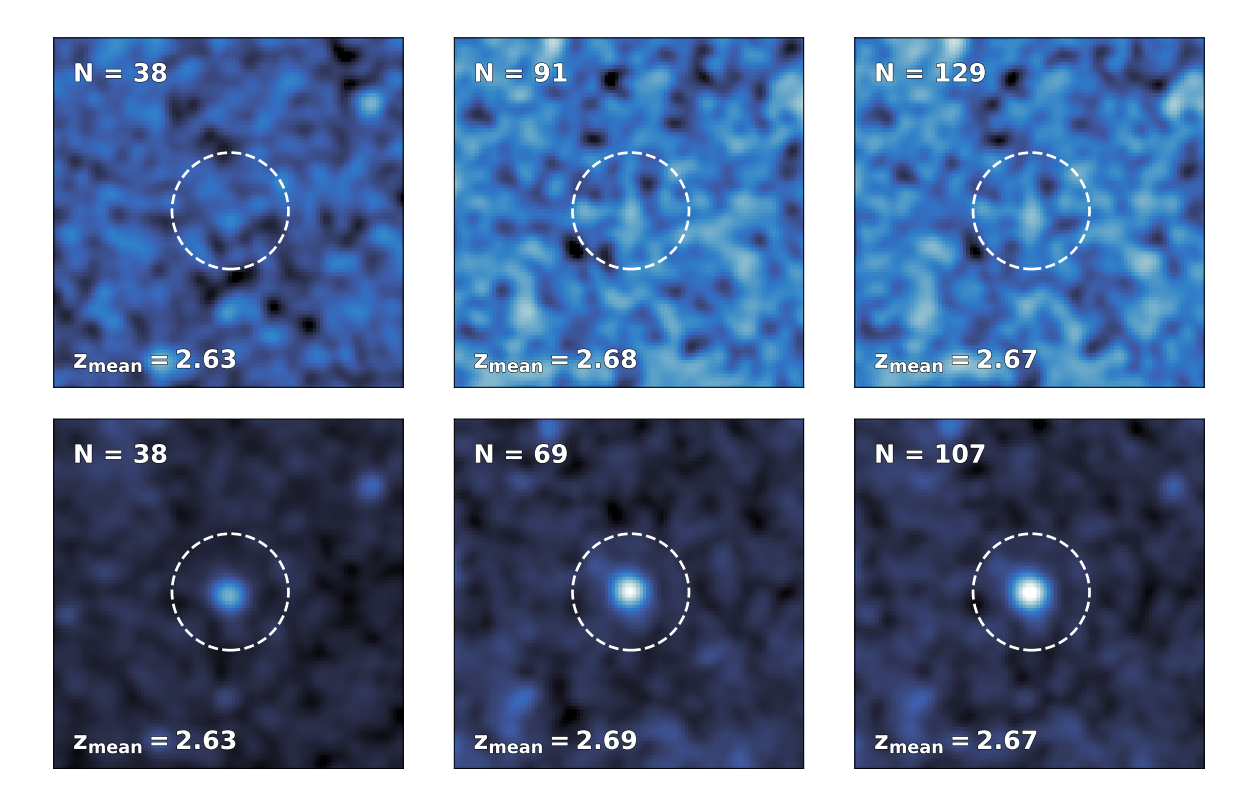


Figure 3.5 : F275W (top) and F336W (bottom) stacks of spectroscopically identified sources between 2.35 < z < 3.05 with UV coverage from the HDUV survey. Images from left to right show stacks from the GOODS-S, the GOODS-N, and both fields combined. Images are 6" on a side and stretched to the same pixel values for each band (except for the F336W image of the combined GOODS fields, which saturates at the color scale used for the individual fields). North is up and East is to the left. The differing number of sources in the GOODS-N stacks (middle column) are due to wider areal coverage of the field in F275W than in F336W.

first row of Figure 3.5) are likely foreground galaxies with significant F275W flux, though these do not affect our measurements at z > 2.35. Most of our candidate LyC leakers across both fields lie at  $z \sim 2.4 - 2.7$ , just above our redshift threshold of 2.35. At higher redshifts, it is increasingly likely that a Lyman limit system along some line-of-sight will wipe out any emergent ionizing flux, leading to a greater number of non-detections (see Section 3.6). Because of this, it is possible that including sources at the higher-redshift end of the range we probe here in the stacks could "dilute" some underlying average signal from sources at the lower-redshift end.

To test this, we broke apart our stacks for the combined GOODS fields into three redshift bins, each with equal numbers of galaxies, and performed the same analysis. At F275W, we found nondetections in all three redshift bins. This suggests that the "dilution" does not affect our ability to detect possible LyC-leaking galaxies at the depth of the HDUV F275W data. Meanwhile, the stacked detection in F336W remains fairly strong in all three redshift bins, dropping from SNR = 21.6 in the lowest-redshift bin to SNR = 5.7 in the highest, where most of the band now probes the rest-frame Lyman continuum.

In summary, we are left with (1) a handful of candidate LyC-leaking galaxies that appear to be individually detected at moderate significance (at the  $\gtrsim 3\sigma$  level), and (2) a general population of galaxies that are essentially invisible at LyC wavelengths, even in stacked images. This has some parallels to the results of the LACES program (Fletcher et al. 2019), which used deep WFC3/UVIS imaging in F336W of the SSA22 field to search for  $z \sim 3.1$  LyC leakers that are also Ly $\alpha$  emitters and Lyman break galaxies. While they successfully detect significant LyC flux in  $\sim 20\%$  of their targets, the majority of their sources (42 of 54) are faint in F336W (SNR < 4). Stacking these non-detections yielded no net signal, with an upper limit of F336W = 31.8 (3 $\sigma$  in a 0.12"aperture). This led the authors to conclude that detection of LyC emission in their sample is dichotomous, occurring either fairly strongly in individual sources or not at all.

However, we note two important differences in methodology that distinguish this work from Fletcher et al. (2019). First, their high success rate in identifying LyC leakers (for comparison, we have a  $\sim 6.5\%$  success rate in the GOODS-S—that is, three candidates out of 46 total sources with robust redshifts in the z=2.35-3.05 range and with UV coverage) can be attributed largely to (1) the depth of their F336W exposures compared to the typical depth of an HDUV pointing ( $\sim 30$  mag at  $3\sigma$  in a 0".12 diameter aperture in LACES vs.  $\sim 27.5$  mag at  $5\sigma$  in a 0".4 diameter aperture in HDUV), and (2) the higher

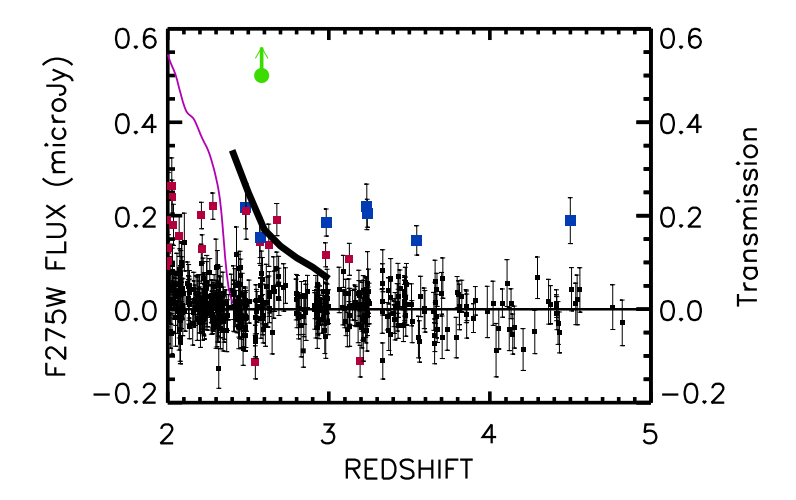


Figure 3.6: F275W flux vs. redshift for the 129 galaxies with high-quality spectroscopic redshifts and F275W coverage in both GOODS fields. The quasar in the GOODS-N (GN-UVC-1 from J18) is marked in green with an upward pointing arrow, since its measured flux is much higher than the y-axis limit. The red and blue squares are all the  $> 3\sigma$  detections, positive or negative, with the blue denoting contamination by foreground galaxies. Note that GN-UVC-6 is a 2.9 $\sigma$  source and hence not marked in red. Thus, there are five  $> 3\sigma$  LyC-leaking galaxy candidates in the redshift range 2.35 < z < 3.05. The thick black curve shows the transmission over this redshift range (right-hand y-axis scale), which drops rapidly as one moves to higher redshifts. The purple curve shows the F275W filter transmission at the LyC edge as a function of redshift. The y-axis units are arbitrary. Above z = 2.35, we will only have LyC photons within the filter.

throughput in F336W compared to F275W, which partially offsets the rising opacity of the IGM to LyC photons at z>3. Second, their HST/WFC3 followup was highly targeted, focusing on a set of sources that were already known to have high Ly $\alpha$  equivalent widths and large O32—both of which may correlate with LyC escape (Nakajima & Ouchi 2014; Izotov et al. 2016a,b, 2018; Micheva et al. 2017; Marchi et al. 2018; Steidel et al. 2018). In contrast, the sample presented here is virtually blind to such selection effects, since we require only that a source be reasonably bright in F275W and that it have a spectroscopic redshift.

## 3.6 Contributions to the Metagalactic Ionizing Background

Determining the absolute escape fraction for each of our candidate LyC leakers is challenging, if not impossible, without reliable knowledge of each source's intrinsic spectral energy distribution (SED) and degree of reddening. Instead, we consider the extent to which our candidate sample contributes to the metagalactic ionizing background. To do so, we combine the GOODS-N and the GOODS-S data. Excluding the spectroscopically contaminated sources, we have a total of 129 SFGs together with 9 AGNs based on the X-ray properties. We have identified six of these as candidate LyC leakers. These consist of a single quasar (the LyC-luminous source GN-UVC-1 from J18) and the five SFGs described in Section 3.4. GN-UVC-1 dominates the flux in the two fields with a F275W flux of 2  $\mu$ Jy, roughly twice the contribution of all of the SFGs even when including the candidate LyC leakers (1.00  $\pm$  0.41  $\mu$ Jy). The remaining AGNs contribute only an insignificant total of 0.096  $\mu$ Jy. Because of the sparseness of the luminous AGNs, the fields are too small to make an accurate estimate of the AGN contributions, and we focus solely on the SFGs.

We converted each SFG's F275W flux density to an ionizing volume emissivity,  $\epsilon_{900}$ , defined as the luminosity density at 900 Å per unit frequency, divided by the comoving survey volume based on (1) the total survey area in F275W (131 arcmin<sup>2</sup>) and (2) the redshift bounds 2.35 < z < 3.05. We simplified our calculations by assuming that the entirety of each SFG's F275W flux falls at the filter's effective wavelength of  $\sim 2714$  Å, or rest-frame  $\sim 750$  Å. We further assumed that the emergent SEDs of these galaxies are flat in frequency space (i.e.,  $f_{\lambda} \propto \lambda^{\beta}$  with  $\beta = -2$ ) both blueward and redward of 912 Å, albeit with different amplitudes on each side of the Lyman limit. While a shallower spectral slope at  $\lambda_{rest} < 912$  Å may be more plausible, the assumption of a spectrally flat LyC allows us to use our measured flux densities "as-is", without the need for scaling to 900 Å, which

would only increase our calculated values of  $\epsilon_{900}$ . This assumption thus allows us to remain as conservative as possible when estimating the ionizing emissivities.

Intergalactic transmission losses are substantial for the higher redshift galaxies seen in the F275W band, and these losses need to be taken into account in computing the ionizing emissivity. Below the LyC wavelength, the opacity is dominated by sources with N(HI) column densities near the Lyman limit ( $\log N(HI) = 17.2 \text{ cm}^{-2}$ ). Because the number of absorbing systems is small, there is a wide variation in the mean flux in the F275W filter, after intergalactic absorption, relative to the galaxy flux at rest-frame 900 Å (e.g., Inoue et al. 2014 and references therein). The transmission also drops rapidly with increasing galaxy redshift as the intergalactic path length increases.

In order to compute the transmission correction, we ran Monte Carlo simulations, assuming the number of N(HI) systems per unit N(HI) is a power law with index -1.7, and the number of Lyman limit systems with  $\tau > 1$  per unit dz is given by the analytic form  $2.8 \times ((1+z)/4.5)^{1.94}$  of Songaila & Cowie (2010). In Figure 3.6, we show the mean flux in the F275W filter relative to the galaxy flux at rest-frame 900 Å versus redshift, which drops from 0.37 at z=2.35 to 0.065 at z=3. Because of this rapid drop in the mean transmission, we have chosen to divide the sample into two redshift intervals in computing the corrected emissivity. We find a logarithmic value for  $\epsilon_{900}$  of  $25.0 \pm 0.3$  erg s<sup>-1</sup> Hz<sup>-1</sup> Mpc<sup>-3</sup> in the z=2.35-2.7 interval. Removing source 24639 from our calculation in the lower-redshift interval decreases the value of  $\log(\epsilon_{900})$  by about 0.15 dex.

The bulk of our ionizing flux (67%) comes from the five SFGs, with the remaining galaxies contributing only a small fraction. This is consistent with the results of Smith et al. (2018, 2020), who do not detect significant LyC emission in their own stacking analyses. This bimodality may be caused by favorable lines-of-sight through the ISM of the host galaxy (e.g., Cen & Kimm 2015) and/or the IGM rather than by the intrinsic

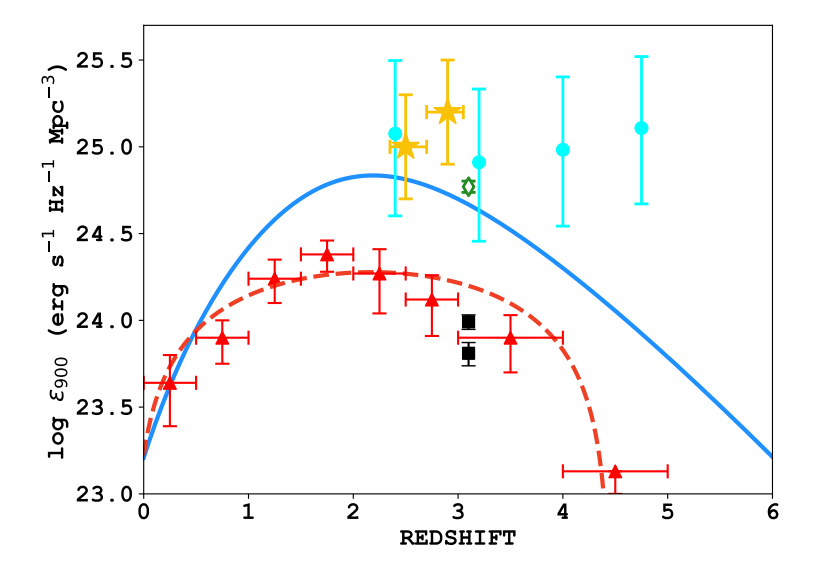


Figure 3.7: Ionizing volume emissivity at z=2.35-2.7 and z=2.7-3.05 estimated from our 5 LyC-leaking candidates together with our stacking analysis of the remaining z=2.35-3.05 galaxies in the combined HDUV-GOODS fields (filled gold stars). Horizontal error bars on our data points indicate the redshift range. To compare with literature observations of the ionizing emissivity from AGN, we show data points from Cowie, Barger, & Trouille (2009) and Micheva et al. (2017) (red triangles and black squares, respectively) and best-fit models from Cowie, Barger, & Trouille (2009) and Haardt & Madau (2012) (red and blue curves, respectively). For the contribution from SFGs, we show the data point from Steidel et al. (2018) (open green diamond). Cyan circles show the total inferred metagalactic ionizing luminosity density from Becker & Bolton (2013).

galaxy properties, with the small number of candidate LyC leakers corresponding to lines-of-sight with low IGM absorption. Even at z=2.35, 14% of the lines-of-sight have < 10% transmission in the F275W filter, and only 30% of the lines-of-sight have transmission above 50%, while at z=2.7, 48% of the lines-of-sight have < 10% transmission in the F275W filter, and only 5% of the lines-of-sight have transmission above 50%. This is consistent with the redshift distribution of the candidate LyC leakers (Figure 3.6), four of which lie in the lower-redshift interval (z=2.35-2.7).

In Figure 3.7, we summarize the results of our calculations and put them into context using other  $z\sim 3$  measurements of the ionizing background from the literature. The level of ionizing volume emissivity that we estimate from the SFGs is roughly consistent with

other recent estimates, such as that of Steidel et al. (2018) at slightly higher redshifts. It is above the AGN ionizing output measured by Cowie, Barger, & Trouille (2009), Haardt & Madau (2012), and Micheva et al. (2017) in large samples of quasars and broad-line AGNs at similar redshifts. Becker & Bolton (2013) used Ly $\alpha$  forest observations to infer the total ionizing background from 2 < z < 5. At z = 3.2, they estimated a nominal  $\log(\epsilon_{900}) = 24.9 \text{ erg s}^{-1} \text{ Hz}^{-1} \text{ Mpc}^{-3}$ , which is comparable to our estimates of  $\epsilon_{900}$  for the SFG ionizing background at these redshifts. However, we emphasize that there may be further contamination in our sample by intervening sources that we have not identified. Hence, the present values should be considered as upper limits.

## 3.7 Summary

We have presented a search for candidate LyC leakers at  $z \sim 2.5-3$  in the GOODS-S field using a combination of deep HST/WFC3 F275W imaging data from the HDUV survey (Oesch et al. 2018) and extensive optical/NIR spectroscopy. We found four candidate ionizing sources brighter than F275W = 26, plus one additional source just below this cutoff with very blue rest-frame UV colors. However, two of these five sources are contaminated by foreground lower redshift galaxies, as seen in their optical spectra, leaving only three possible candidate LyC leakers.

We performed an averaging analysis of all the sources with spectroscopic redshifts 2.35 < z < 3.05 in the HDUV areas in both the GOODS-S and GOODS-N and found that the total ionizing output of galaxies at these redshifts is dominated by just five individual candidate LyC leakers. These include the three GOODS-S sources described above, and two sources in the GOODS-N (one of which was presented in J18). Allowing for the very substantial effects of intergalactic absorption, we found that the volume ionizing flux roughly matches that required to ionize the IGM at these redshifts (Becker & Bolton 2013)

and is consistent with other recent estimates.

We thank R. Bacon and the MUSE-Deep team for providing MUSE spectra of some of our LyC-leaking candidates ahead of publication. Some figures in this work use colormaps from the Python package CMasher (van der Velden 2020). We gratefully acknowledge support from NSF grant AST-1715145, the William F. Vilas Estate, and the Kellett Mid-Career Award from the University of Wisconsin-Madison Office of the Vice Chancellor for Research and Graduate Education with funding from the Wisconsin Alumni Research Foundation (A. J. B.). Based in part on data obtained at the W. M. Keck Observatory, which is operated as a scientific partnership among the California Institute of Technology, the University of California, and NASA and was made possible by the generous financial support of the W. M. Keck Foundation. The authors wish to recognize and acknowledge the very significant cultural role and reverence that the summit of Mauna Kea has always had within the indigenous Hawaiian community. We are most fortunate to have the opportunity to conduct observations from this mountain.

Facilities: VLT (MUSE), DEIMOS (Keck II), Hubble

Software: astropy (Astropy Collaboration et al. 2018), Source Extractor for Python (Barbary 2016)

## A Statement of Work

Here are briefly outlined the contributions of all listed authors for this publication, in order of their listing in the journal article.

- Logan H. Jones: Devised methodology for the photometry, sample selection, and estimation of foreground contamination; led analysis of optical spectra and of the contribution of HDUV sources to the LyC luminosity density at  $z \sim 3$ ; primary contributor to the writing of this manuscript.
- Amy J. Barger: Provided spectroscopic data for candidate LyC sources; provided intergalactic LyC transmission calculations; suggested tests of the methodology; proofreading and revisions.
- Lennox L. Cowie: Provided spectroscopic data for candidate LyC sources; suggested tests of the methodology; proofreading and revisions.

#### References

Alexander, D. M., Bauer, F. E., Brandt, W. N., et al. 2003, AJ, 126, 539

Astropy Collaboration, Price-Whelan, A. M., Sipőcz, B. M., et al. 2018, AJ, 156, 123

Bacon, R., Conseil, S., Mary, D., et al. 2017, A&A, 608, A1

Balestra, I., Mainieri, V., Popesso, P., et al. 2010, A&A, 512, A12

Barbary, K. 2016, JOSS, 1, 58

Barger, A. J., Cowie, L. L., Capak, P., et al. 2003, ApJ, 584, L61

Barger, A. J., Cowie, L. L., Bauer, F. E., & González López, J. 2019, ApJ, 887, 23

Barrow, K. S. S., Robertson, B. E., Ellis, R. S., et al. 2020, ApJ, 902, 39

Becker, G. D. & Bolton, J. S., 2013, MNRAS, 436, 1023

Bertin, E. & Arnouts, S. 1996, A&ASupplement, 117, 393

Bolton, J. S., Haehnelt, M. G., Viel, M., & Springel, V. 2005, MNRAS, 357, 1178

Bolton, J. S. & Haehnelt, M. G. 2007, MNRAS, 382, 325

Bouwens, R. J., Illingworth, G. D., Blakeslee, J. P., & Franx, M. 2006, ApJ, 653, 53

Bouwens, R. J., Illingworth, G. D., Oesch, P. A., et al. 2012, ApJ, 752, L5

Bouwens, R. J., Illingworth, G. D., Oesch, P. A., et al. 2015, ApJ, 811, 140

Bouwens, R. J., Illingworth, G. D., Oesch, P. A., et al. 2015, ApJ, 803, 34

Cen, R. & Kimm, T. 2015, ApJ, 801, 25

Cowie, L. L., Barger, A. J., & Trouille, L. 2009, ApJ, 692, 1476

Cowie, L. L., Barger, A J., & Hu, E. M. 2010, ApJ, 711, 928

Cowie, L. L., Barger, A. J., & Hasinger, G. 2012, ApJ, 748, 50

Cowie, L. L., Barger, A. J., Bauer, F. E., & González-López, J. ApJ, 891, 69

Cristiani, S., Serrano, L. M., Fontanot, F., Vanzella, E., & Monaco, P. 2016, MNRAS, 462

2478

Faisst, A. L. 2016, ApJ, 829, 99

Faucher-Giguère, C.-A., Lidz, A., Hernquist, L., & Zaldarriaga, M. 2008, ApJ, 688, 85

Feng, Y., Di-Matteo, T., Croft, R. A., et al. 2016, MNRAS, 455, 2778

Finkelstein, S. L., Papovich, C., Ryan, R. E., et al. 2015, ApJ, 758, 93

Fletcher, T. J., Tang, M., Robertson, B. E., et al. 2019, ApJ, 878, 87

Fontanot, F., Cristiani, S., Monaco, P., et al. 2007, A&A, 461, 39

Fontanot, F., Cristiani, S., & Vanzella, E. 2012, MNRAS, 425, 1413

Fontanot, F., Cristiani, S., Pfrommer, C., Cupani, G., & Vanzella, E. 2014, MNRAS, 438, 2097

Giallongo, E., Grazian, A., Fiore, F. et al. 2019, ApJ, 884, 19

Giavalisco, M., Ferguson, H. C., Koekemoer, A. M., et al. 2004, ApJ, 600, L93

Grazian, A., Giallongo, E., Fiore, F., et al. 2020, ApJ, 897, 94

Grazian, A., Giallongo, E., Gerbasi, R., et al. 2016, A&A, 585, A48

Grazian, A., Giallongo, E., Paris, D., et al. 2017, A&A, 602, A18

Grogin, N. A., Kocevski, D. D., Faber, S. M., et al. 2011, ApJS, 197, 35

Grimes, J. P., Heckman, T., Aloisi, A., et al. 2009, ApJS, 181, 272

Guo, Y., Ferguson, H. C., Giavalisco, M., et al. 2013, ApJS, 207, 24

Haardt, F. & Madau, P. 2012, ApJ, 746, 125

Inami, H., Bacon, R., Brinchmann, J., et al. 2017, A&A, 608, A2

Inoue, A. K. 2010, MNRAS, 401, 1325

Inoue, A. K., Shimizu, I., Iwata, I., & Tanaka, M. 2014, MNRAS, 442, 1805

Ishigaki, M., Kawamata, R., Ouchi, M., et al. 2018, ApJ, 854, 73

Izotov, Y. I., Orlitová, I., Schaerer, D., et al. 2016, Nature, 529, 178

Izotov, Y. I., Schaerer, D., Thuan, T. X., et al. 2016, MNRAS, 461, 3683

Izotov, Y. I., Thuan, T. X., & Guseva, N. G. 2017, MNRAS, 471, 548

Izotov, Y. I., Worseck, G., Schaerer, D., et al. 2018, MNRAS, 478, 4851

Japelj, J., Vanzella, E., Fontanot, et al. 2017, MNRAS, 468, 389

Ji, Z., Giavalisco, M., Vanzella, E., et al. 2020, ApJ, 888, 109

Jones, L. H., Barger, A. J., Cowie, L. L., et al. 2018, ApJ, 862, 142

Khaire, V., Srianand, R., et al. 2016, MNRAS, 457, 4051

Kimm, T., Katz, H., Haehnelt, M. G., et al. 2017, MNRAS, 466, 4826

Koekemoer, A. M., Faber, S. M., Ferguson, H. C., et al. 2011, ApJS, 197, 36

Kurk, J., Cimatti, A., Daddi, E., et al. 2013, A&A, 549, A63

Leitet, E., Bergvall, N., Hayes, M., et al. 2013, A&A, 553, A106

Leitherer, C., Ferguson, H. C., Heckman, T. M., & Lowenthal, J. D. 1995, ApJ, 454, 19L

Livermore, R. C., Finkelstein, S. L., & Lotz, J. M. 2017, ApJ, 835, 113

Luo, B., Brandt, W. N., Xue, Y. Q., et al. 2017, ApJS, 228, 2

Madau, P. 1995, ApJ, 441, 18

Madau, P. & Haardt, F. 2015, ApJ, 813, L8

Marchi, F., Pentericci, L., Guaita, L., et al. 2018, A&A, 614, A11

Matthee, J., Sobral, D., Best, P., et al. 2017, MNRAS, 465, 3637

Micheva, G., Iwata, I., & Inoue, A. K. 2017, MNRAS, 465, 302

Mitra, S., Ferrara, A., & Choudhury, T. R. 2013, MNRAS, 428, L1

Momcheva, I. G., Brammer, G. B., van Dokkum, P. G., et al. 2016, ApJS, 225, 27

Morris, A. M., Kocevski, D. D., Trump, J. R., et al. 2015, AJ, 149, 178

Mostardi, R. E., Shapley, A. E., et al. 2015, ApJ, 810, 107

Naidu, R. P., Oesch, P. A., Reddy, N., et al. 2017, ApJ, 847, 12

Naidu, R. P., Forrest, B., Oesch, P. A., et al. 2018, MNRAS, 478, 791

Nakajima, K., & Ouchi, M. 2014, MNRAS, 442, 900

Nestor, D. B., Shapley, A. E., Kornei, K. A., et al. 2013, ApJ, 765, 47

Oesch, P. A., Montes, M., Reddy, N., et al. 2018, ApJS, 237, 12

Ouchi, M., Mobasher, B., Shimasaku, K., et al. 2009, ApJ, 706, 1136

Pentericci, L., McLure, R. J., Garilli, B., et al. 2018, A&A, 616, 174

Popesso, P., Dickinson, M., Nonino, M., et al. 2009, A&A, 494, 443

Price, L. C., Trac, H., & Cen, R. 2016, arXiv:1605.03970

Rafelski, M., Teplitz, H. I., Gardner, J. P., et al. 2015, AJ, 150, 31

Reddy, N. A., Steidel, C. C., Pettini, M., et al. 2016b, ApJ, 828, 108

Riccoti, M., & Shull, J. M. 2000, ApJ, 542, 548

Rivera-Thorsen, T. E., Dahle, H., Chisholm, J., et al. 2019, Science, 366, 738

Robertson, B. E., Ellis, R. S., Dunlop, J. S., McLure, R. J., & Stark, D. P. 2010, Nature, 468, 49

Robertson, B. E., Ellis, R. S., Furlanetto, S. R., & Dunlop, J. S. 2015, ApJ, 802, L19

Rutkowski, M. J., Scarlata, C., Haardt, F., et al. 2016, ApJ, 819, 81

Rutkowski, M. J., Scarlata, C., Henry, A., et al. 2017, ApJ, 841, 27

Saha, K., Tandon, S. N., Simmonds, C., et al. 2020, Nature Astronomy, 193

Shapley, A. E., Steidel, C. C., Pettini, M., et al. 2006, ApJ, 651, 688

Shapley, A. E., Steidel, C. C., Strom, A. L., et al. 2016, ApJ, 826, L24

Shin, S., Im, M., Kim, Y., et al. 2020, ApJ, 893, 45

Siana, B., Teplitz, H. I., Ferguson, H. C., et al. 2010, ApJ, 723, 241

Siana, B., Shapley, A. E., Kulas, K. R., et al. 2015, ApJ, 804, 17

Smith, B. M., Windhorst, R. A., Jansen, R. A., et al. 2018, ApJ, 853, 191

Smith, B. M., Windhorst, R. A., Cohen, S., et al. 2020, ApJ, 897, 41

Songaila, A., 2004, AJ, 127, 2598

Songaila, A., & Cowie, L. L. 2010, ApJ, 721, 1448

Steidel., C. C., Pettini, M., & Adelberger, K. L. 2001, ApJ, 546, 665

Steidel, C. C., Bogosavlevic, M., Shapley, A. E., et al. 2018, ApJ, 869, 123

Straatman, C. M. S., Spitler, L. R., Quadri, R. F., et al. 2016, ApJ, 830, 51

Tang, M., Stark, D. P., Chevallard, J., & Charlot, S. 2019, MNRAS, 489, 2572

Teplitz, H. I., Rafelski, M., Kurczynski, P., et al. 2013, AJ, 146, 159

Urrutia, T., Wisotzki, L., Kerutt, J., et al. 2019, A&A, 624, A141

van der Velden, E. 2020, JOSS, 5, 2004.

Vanzella, E., Siana, B., Cristiani, S., & Nonino, M. 2010, MNRAS, 404, 1672

Vanzella, E., Giavalisco, M., Inoue, A. K., et al. 2010, ApJ, 725, 1011

Vanzella, E., Nonino, M., Cristiani, S., et al. 2012, MNRAS, 424, 54

Vanzella, E., Guo, Y., Giavalisco, M., et al. 2012, ApJ, 751, 70

Vanzella, E., Nonino, M., Cupani, G., et al. 2018, MNRAS, 476, 15

Vanzella, E., Caminha, G. B., Calura, F., et al. 2020, MNRAS, 491, 1093

Verhamme, A., Orlitová, I., Schaerer, D., et al. 2017, A&A, 597, 13

Windhorst, R. A., Cohen, S. H., Hathi, N. P., et al. 2011, ApJS, 193, 27

Xue, Y. Q., Luo, B., Brandt, W. N., et al. 2016, ApJS, 224, 15

## Chapter 4

# Introduction to the (Sub)-Millimeter High-Redshift Universe

## 4.1 Phenomenology of Submillimeter Galaxies

Since the launch of the COBE satellite in the 1990s, astronomers have determined that the universe shines as brightly in the far-infrared (FIR) as it does in the UV and optical (Puget et al. 1996; Fixsen et al. 1998; Dole et al. 2006; Cowley et al. 2019). In the decades since, many studies (beginning with the first 850  $\mu$ m observations with the Submillimeter Common-User Bolometer Array (SCUBA) on the 15 m James Clerk Maxwell Telescope (JCMT)) have shown that the vast majority of this cosmic infrared background can be attributed to resolved sources now referred to as submillimeter (submm) galaxies or SMGs. (See, e.g., Smail et al. 1997; Barger et al. 1998; Hughes et al. 1998, and Eales et al. 1999 for some of the first reports on SMGs, and Chen et al. 2013 and Odegard et al. 2019 and references therein for in-depth discussions relating SMG number counts to the cosmic infrared background).

As the name may imply, the bolometric luminosity of SMGs is dominated by emission

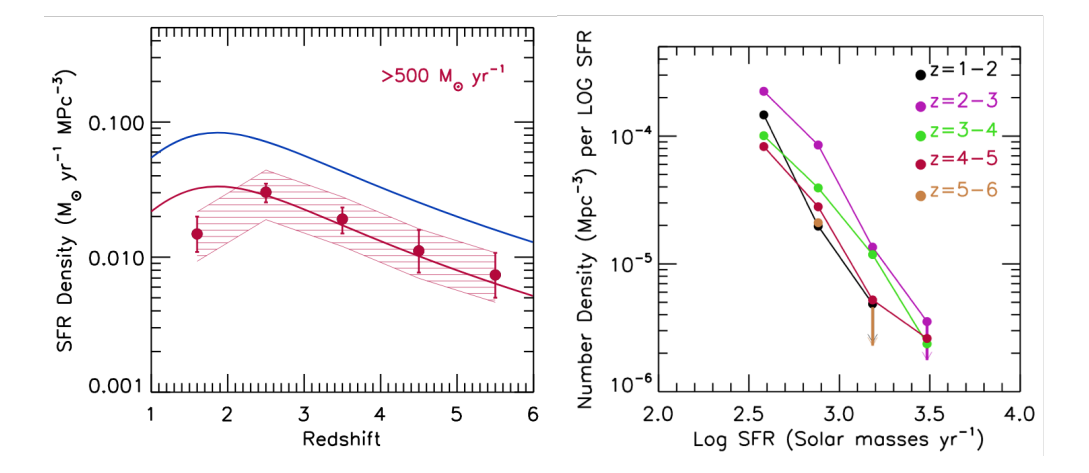


Figure 4.1 : Left: The star formation rate density per comoving volume for SCUBA-2 SMGs with SFR >  $500M_{\odot}$  yr<sup>-1</sup>. The data are binned into redshift intervals  $\Delta z = 1$  wide, with the 68% confidence range shown as the hatched region. The blue curve shows the total (UV+IR) SFR density as a function of redshift from Madau & Dickinson (2014) after conversion to a Kroupa IMF; the red curve shows the same, multiplied by 0.4 to match the amplitude of the data points. Right: Number of sources per log(SFR) bin per comoving volume, split by redshift. Although the normalization is highest at  $z \sim 2-3$  (magenta points), these data suggest a roughly constant proportion of ultra-luminous SMGs to more moderate ones out to at least  $z \sim 5$ . Figure reproduced from Cowie et al. (2017).

at FIR through millimeter wavelengths. Like their low-redshift cousins, the ultra- and hyperluminous infrared galaxies (ULIRGs and HyLIRGS), SMGs are heavily enshrouded in dust (with optical extinctions  $A_V \sim 2-5$ ), which obscures and absorbs much of the ultraviolet flux in these galaxies and re-radiates it into the FIR. It is thought that this dust emission is powered mostly by massive, UV-bright stars, though some SMGs may also host an obscured AGN, which can contribute to the UV-FIR energy balance (e.g., Haziminaoglou et al. 2010; Gall et al. 2011; Wang et al. 2013a; Barger et al. 2019).

The inferred FIR luminosities imply prodigious rates of star formation in SMGs, often in excess of 500  $M_{\odot}$  yr<sup>-1</sup> and as high as  $\sim 6000 M_{\odot}$  yr<sup>-1</sup>, assuming a Salpeter (1955) initial mass function (Barger et al. 2014). As such, they are responsible for a large fraction of the cosmic star formation rate density (SFRD) at z > 2, where they are most common (Chapman et al. 2005; Simpson et al. 2014; Neri et al. 2020). Depending on the sample and

redshift range, literature reports suggest that between  $\sim 20$  and 50% of the SFRD at z > 2 is powered by SMGs (e.g., Le Floc'h et al. 2005; Barger et al. 2014; Madau & Dickinson 2014; Cowie et al. 2017; Dudzevičiūtė et al. 2020); see also the left panel of Figure 4.1, which has been reproduced from Cowie et al. (2017).

Finally, SMGs are thought to be likely progenitors of modern, massive ellipticals and of compact quiescent galaxies at intermediate redshifts, which appear to have built up their stellar masses at early times and over short durations (e.g., Thomas et al. 2010; Carilli & Walter 2013; Simpson et al. 2014; Toft et al. 2014). As sites of intense star formation, merger activity (e.g., Toft et al. 2014), and possible accretion of cold gas (e.g., Tadaki et al. 2018), several lines of evidence point to SMGs also being tracers of massive halos in the high-redshift universe (e.g., Chen et al. 2016; Dudzevičiūtė et al. 2020; Long et al. 2020). This last point motivates the research presented in the next chapter, in which I report the discovery of a new, SMG-rich protocluster of galaxies. A full description of the phenomenology of SMGs is given in Casey et al. (2014).

## 4.2 Observational Utility of Submillimeter Galaxies at High Redshift

While difficult to observe at all but the lowest redshifts at UV and optical wavelengths due to their extremely dusty nature, SMGs are quite easy to observe at (sub)millimeter wavelengths out to very high redshifts due to a peculiarity in the shape of their FIR SEDs. In brief, dust emission in SMGs is well-described by a modified blackbody,  $S \propto (1-e^{-\tau})B_{\nu}$ , where  $B_{\nu}$  is the Planck function. Here, the differential opacity of dust as a function of frequency  $\tau \propto \nu^{\beta}$  (Draine 2006) imposes a steeper-than-normal dependence of source flux on  $\nu$  (hence the moniker of a "modified" blackbody); values of  $\beta$  between 1.5 and 2.5 are typical in studies of ULIRGs and SMGs (e.g., Dunne & Eales 2001). A peak rest-frame

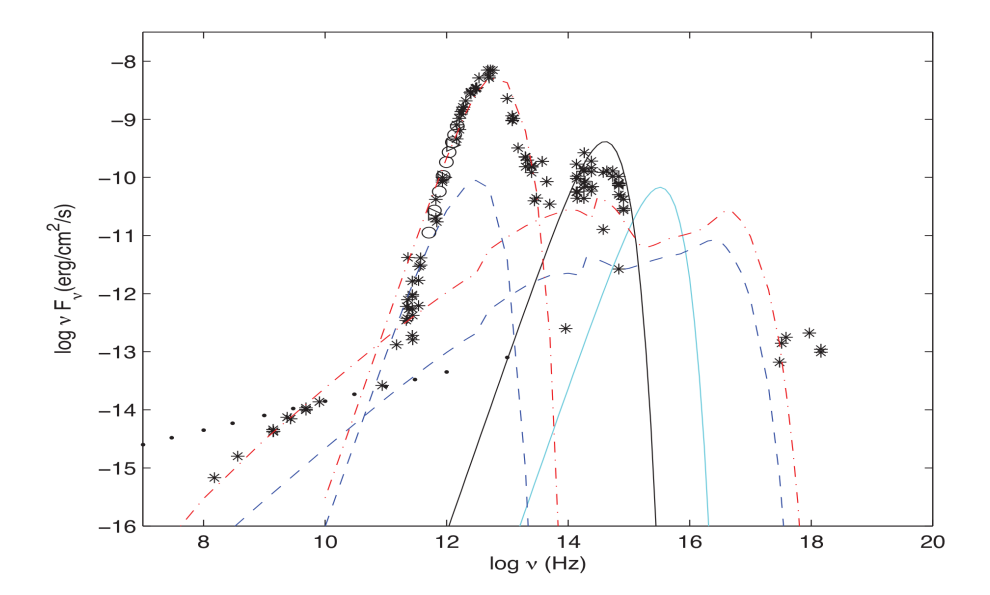


Figure 4.2: An SED of the merging galaxy system Arp220, a ULIRG and prototype for SED modeling of many other dusty starbursts in the literature, reproduced from Contini (2013); see Contini (2013) for references for the plotted multiwavelength flux values. Dust emission (the red, dot-dashed modified blackbody curve) dominates the bolometric light output of the system, outshining the old and young stars, active galactic nuclei, and synchrotron components (black solid, cyan, blue dashed, and black dotted curves, respectively).

wavelength of  $\sim 100~\mu\mathrm{m}$  is typical and frequently assumed, but will vary from galaxy to galaxy as a function of dust temperature. At wavelengths substantially longer than the peak (where a simplification of the Planck law to the Rayleigh-Jeans law is appropriate), the above relation simplifies further to  $S \propto \nu^{\beta+2}$ .

Because (sub)millimeter observational windows effectively "climb" the Rayleigh-Jeans tail of the blackbody as the source redshift increases, the steep dependence of source flux on frequency in this wavelength regime is key to the observability of SMGs out to very high redshifts. As an example, for the 850  $\mu$ m atmospheric window observable by JCMT/SCUBA-2, observations of a ULIRG-like galaxy at z=3 will be sensitive to emission much nearer in wavelength to the redshifted peak of the modified blackbody compared to a ULIRG of the same dust temperature and FIR luminosity at z=0. This can be inferred from the shape of the Arp220 SED shown in Figure 4.2 by comparing flux densities at 345

GHz (z = 0) and 1.4 THz (z = 3).

For an appropriate value of  $\beta$ , this shift in the probed rest-frame wavelength range essentially offsets the dimming effect of the much higher distance to the z=3 galaxy, leading to a roughly constant observed flux density  $S_{850}$ . This is known as the negative K-correction, where flux is added back to an observational window due to the source's SED shape at certain wavelengths. Most other wavelength regimes (optical, NIR, radio) have a spectral slope  $\beta$  that is flat or negative, leading to an additional loss of flux due to the shape of the SED (a positive K-correction). In principle, the very negative K-correction at (sub)millimeter wavelengths means that sufficiently deep observations at  $0.8-3~\mu m$  should be able to detect SMGs out to z=8 or greater -if any exist at such early times.

## 4.3 Challenges of Observing Submillimeter Galaxies

The physical characterization of SMGs is confounded by two factors: difficulty in determining spectroscopic redshifts, and difficulty in determining optical and near-infrared (NIR) counterparts. First, SMGs tend to lie at z > 1.5 (e.g., Chapman et al. 2005), where the brightest optical lines are shifted into the JHK bands or beyond. Coupled with the high dust extinction in these galaxies, optical/NIR spectroscopy of individual SMGs becomes relatively expensive; see, however, the stacking analyses of Swinbank et al. (2004) and Casey et al. (2017).

Second, at millimeter wavelengths, diffraction-limited images from single-dish telescopes suffer from poor resolution – e.g., beam FWHMs of 7.5 and 14" at 450 and 850  $\mu$ m with SCUBA-2 on the JCMT; 19.2" at 870  $\mu$ m with LABOCA on the Atacama Pathfinder Experiment; and 17.6, 23.9, and 35.2" in the 250, 350, and 500  $\mu$ m bands on *Herschel* Space Observatory's Spectral and Photometric Imaging Receiver (SPIRE). Such large beam sizes have several effects on the ability of astronomers to accurately profile SMGs with single-

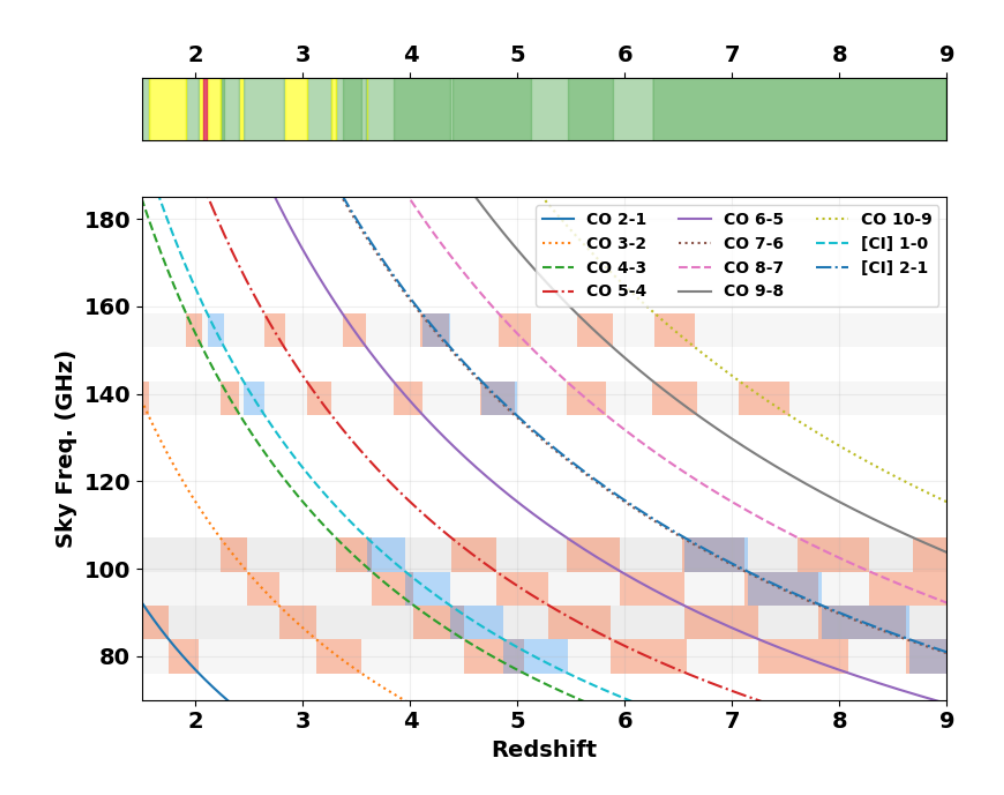


**Figure 4.3**: An illustration of the redshift-determining power of NOEMA across 1.5 < z < 9. Each pair of light or dark grey regions (centered at 87.7, 95.5, and 146.7 GHz) represents the 7.744 GHz-wide upper and lower sidebands of a single spectral tuning. Red and blue patches show redshift intervals where moderate- to high-J CO lines or [CI] lines are observable within the tunings. The upper panel shows the redshift intervals in which zero (red), one (yellow), or two or more (green and dark green) CO and [CI] lines would be detectable using this combination of spectroscopic observations. Above z = 3, this combination of tunings all but ensures an unambiguous redshift determination.

dish data alone. First, beams with FWHM  $\gtrsim 10''$  often encompass many optical and NIR-detected objects, making reliable identification of multiwavelength counterparts inherently difficult. Additionally, single-dish observations have no way of determining whether a given source is a single galaxy or a tight grouping (real or projected) of several weaker submm objects; higher-resolution followup observations routinely show that a substantial fraction ( $\sim 10-40\%$ ) of single-dish sources are actually blends of multiple galaxies (e.g., Barger et al. 2012; Chen et al. 2013; Hodge et al. 2013). Finally, a large angular resolution also imposes a wavelength- and instrument-dependent confusion limit (Condon 1974), which

effectively sets a flux limit below which individual sources cannot be resolved even with arbitrarily long exposures on the same field. This poses a problem for the precise determination of the number density of submm-faint galaxies and hence an accurate census of the fraction of cosmic star formation and background infrared light that is attributable to such sources.

Many of the resolution and confusion issues outlined above can be mitigated with the use of (sub)millimeter-wavelength interferometry, which (depending on the observatory, wavelength, and instrument configuration) can yield spatial resolutions of 1" or better and spectral coverage over wide swathes of frequency space. I show in Figure 4.3 an example of the redshift-identifying power of millimeter spectroscopy with the NOrthern Extended Millimeter Array (NOEMA). Beyond  $z \sim 2$ , many strong transitions from several atomic and molecular species (e.g., [CI], [OI], CO, or  $H_2O$ ; Spilker et al. 2014) are redshifted from the FIR to the millimeter regime, making them readily observable with NOEMA and similar observatories (e.g., ALMA or the Submillimeter Array (SMA)). Careful choice of spectral tunings can all but guarantee a robust redshift identification, without the added challenge of the extincting effects of dust. In the next chapter, I will report redshift measurements for three of the brightest SMGs in the greater GOODS-North field (Giavalisco et al. 2004) using NOEMA. Two of the galaxies lie at  $z \approx 3.14$ , and a brief analysis of the spatial distribution of all galaxies in the GOODS-N at this redshift shows that the SMGs signpost a new and relatively late-forming protocluster of galaxies.

#### References

Barger, A. J., Cowie, L. L., Sanders, D. B., et al. 1998, Nature, 394, 248

Barger, A. J., Wang, W.-H., Cowie, L. L., et al. 2012, ApJ, 761, 89

Barger, A. J., Cowie, L. L., Chen, C.-C., et al. 2014, ApJ, 784, 9

Barger, A. J., Cowie, L. L., Bauer, F. E., & González-López, J. 2019, ApJ, 887, 23

Carilli, C. L. & Walter, F. 2013, ARA&A, 51, 105

Casey C. M., Narayanan D., & Cooray A. 2014, Phys. Rep., 541, 45

Casey, C. M., Cooray, A., Killi, M., et al. 2017, ApJ, 840, 101

Chapman S. C., Blain A. W., Smail I., & Ivison R. J. 2005, ApJ, 622, 772

Chen, C.-C., Cowie, L. L., Barger, A. J., et al. 2013, ApJ, 776, 131

Chen, C.-C., Smail, I., Ivison, R. J., et al. 2016, ApJ, 820, 82

Condon, J. J. 1974, ApJ, 188, 279

Contini, M. 2013, MNRAS, 429, 242

Cowie, L. L., Barger, A. J., Hsu, L.-Y., et al. 2017, ApJ, 837, 139

Cowley, W. I, Lacey, C. G., Baugh, C. M., et al. 2019, MNRAS, 487, 3082

Dole, H., Lagache, G., Puget, J.-L., et al. 2006, A&A, 451, 417

Draine B. T., 2006, ApJ, 636, 1114

Dudzevičiūtė, U., Smail, I., Swinbank, A. M., et al. 2020, MNRAS, 494, 3828

Dunne, L. & Eales, S. A., 2001, MNRAS, 327, 697

Eales, S., Lilly, S., Gear, W., et al. 1999, ApJ, 515, 518

Fixsen, D. J., Dwek, E., Mather, J. C., et al. 1998, ApJ, 508, 123

Gall, C., Hjorth, J., & Andersen, A. C. 2011, A&A Rev., 19, 43

Giavalisco, M., Ferguson, H. C., Koekemoer, A. M., et al. 2004, ApJ, 600, L93

Hatziminaoglou, E., Omont, A., Stevens, J. A., et al. 2010, A&A, 518, 33

Hodge, J. A., Karim, A., Smail, I. et al. 2013, ApJ, 768, 91

Hughes, D. H., Serjeant, S., Dunlop, J., et al. 1998, Nature, 394, 241

Le Floc'h, E., Papovich, C., Dole, H., et al. 2005, ApJ, 632, 169

Long, A. S., Cooray, A., Ma, Jingzhe, et al. 2020, ApJ, 898, 133

Madau, P. & Dickinson, M. 2014, ARA&A, 52, 415

Neri, R., Cox, P., Omont, A., et al. 2020, A&A, 635, A17

Odegard, N., Weiland, J. L., Fixsen, D. J., et al. 2019, ApJ, 887, 40

Puget, J., Abergel, A., Bernard, J., et al. 1996, A&A, 308, L5

Salpeter, E. E. 1955, ApJ, 121, 161

Simpson, J. M., Swinbank, A. M., Smail, I., et al. 2014, ApJ, 788, 125

Smail, I., Ivison, R. J., & Blain, A. W. 1997, ApJ, 490, L5

Spilker, J. S., Marrone, D. P., Aguirre, J. E., et al. 2014, ApJ, 785, 149

Swinbank, A. M., Smail, I., Chapman, S. C., et al. 2004, ApJ, 617, 64

Toft, S., Smolčić, V.; Magnelli, B., et al. 2014, ApJ, 782, 68

Tadaki, K., Iono, D., Yun, M. S., et al. 2018, Nature, 560, 613

Thomas D., Maraston C., Schawinski K., et al. 2010, MNRAS, 404, 1775

Wang, R., Wagg, J., Carilli, C. L., et al. 2013, ApJ, 773, 44

## Chapter 5

## NOEMA Redshift Measurements of Extremely Bright Submillimeter Galaxies Near the GOODS-N

A version of this chapter has been accepted for publication in the Astrophysical Journal Jones, L. H. et al. 2021, ApJ, 916, 46 and is cited as J21b throughout this dissertation.

## Abstract

We report spectroscopic redshift measurements for three bright submillimeter galaxies (SMGs) near the GOODS-N field, each with SCUBA-2 850  $\mu$ m fluxes > 10 mJy, using the Northern Extended Millimeter Array (NOEMA). Our molecular linescan observations of these sources, which occupy an  $\sim$  7 arcmin<sup>2</sup> area outside of the *HST* coverage of the field, reveal that two lie at  $z \sim 3.14$ . In the remaining object, we detect line emission consistent with CO(7–6), [C I], and H<sub>2</sub>O at z = 4.42. The far-infrared spectral energy distributions of these galaxies, constrained by SCUBA-2, NOEMA, and *Herschel*/SPIRE, indicate instantaneous star formation rates  $\sim 4000 \text{ M}_{\odot} \text{ yr}^{-1}$  in the z = 4.42 galaxy and  $\sim 2500 \text{ M}_{\odot} \text{ yr}^{-1}$  in the two  $z \sim 3.14$  galaxies. Based on the sources' CO line luminosities, we estimate  $M_{\rm gas} \sim 10^{11} M_{\odot}$  and find gas depletion timescales of  $\tau_{\rm depl} \sim 50 \text{ Myr}$ , consistent with findings in other high-redshift SMGs. Finally, we show that the two  $z \sim 3.14$  sources, which alone occupy a volume  $\sim 10 \text{ Mpc}^3$ , very likely mark the location of a protocluster of bright SMGs and less dusty optical sources.

## 5.1 Introduction

Submillimeter galaxies (SMGs) are home to some of the most extreme regions of star formation in the Universe. These highly dust-obscured sources, with far-infrared (FIR) luminosities  $L_{\rm IR}$  in excess of  $10^{12}~L_{\odot}$ , have star formation rates (SFRs) of hundreds to thousands of  $\rm M_{\odot}~yr^{-1}$  and typically lie at redshifts z=2-3 (e.g., Chapman et al. 2005; Simpson et al. 2014; Neri et al. 2020), though a significant tail in their redshift distribution has been found out to z>6 (e.g., Daddi et al. 2009a,b; Riechers et al. 2020). SMGs are major contributors to the SFR density of the early Universe, accounting for as much as half of all star formation at z>1 (e.g., Cowie et al. 2017; Dudzevičiūtė et al. 2020). The rapid buildup of stellar mass that results from their prodigious SFRs also suggests that SMGs are likely progenitors of compact quiescent galaxies at moderate redshifts and of massive ellipticals locally (e.g., Simpson et al. 2014; Toft et al. 2014).

In addition to being an important phase in massive galaxy evolution, dusty starbursts may also trace the most massive dark matter halos in the early Universe (e.g., Chen et al. 2016; Dudzevičiūtė et al. 2020; Long et al. 2020). In the last ten years, a growing number of z > 2 overdensities and protoclusters of galaxies have been discovered through an excess of SMGs and luminous active galactic nuclei (AGNs), each containing several (sometimes > 10) such sources (e.g., Chapman et al. 2009; Daddi et al. 2009a,b; Capak et al. 2011; Walter et al. 2012; Casey et al. 2015; Miller et al. 2018; Oteo et al. 2018; Gómez-Guijarro et al. 2019; Hill et al. 2020; Long et al. 2020; Riechers et al. 2020; Zhou et al. 2020).

However, the relatively short duration ( $\lesssim 100$  Myr, e.g., Carilli & Walter 2013) of a dusty starburst phase means that such structures may pose challenges to our understanding of galaxy evolution. Perhaps activation of the SMG phase is somehow correlated over the

volume of a protocluster, though it is unclear how the canonical mechanisms for triggering a starburst in SMGs—gas-rich mergers (e.g., Toft et al. 2014) or the smooth accretion of gas from the surrounding medium (e.g., Tadaki et al. 2018)—could synchronize over large distances and short timescales. Alternatively, the gas depletion timescales  $\tau_{\text{depl}}$  in these environments may be significantly longer than previously thought, up to  $\sim$ 1 Gyr in duration (e.g., Casey 2016, and references therein). However, this conflicts with observations that suggest the most massive ellipticals in low-redshift clusters formed most of their stellar mass in short ( $\lesssim$  1 Gyr) bursts at high redshift (Thomas et al. 2010). Long  $\tau_{\text{depl}}$  would also imply impossibly massive end-product galaxies, if an SMG were to sustain its  $\gtrsim$  500  $M_{\odot}$  yr<sup>-1</sup> SFR for 1 Gyr.

In any case, the existence of SMG-rich structures in the early Universe provides new and interesting constraints on the growth of individual massive galaxies and the assemblage of large-scale structures. Moreover, the diversity of observed properties of distant protoclusters (e.g., Casey 2016, and references therein) illustrates the need for a statistical sample of such structures if we are to make robust inferences about the growth of galaxy clusters and of massive galaxies across cosmic time.

In the first paper of their SUPER GOODS series, Cowie et al. (2017) presented a deep 450  $\mu$ m and 850  $\mu$ m survey of the region around the GOODS-N field using SCUBA-2 on the 15 m James Clerk Maxwell Telescope (JCMT), along with interferometric followup of most of the more luminous SMGs with the Submillimeter Array (SMA). (Note that observations of the field have continued since that published work, and we use the latest images when quoting SCUBA-2 flux densities below.)

Of the six SCUBA-2 sources in the field with 850  $\mu$ m fluxes greater than  $\sim$ 10 mJy, four reside in a small ( $\sim$  7 arcmin<sup>2</sup>) region to the northwest of the field center, just outside the HST/ACS and WFC3 footprints of the GOODS (Giavalisco et al. 2004) and CANDELS

(Grogin et al. 2011; Koekemoer et al. 2011) surveys; see the upper-right panel of Figure 5.1. This includes one of the brightest SCUBA-2 850  $\mu$ m sources in the entire extended GOODS-N with an 850  $\mu$ m flux density of 18.7 mJy; cf. GN20 (Pope et al. 2005) at 16.3 mJy.

The three brightest SMGs in this grouping appear to be single sources at the resolution of the SMA observations, with the fourth only recently observed (M. Rosenthal et al., in preparation). More than being projected neighbors, their similar 20 cm flux densities,  $K_s$  magnitudes, and photometric redshifts  $z_{phot} \sim 3$  (Yang et al. 2014; Hsu et al. 2019) suggest they may also lie at similar redshifts and may even belong to a single, massively star-forming structure. Two more moderately-bright SCUBA-2 sources, each with  $S_{850} > 8$  mJy and  $z_{phot} \sim 3$ , also lie in this region.

In this work, we present the first results of a spectroscopic campaign with the IRAM Northern Extended Millimeter Array (NOEMA) to detect CO line emission towards SMGs in this northwest offshoot of the GOODS-N. From these data, we determined spectroscopic redshifts of the three brightest sources and confirmed that two are at nearly identical redshifts. In Section 5.2, we describe our NOEMA observations and data reduction, along with public multiwavelength imaging for our field. We present the redshifts and observed continuum and line properties of our sources in Section 5.3. In Section 5.4, we discuss the nature of these sources as well as their physical properties derived from our NOEMA data and from optical-through-mm spectral energy distribution (SED) fitting. We also discuss the evidence for these sources signposting a galaxy overdensity, concluding that they very likely belong to a protocluster that is relatively rich in SMGs. Finally, we give a brief summary in Section 5.5. Throughout this work we use a  $\Lambda$ CDM cosmology with  $H_0 = 70.5$  km s<sup>-1</sup>,  $\Omega_{\rm m} = 0.27$ , and  $\Omega_{\Lambda} = 0.73$ .

### 5.2 Data

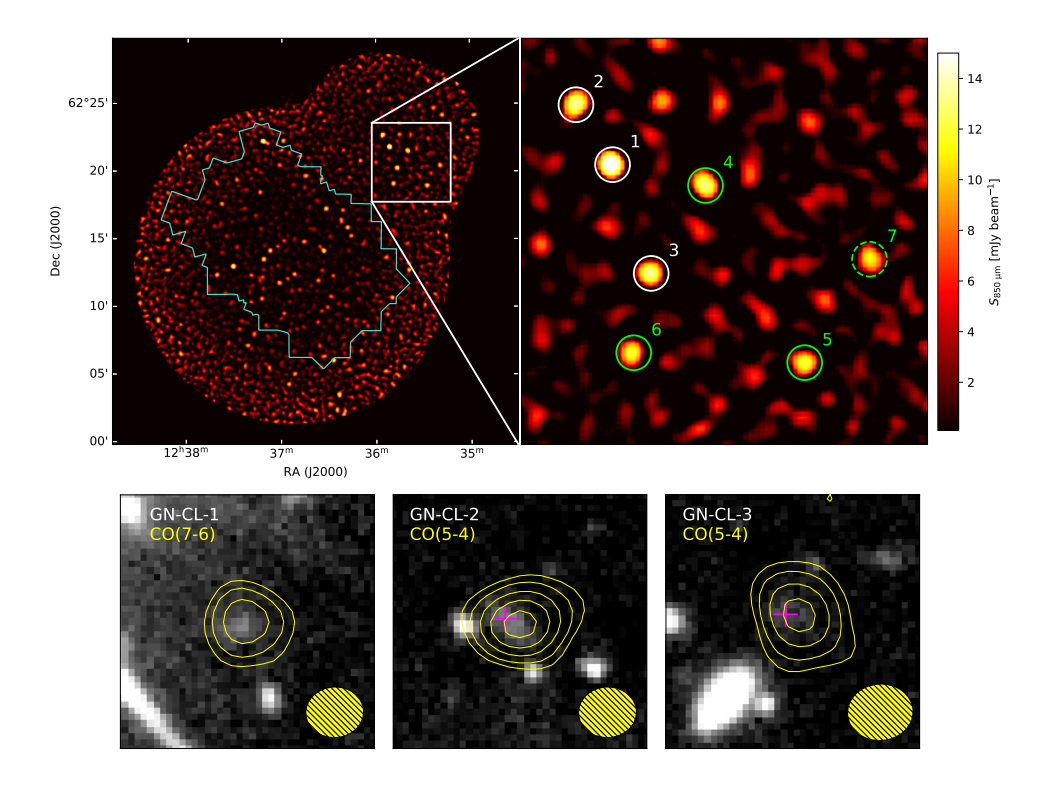


Figure 5.1 : Top left: SCUBA-2 850  $\mu$ m image of the extended GOODS-N. Displayed fluxes include a multiplicative factor of 1.1 to correct for the SCUBA-2 PSF. The blue contour shows the CANDELS HST/WFC3 F160W footprint. Top right: A zoom-in to the portion of the field that contains our target galaxies (marked by the white box in the top left panel). Our 3 target galaxies are circled in solid white. An additional 3 galaxies with  $S_{850} > 8$  mJy, which may also belong to the  $z \sim 3.1$  protocluster, are circled in solid green. Bottom: CFHT/WIRCam  $K_s$ -band images at the positions of GN-CL-1, GN-CL-2, and GN-CL-3. Each panel is 12" on a side. Pink crosshairs mark the coordinates of the nearest  $K_s$ -band counterparts to each source (if any) in the catalog of Hsu et al. (2019). Contours show the 3, 7, 12, 18, and  $25\sigma$  levels of the CO(7–6) emission line in GN-CL-1 and CO(5–4) in GN-CL-2 and GN-CL-3. In the bottom-right corner of each panel, we show the beam profiles for the CO maps as yellow ellipses.

#### 5.2.1 NOEMA Observations

We targeted the three brightest SCUBA-2 sources in the northwest offshoot of the GOODS-N using the NOEMA interferometer in the compact D configuration (project ID W19DG; PI: Jones). We used two spectral tunings each in the *PolyFix* 2 mm and 3 mm bands, which cover the frequency ranges 78.384–109.116 GHz and 131.384–162.116 GHz.

GN-CL-1 and 2 were observed only in the 2 mm band, as 3 mm observations towards these sources had already been carried out in 2019 August; to our knowledge, these data have not yet been published. GN-CL-3 was observed with all four spectral setups. Observations were carried out in track-sharing mode in good weather conditions over the course of 2020 April 10–16, with average atmospheric phase stability of  $\sim 10$ –30% degrees rms and typical precipitable water vapor levels of 1–4 mm. Tracks executed on 2020 April 10 used nine antennas, while all others used ten. In all observations, the quasar 1030+611 was used as the phase and amplitude calibrator. Observations carried out on 2020 April 10 used 0851+202 as the flux calibrator, while all others used LkH $\alpha$ 101. Calibration and imaging of the uv data were carried out in GILDAS. We estimate that the absolute flux calibration is accurate at the  $\sim$ 15% level. Images were produced using natural weighting, with typical synthesized beam sizes of  $7'' \times 4''$  ( $3'' \times 2''.5$ ) at 3 (2) mm (see bottom panels in Figure 5.1).

Identification of lines in each tuning and sideband, as well as separation of line- and continuum-only information, were carried out using an iterative process. First, cleaned spectral cubes were binned to  $\sim$ 75 km s<sup>-1</sup> channel widths to better identify potential emission and absorption features. Strong emission features were identified by eye and then masked with the UV\_FILTER task in GILDAS/MAPPING using a  $\sim$ 800–1000 km s<sup>-1</sup> wide window around the frequency of the line peak. This somewhat aggressive method of line-masking ensures that our continuum measurements remain uncontaminated by strong emission features at the cost of slightly underestimating the continuum flux density. The remaining channels were then collapsed to form our continuum-only images. RMS noise values in a given window were essentially uniform for all sources observed in that window, ranging from 16–19.8  $\mu$ Jy in the 3 mm band and 23.2–30.1  $\mu$ Jy in the 2 mm band. Continuum-subtracted spectral cubes were created with the UV\_BASE task in GILDAS/MAPPING using the same windows as described previously to mask out strong

lines.

### 5.2.2 Multiwavelength Data

Because HST data are not available for our sources, we instead used the compilation of deep ultraviolet (UV), optical, and near-infrared (NIR) photometry of the extended GOODS-N from Hsu et al. (2019) and references therein to constrain the stellar properties of our sources. Specifically, for our SED fits (see Section 5.4.1), we used Subaru/Suprime-Cam BVRIz data from Capak et al. (2004); CFHT/WIRCam  $JHK_s$  data from Wang et al. (2010) and Hsu et al. (2019); and Spitzer/IRAC 3.6  $\mu$ m and 4.5  $\mu$ m data from Ashby et al. (2013). Two of our three sources (GN-CL-2 and 3) have counterparts in the Hsu et al. (2019) catalog within 1" of the SMA 870  $\mu$ m centroid, and we used their photometry directly for these sources. GN-CL-1 is very near a bright (H=7.8) star and thus no nearby optical-NIR counterpart is listed in the Hsu et al. (2019) catalog. Instead, we performed our own aperture photometry on the  $JHK_s$  data from Wang et al. (2010) and Hsu et al. (2019) at the SMA position of GN-CL-1. In each band, we measured fluxes in a 2" diameter aperture and a local median "background" (which largely comes from the saturated foreground star) in a 2.4"-6" diameter annulus, both centered on the SMA position of GN-CL-1. We use the median background values to correct our fluxes for spillover light from the star.

At long wavelengths, we use data from the GOODS-Herschel program of Elbaz et al. (2011) to measure SPIRE 250  $\mu$ m, 350  $\mu$ m, and 500  $\mu$ m fluxes for our sources. Finally, we use the Very Large Array (VLA) 20 cm observations of Morrison et al. (2010) to search for radio counterparts, though the radio fluxes are not included in our SED fits.

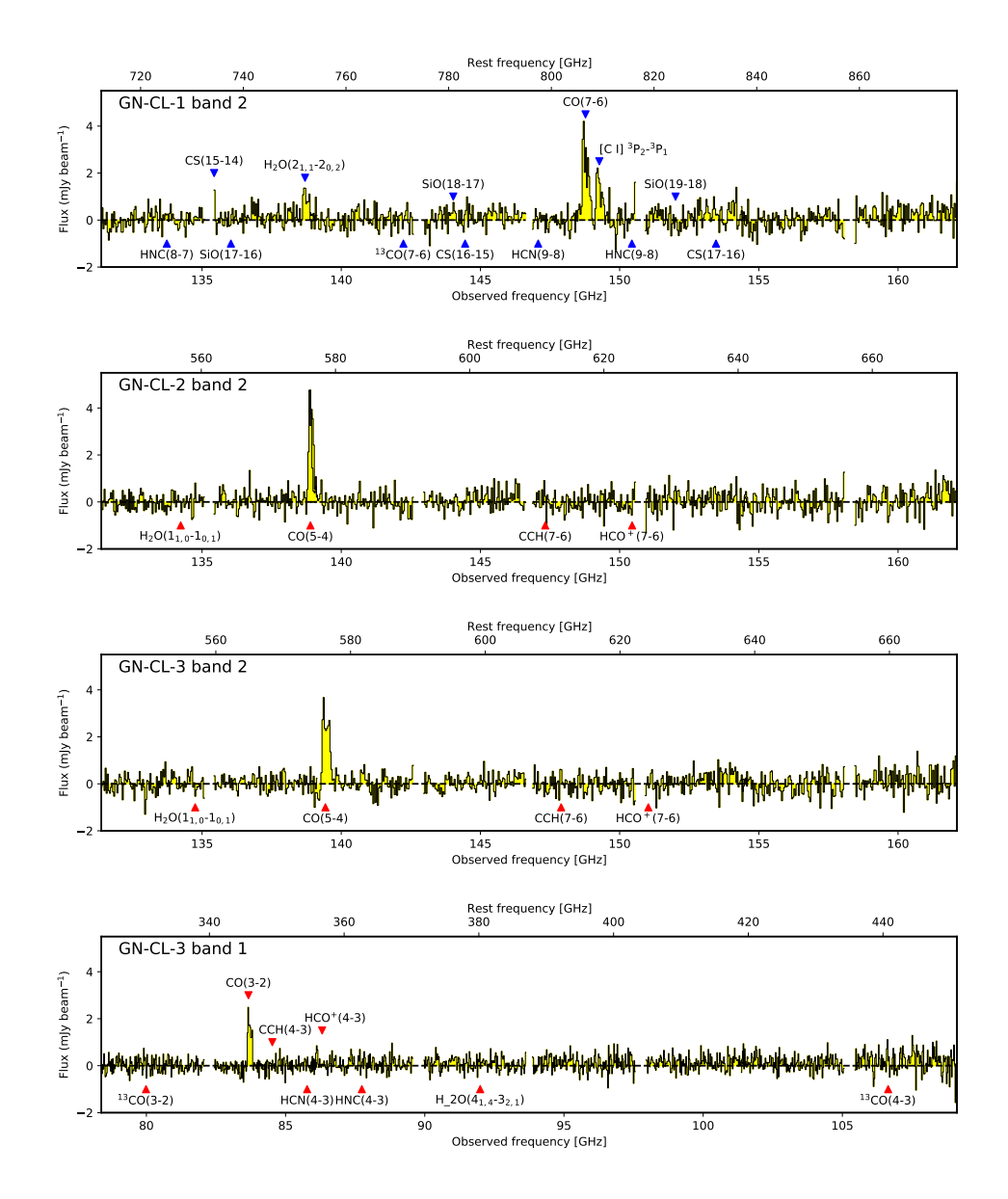


Figure 5.2: Full millimeter spectra of our three bright SCUBA-2 sources. The source name and band are labeled in the top left corner of each panel. Continuum-subtracted spectra were extracted from the spaxel with the brightest continuum emission. The triangles denote the frequencies of common molecular and atomic emission and absorption lines in the spectral ranges of our observations. Given the rms noise in these spectra, we can only securely identify the CO,  $H_2O$ , and  $[C\ I]$  emission lines listed in Table 5.2. However, for completeness, we also label several weaker transitions that are known to exist in these ranges. Red triangles show commonly observed transitions in SMGs from Spilker et al. (2014). Because that work does not extend to the highest rest-frame frequencies at which we observed GN-CL-1, we mark transitions from the NRAO's Splatalogue database as blue triangles on its spectrum.

### 5.3 Results

For GN-CL-1 and GN-CL-2, we extract four continuum flux densities in windows centered at 135.3, 142.8, 150.7, and 158.2 GHz. For GN-CL-3, we extract four at the above frequencies and another four in windows centered at 82.3, 89.8, 97.7, and 105.2 GHz. All of our sources are securely detected in continuum (at the  $\gtrsim 4\sigma$  level) in all sidebands of all tunings in which they were observed, though for brevity, we report only the 158.2 GHz flux densities in Table 5.1, as this sideband is devoid of obvious line emission or absorption in all of our sources and thus provides a clean continuum measurement. As may be expected from their relative 850  $\mu$ m fluxes, the 158.2 GHz flux densities of GN-CL-2 and 3 are similar at around 0.9 mJy, while that of GN-CL-1 is brighter; we give exact values in Table 5.1.

We show the full NOEMA spectra of each of our sources in Figure 5.2, and mark common molecular and atomic transitions in these bands. We do not detect most of the weaker emission features, but GN-CL-1, 2, and 3 all have at least one millimeter emission

Table 5.1: Continuum Properties of NOEMA Targets

Name	R.A. <sup>a</sup>	$\mathrm{Dec.}^a$	$S_{850\mu{\rm m}}{}^{b}$	$S_{158.2\text{GHz}}^{c}$
			[mJy]	[mJy]
GN-CL-1	188.96404	62.36311	$18.7 \pm 0.5$	$2.40\pm0.03$
GN-CL-2	188.98283	62.37750	$11.2 \pm 0.5$	$0.87 \pm 0.03$
GN-CL-3	188.94433	62.33703	$11.5 \pm 0.6$	$0.90 \pm 0.03$

NOTE—<sup>a</sup>Source positions are from the SMA observations of Cowie et al. (2017) (columns 8 and 9 of their Table 5).

 $^b$ The 850  $\mu$ m fluxes are from the latest SCUBA-2 images.

 $^c$ This sideband is devoid of obvious spectral features in all of our sources, providing a clean continuum measurement. The flux uncertainties are from the 2D Gaussian fits to the continuum images and do not include systematic uncertainties, such as from absolute flux calibration, which may be  $\sim 15\%$ .

Table 5.2 . Enter Heritage of Trockitt Intention							
Name	Line	$\nu_{ m obs}$	z	$\nu_0$	$\Delta v_{\mathrm{FWHM}}$	$S_{ m peak}$	
		[GHz]		[GHz]	$[{\rm km~s^{-1}}]$	$[\mathrm{mJy\ beam^{-1}}]$	
GN-CL-1	CO(7-6)	148.76	4.422	806.65	513±49	3.1±0.3	
	$[C I](^3P_2-^3P_1)$	149.24	4.423	809.34	$362 \pm 63$	$2.0 \pm 0.3$	
	$H_2O(2_{11}-2_{02})$	138.72	4.421	752.03	$430 \pm 85$	$1.2 \pm 0.2$	
GN-CL-2	CO(5-4)	138.92	3.148	576.27	$369 \pm 23$	4.3±0.2	
GN-CL-3	CO(5-4)	139.46	3.132	576.27	$500 \pm 41$	$3.0 \pm 0.2$	
	CO(3-2)	83.71	3.131	345.80	$459 \pm 40$	$2.0 \pm 0.2$	

Table 5.2: Line Properties of NOEMA Targets

line detected at  $>5\sigma$ . We show the spectra from the spaxel with the brightest line emission in Figure 5.3. Below we discuss the continuum flux densities, line properties, and redshifts of the sources individually.

GN-CL-1: This source is extremely well-detected in continuum, with flux densities rising from 1.3 ± 0.03 mJy (S/N ~43) in the 135.3 GHz window to 2.4±0.03 mJy (S/N ~80) in the 158.2 GHz window. We detect two strong emission features towards this source at 148.762 and 149.243 GHz and a weaker emission feature at 138.721 GHz, consistent with the frequency ratios of CO(7–6), [C I]( $^3P_2-^3P_1$ ), and H<sub>2</sub>O(2<sub>11</sub>-2<sub>02</sub>) at  $z \approx 4.42$ . We fit the CO(7–6) and [C I]( $^3P_2-^3P_1$ ) lines simultaneously with two Gaussians, without fixing their line ratios, widths, or frequencies relative to one another, and we fit a single Gaussian to the H<sub>2</sub>O feature. The three lines have peak flux densities of 3.1±0.3, 2.0±0.3, and 1.2±0.2 mJy beam<sup>-1</sup> for CO(7–6), [C I]( $^3P_2-^3P_1$ ), and H<sub>2</sub>O(2<sub>11</sub>-2<sub>02</sub>), respectively, with line widths ranging from ~360 to 510 km s<sup>-1</sup>. As we discuss below, this redshift identification shows that GN-CL-1 is not physically associated with either of the remaining two sources.

<u>GN-CL-2</u>: The second brightest SCUBA-2 source in our sample has NOEMA continuum flux densities ranging from  $0.41\pm0.02$  mJy in the 135.3 GHz window to  $0.87\pm0.03$  mJy in the 158.2 GHz window. We detect a single strong emission line towards GN-CL-2 at 138.917 GHz, with a peak flux density of  $4.3\pm0.2$  mJy beam<sup>-1</sup> and a FWHM

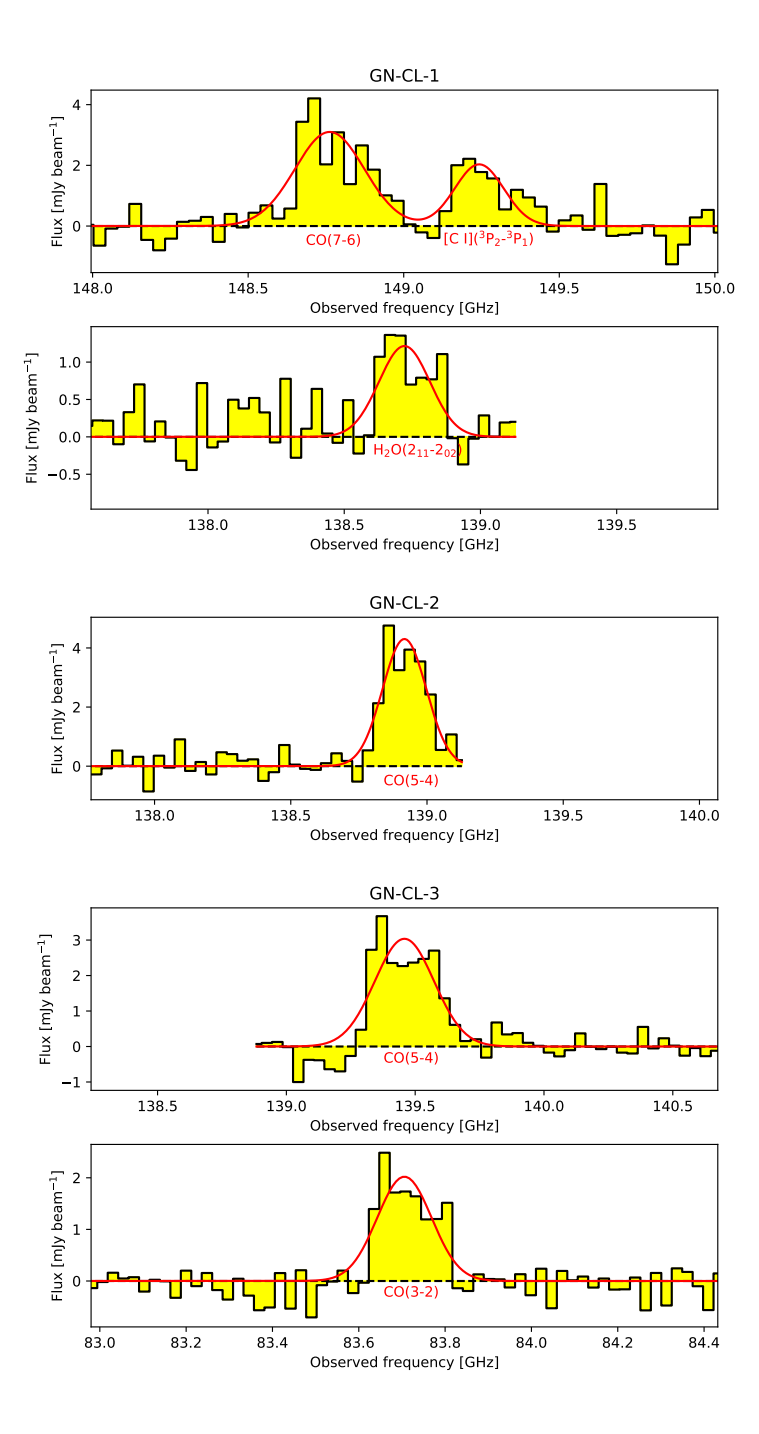
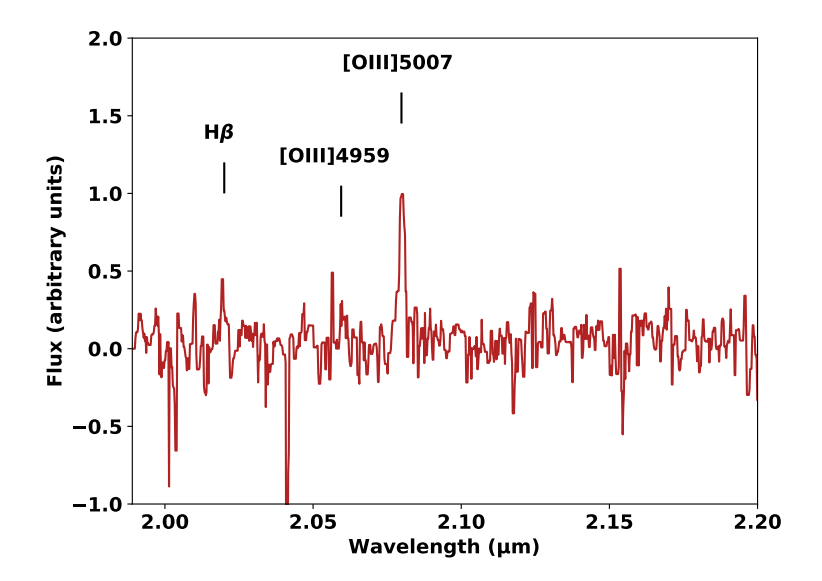


Figure 5.3: Continuum-subtracted CO or  $H_2O$  emission from our three bright SCUBA-2 sources, zoomed in from the full spectra shown in Figure 5.2. Spectra are extracted from the spaxel with the brightest continuum emission. Red lines show Gaussian fits to the data, with the transition labeled in red below the line. The fitted peak flux densities, FHWM velocities, and peak frequencies are listed in Table 5.2.



**Figure 5.4**: Portion of the Keck/MOSFIRE K-band spectrum of optical source 77630 in the catalog of Hsu et al. (2019), the most likely optical-NIR counterpart to GN-CL-2. The data have been median filtered using a window that is 5 wavelength bins wide. We mark the observed positions of the redshifted [OIII] doublet and H $\beta$  at z=3.15.

of  $\approx 370 \text{ km s}^{-1}$ . For this redshift range, based on the most common millimeter transitions in high-redshift SMGs (e.g., Spilker et al. 2014), a line of this strength is most likely to be CO with  $J_{\rm up} = 4$ , 5, 6, or 7 at z = 2.32, 3.15, 3.98, or 4.81, respectively, [C I](1–0) at z = 2.54, or  $H_2O(2_{11}-2_{02})$  at z = 4.41.

Our near-continuous coverage from 131.4–162.1 GHz allows us to rule out most of these redshift identifications by the non-detection of other strong lines at the expected frequencies. If the feature at 138.917 GHz were CO(4–3) at z=2.32, for example, we would expect to detect [CI](1–0) at  $\nu_{\rm obs}\approx 148.2$  GHz, but no significant line emission is seen there. Redshifts of z=3.98, 4.41, and 4.81 are similarly ruled out by the absence of strong ( $\gtrsim 1$  mJy beam<sup>-1</sup>) H<sub>2</sub>O(2<sub>11</sub> – 2<sub>02</sub>), CO(7–6), and [CI]( $^3$ P<sub>2</sub>– $^3$ P<sub>1</sub>) emission at their respective expected frequencies.

This leaves CO(5-4) at z=3.15 and [CI](1-0) at z=2.54 as the only viable redshift identifications from the NOEMA data alone. Follow-up Keck/MOSFIRE K-band

spectroscopy from M. Rosenthal et al., in preparation, of this source's nearest optical-NIR counterpart (source 77630 in Hsu et al. 2019, with K = 22.7 and a separation of 0″.709 from the SMA position of GN-CL-2) finds a redshift of z = 3.15 based on the [OIII] doublet and H $\beta$  (see Figure 5.4). This confirms the higher redshift identification.

GN-CL-3: GN-CL-3 was the only source we observed in both the 2 mm and 3 mm bands. The nearest optical-NIR counterpart to this SMG (separation of 0″473 from its SMA position) is source 85384 in Hsu et al. (2019). Its millimeter continuum flux densities rise smoothly from 82.5±16 μJy in the 82.3 GHz window to  $0.9\pm0.03$  mJy in the 158.2 GHz window. We detect strong emission features at 83.706 GHz and 139.458 GHz, consistent with the frequency ratio of CO(3–2) and CO(5–4) at  $z\approx3.13$ . Separate Gaussian fits to each of these lines yield peak flux densities of  $2.0\pm0.2$  and  $3.0\pm0.2$  mJy beam<sup>-1</sup>, respectively, with FWHM ≈ 480 km s<sup>-1</sup>. GN-CL-2 and GN-CL-3 are therefore confirmed to lie a mere  $\Delta z \sim 0.02$  apart in redshift, with a projected separation of 1.2 Mpc and a 3D separation of 2.7 proper (14.6 comoving) Mpc, if the difference in recession velocities is due only to the Hubble flow. A sphere of diameter equal to the proper distance between these two galaxies would have a volume of, at most, ~10 Mpc<sup>3</sup>. However, as we discuss in the next section, these galaxies very likely belong to a larger overdensity of rare, submillimeter-bright galaxies. If the difference in their redshifts is due to peculiar velocities within a common structure, then the separations quoted above would be overestimates.

Finally, we note that GN-CL-3 appears to have a projected companion about 5" to the southeast. This neighboring source is extremely faint in continuum, with a  $< 2\sigma$  detection in the  $\sim 2$  mm data and completely invisible in the lower-resolution 3 mm data. However, its presence is revealed by a single strong emission feature (peak flux density  $\sim 2.5$  mJy) at 149.3 GHz. No line emission from an SMG at z=3.13 is expected at this frequency, which suggests that the companion is not associated with GN-CL-3. The line emission is

spatially coincident with an optically-bright z = 0.543 radio source (Barger et al. 2014), which suggests this line may be CO(2-1).

## 5.4 Discussion

### 5.4.1 Star Formation Rates, Masses, and Dust Temperatures

The rich photometric data from the rest-frame optical to the radio allow us to constrain the physical properties of these galaxies with SED fitting. We use the Code Investigating GALaxy Emissions (CIGALE, Noll et al. 2009), which calculates SEDs using an energy balance principle, where the energy absorbed by dust in the UV to NIR equals that re-radiated in the MIR to FIR. We use the updated PYTHON version of the code, which has been shown to produce comparable results for high-redshift starbursts to other SED fitting codes (Boquien et al. 2019), to constrain the SFRs, stellar masses, dust masses, and dust temperatures of the three SMGs.

We used Bruzual & Charlot (2003) stellar population libraries with a Chabrier (2003) initial mass function (IMF) for the full range of available metallicities. Stellar spectra are attenuated using a modified Charlot & Fall (2000) dust law with fixed power law indices  $\delta_{\rm ISM} = -0.7$  and  $\delta_{\rm BC} = -1.3$  and a separation age between old and young stellar populations of 10 Myr. We use the dust emission models from Draine et al. (2014), with an input minimum radiation field of  $1.0 \leq U_{\rm min} \leq 50.0^{1}$  and an input mass fraction of  $0.005 \leq \gamma \leq 0.05$  irradiated by  $U > U_{\rm min}$ . We fix the radiation field power law slope  $\alpha = 2.0$ , and we fit for polycyclic aromatic hydrocarbon (PAH) mass fractions  $0.47\% \leq q_{\rm PAH} \leq 3.90\%$ . The mean intensity  $\langle U \rangle$  is used to derive a characteristic dust temperature,  $T_{\rm d,char} = 18 \text{ K} \times \langle U \rangle^{1/6}$  (Draine et al. 2014), which we report in Table 5.3.

 $<sup>^{1}</sup>U$  has units of 1 Habing =  $1.6 \times 10^{-3}$  erg cm<sup>-2</sup> s<sup>-1</sup>

	GN-CL-1	GN-CL-2	GN-CL-3				
$\rm SFR^a \ [M_{\odot} \ yr^{-1}]$	$3900 \pm 580$	$2530 \pm 130$	$2990 \pm 770$				
$SFR_{100}^{b} [M_{\odot} yr^{-1}]$	$1070 \pm 300$	$630 \pm 30$	$390 \pm 140$				
$M_{\star} \ [10^{10} \ {\rm M}_{\odot}]$	$10.7 \pm 3.1$	$5.8 \pm 0.3$	$4.5\pm1.2$				
$sSFR [Gyr^{-1}]$	$37 \pm 12$	$44 \pm 3$	$67 \pm 25$				
$M_{\rm d} \ [10^9 \ {\rm M}_{\odot}]$	$4.5 \pm 0.4$	$2.2 \pm 0.2$	$2.0 \pm 0.1$				
$T_{\rm d,char}$ [K]	$33.4 \pm 0.8$	$34.9 \pm 0.5$	$34.8 \pm 0.6$				
$M_{\rm gas} \ [10^{11} \ {\rm M}_{\odot}]$	$2.0 \pm 0.5$	$1.3 \pm 0.2$	$1.2 \pm 0.2^{c}$				
$\tau_{\rm depl} \; [{ m Myr}]$	$52 \pm 15$	$51 \pm 9$	$41 \pm 13^{c}$				
$M_{ m gas}/M_{ m d}$	$45 \pm 12$	$59 \pm 11$	$61 \pm 12^{c}$				

Table 5.3: Derived Properties of Candidate Protocluster Members

Note—<sup>a</sup>Instantaneous SFR from CIGALE. This row is used to calculate sSFR and  $\tau_{\text{depl}}$ .

<sup>b</sup>100 Myr-averaged SFR from CIGALE.

<sup>c</sup>GN-CL-3 values use  $M_{\rm gas}$  from CO(5–4), but these are consistent within error with values from CO(3–2) (see Section 5.4.2).

The properties estimated by CIGALE, especially the SFR, are strongly dependent on the input star formation history (SFH). Given these galaxies have FIR fluxes indicative of ongoing starbursts, we model the SFH as having formed 50-99% of stars by mass in a short, ongoing, flat burst of age  $\leq 100$  Myr, and the remainder of stars in an exponentially declining SFH of age 0.25-1.5 Gyr, with e-folding time 250 Myr  $\leq \tau_{\text{main}} \leq 6$  Gyr. CIGALE returns a maximum likelihood instantaneous SFR for each galaxy, as well as SFRs averaged over the preivous 10 and 100 Myr. Different methods of SFR estimation in the literature report either averaged or instantaneous SFRs, so we report both the instantaneous and 100 Myr-averaged SFR for each galaxy in Table 5.3. We use the instantaneous SFRs to compute gas depletion times (see Section 5.4.2). The 100 Myr-averaged SFR is appropriate for comparisons with SFRs output from codes such as MAGPHYS (da Cunha et al. 2015) and works that use it (e.g. Dudzevičiūtė et al. 2020).

We ran CIGALE on FIR to millimeter photometry from Herschel/SPIRE, SCUBA-2,

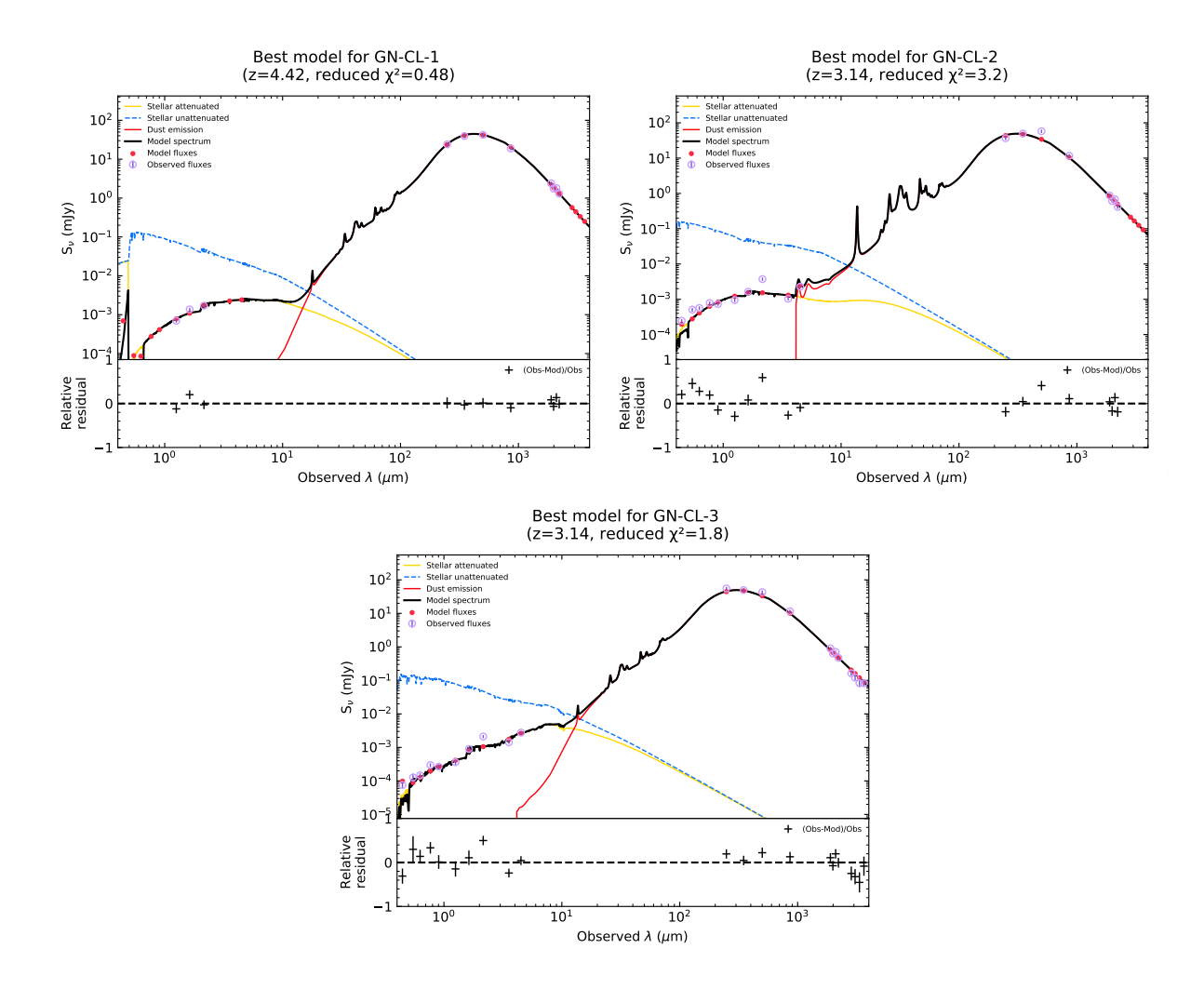


**Figure 5.5**: Best-fit SEDs from CIGALE for each SMG. The black curve shows the total SED, while the red and yellow curves show the relative contributions to the SED of the dust and the attenuated stellar emission, respectively. The purple and red dots show the measured and fit fluxes, respectively.

and NOEMA, along with observed-frame optical to NIR photometry from Hsu et al. (2019) (for GN-CL-2 and 3) or our own JHKs aperture photometry (for GN-CL-1). In addition to the cataloged measurement uncertainties, we included a 10% systematic uncertainty on the absolute photometry/flux calibration in our input flux errors. We fixed the redshifts at the spectroscopic redshift of each source; that is,  $z_{spec} = 4.42$  for GN-CL-1 and  $z_{spec} = 3.14$  for GN-CL-2 and GN-CL-3. We show the best-fit SEDs for the three SMGs in Figure 5.5.

Based on its best-fitting SED, GN-CL-1 has an 8–1000  $\mu$ m luminosity  $L_{\rm IR} \approx$ 

 $1.1 \times 10^{13} \ \mathrm{L}_{\odot}$ , making it a high-redshift hyper-luminous infrared galaxy (HyLIRG). Its instantaneous SFR =  $3900\pm580 \ \mathrm{M}_{\odot} \ \mathrm{yr}^{-1}$  is one of the largest in the field. With  $\sim 10^{11} \ \mathrm{M}_{\odot}$  of stars already in place by z=4.42, this source is the likely progenitor of a massive elliptical at  $z\approx 0$ . GN-CL-2 and GN-CL-3 are also massive star-forming galaxies, with 8–1000  $\mu \mathrm{m}$  luminosity  $L_{\mathrm{IR}}\approx 5\times 10^{12} \ \mathrm{L}_{\odot}$ , comparable to nearby ultraluminous infrared galaxies, and instantaneous SFR  $\approx 2500 \ \mathrm{M}_{\odot} \ \mathrm{yr}^{-1}$ . The similarities between GN-CL-2 and GN-CL-3, as well as the difference in their values compared with GN-CL-1, are consistent with rough expectations from the 850  $\mu \mathrm{m}$  flux densities.

#### 5.4.2 Gas Mass and Depletion Timescale

Molecular hydrogen's low emissivity makes it hard to detect even in nearby galaxies, so the luminosity of the CO(1–0) emission line is often used as a proxy for the mass of molecular hydrogen,  $M_{\rm H_2}$ . We follow the methodology of Bothwell et al. (2013) to convert our higher J CO transitions to CO(1–0), and subsequently into a molecular gas mass for each galaxy,  $M_{\rm gas}$ .

We compute the line luminosity  $L'_{\rm CO}$  using the standard relation from Solomon & Vanden Bout (2005):

$$L'_{\rm CO} = 3.25 \times 10^7 \times S_{\rm CO} \Delta V \nu_{\rm obs}^{-2} D_{\rm L}^2 (1+z)^{-3},$$
 (5.1)

where  $L'_{\rm CO}$  is the line luminosity with units K km s<sup>-1</sup> pc<sup>2</sup>,  $S_{\rm CO}\Delta V$  is the integrated line luminosity in Jy km s<sup>-1</sup>,  $\nu_{\rm obs}$  is the observed line frequency in GHz, and  $D_{\rm L}$  is the luminosity distance in Mpc. We take  $S\Delta V$  to be the area underneath the Gaussian fits to each detected CO line and convert our measured luminosities from higher J lines to CO(1–0) using Table 4 of Bothwell et al. (2013). Errors on  $L'_{\rm CO}$  are dominated by errors on  $S\Delta V$  and on the J-conversion factors  $r_{76/10}$ ,  $r_{54/10}$ , and  $r_{32/10}$ . We assume an  $L'_{\rm CO(1-0)}$  to  $M_{\rm H_2}$  conversion factor  $\alpha = 1$  M<sub> $\odot$ </sub>(K km s<sup>-1</sup> pc<sup>2</sup>)<sup>-1</sup>. Finally, we multiply a correction of  $M_{\rm gas} = 1.36 M_{\rm H_2}$ 

to account for the addition of helium.

For a given SFR and  $M_{\rm gas}$ , the depletion timescale is approximately given by

$$\tau_{\rm depl} = \frac{M_{\rm gas}}{\rm SFR}.\tag{5.2}$$

We list the gas masses and depletion times for our galaxies in Table 5.3. For GN-CL-3, which has both CO(5–4) and CO(3–2) detections, we show values for CO(5–4) for consistency with GN-CL-2, but the values derived from both lines are consistent within errors<sup>2</sup>. The depletion times of  $\sim$ 50 Myr are consistent with values for other high-redshift SMGs based on high- $J_{\rm up}$  CO lines (e.g., Casey 2016). Based on the calculations in Casey (2016), we would not be likely to observe two SMGs in the same structure with such short depletion times, though we note that values of  $\tau_{\rm depl}$  are dependent on the SFR measurement methods used, and, by extension, the assumed SFH, IMF, and conversion factor,  $\alpha$ .

## 5.4.3 (Sub)Millimeter Evidence of a Protocluster

As mentioned previously, the three SMGs we targeted with NOEMA are part of a larger grouping of seven bright SCUBA-2 sources to the northwest of the HST coverage of the GOODS-N. One is confirmed by our NOEMA observations to lie at high redshift (z=4.42), while another (source 7 in Figure 5.1) has a U-band counterpart and  $z_{phot}=1.58$ , making it unlikely to belong to the same  $z\approx 3.14$  halo as GN-CL-2 and GN-CL-3. The remaining three sources (4, 5, and 6 in Figure 5.1) have SCUBA-2 850  $\mu$ m fluxes of 9.8 mJy, 8.6 mJy, and 8.2 mJy, respectively. NOEMA redshift scans of these additional sources, which will determine whether they are part of the same system as GN-CL-2 and GN-CL-3, will be carried out in 2021. In the meantime, we can use the known number counts of bright SMGs to estimate the probability that these sources belong to a

<sup>&</sup>lt;sup>2</sup>Specifically,  $M_{\rm gas} = (12.3 \pm 2.3) \times 10^{10} {\rm M}_{\odot}$  and  $\tau_{\rm depl} = 41 \pm 13 {\rm Myr}$  for CO(5–4), and  $M_{\rm gas} = (12.8 \pm 2.7) \times 10^{10} {\rm M}_{\odot}$  and  $\tau_{\rm depl} = 43 \pm 14 {\rm Myr}$  for CO(3–2).

larger structure or protocluster.

The S2COSMOS survey of Simpson et al. (2019) presents number counts of SCUBA-2 850  $\mu$ m sources in the COSMOS field over 2.6 deg<sup>2</sup>, with a typical  $1\sigma$  noise level of 1.2 mJy beam<sup>-1</sup> in the central region of the field. Their incompleteness-corrected cumulative number counts (their Table 2) suggest that one can expect  $61.9^{+7.2}_{-7.7}$  sources per deg<sup>2</sup>  $(0.017^{+0.002}_{-0.002} \text{ arcmin}^{-2})$  at a flux density  $S_{850} > 7.7$  mJy. However, there are seven  $S_{850} > 8$  mJy galaxies in the northwest offshoot of the GOODS-N that occupy an area only  $\sim 4.6 \times 4.1$  arcmin<sup>2</sup> in size, for a cumulative source density of  $N(S_{850} > 8 \text{ mJy}) = 0.371 \text{ arcmin}^{-2}$ . If we assume that the positions of bright SMGs are completely random on the plane of the sky and uncorrelated in redshift space, then the number counts in Simpson et al. (2019) suggest that we should expect an average of just 0.321 sources with  $S_{850} > 8$  in a given  $4.6 \times 4.1$  arcmin<sup>2</sup> area, a factor of 21.8 lower than what is observed in our field. Even removing sources 1 and 7 (for a total of 5 galaxies across a  $4 \times 4$  arcmin<sup>2</sup> area) yields a projected overdensity 14 times higher than what would be expected if the remaining sources were not part of a single structure.

Alternatively, let us assume that whether or not a bright SMG is seen in a unit area is a Poissonian process so that we can use small number statistics (Gehrels 1986) to determine the raw likelihood of seeing multiple randomly-distributed  $S_{850} > 8$  mJy sources in an 18.9 arcmin<sup>2</sup> box. Specifically, if we treat GN-CL-2 and GN-CL-3 as a single system due to their nearly-identical redshifts, then we may compute the chances of observing 2 < N < 6 projected systems via  $P(N; 0.321) = \frac{\lambda^N e^{-\lambda}}{N!}$ , where  $\lambda = 0.321$  is the mean expected number of sources in a  $4.6 \times 4.1$  arcmin<sup>2</sup> area. As may be expected, the probability of such a projection drops rapidly with increasing N, falling from 3.7% at N = 2 to  $1.1 \times 10^{-4}\%$  at N = 6. For N = 5 (6), only  $\sim 2500$  (160) such projections are expected to be seen across the entire sky.

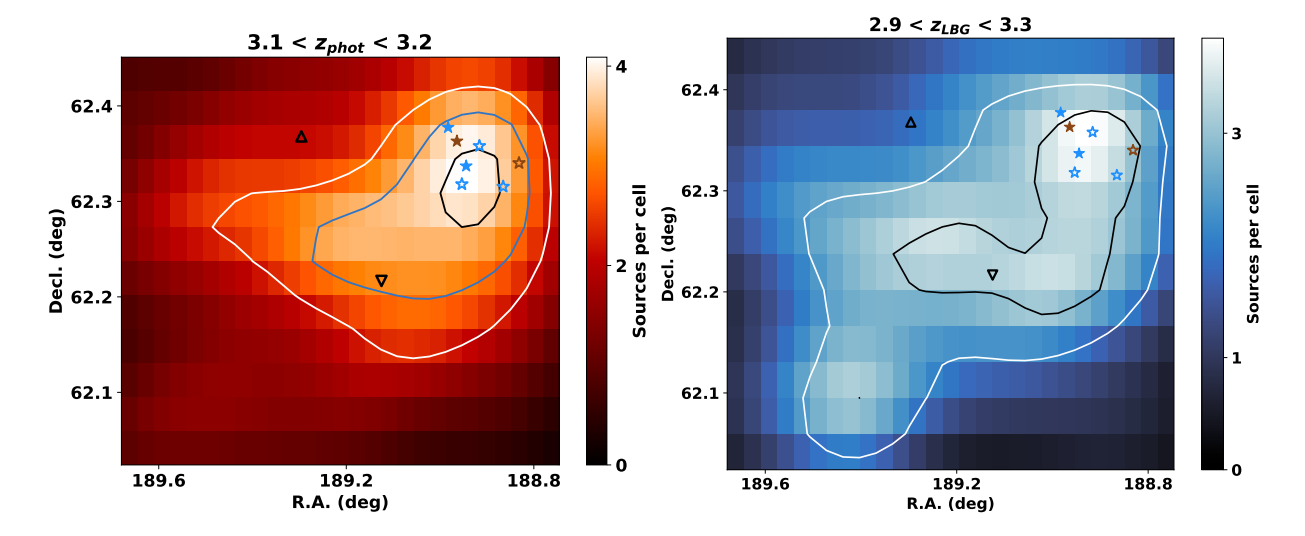


Figure 5.6: Projected 2D density of all sources in the extended GOODS-N with  $3.1 < z_{phot} < 3.2$  in Hsu et al. (2019) (left) and those in the interval  $2.9 < z_{phot} < 3.3$  that meet the LBG criteria of Capak et al. (2004) (right). In both panels, a Gaussian kernel density estimate has been applied, and each cell is  $2 \times 2$  arcmin<sup>2</sup>. Contours on the left (right) panel indicate regions where the source density is  $3\sigma$ ,  $4\sigma$ , and  $5\sigma$  ( $2\sigma$  and  $3\sigma$ ) higher than the mean in the CANDELS portion of the field. Filled stars show the positions of SMGs observed as part of this work (blue if they are spectroscopically confirmed to lie at  $z \sim 3.14$ , and brown otherwise). Blue open stars show the positions of other  $S_{850} > 8$  mJy SMGs in the region that do not yet have spectroscopic confirmation but may belong to the overdensity. The brown open star is an SMG with a bright U-band counterpart and  $z_{phot} = 1.58$ . Upward- and downward-pointing open triangles, respectively, mark the positions of the GN20 overdensity (Pope et al. 2005; Daddi et al. 2009a) and the z = 1.99 SMG-rich protocluster of Chapman et al. (2009).

However, we know from the combination of our NOEMA observations and the UV through radio photometry of Hsu et al. (2019) that sources 1 and 7 are, indeed, a chance projection with one another and with sources 2 and 3. In other words, all three systems are independent "events" such that N is at least 3. If even one of the remaining three bright SMGs is also a chance projection with these systems, then we begin to move into a regime of such extraordinarily low probability that it defies our assumption of independent and physically unassociated systems.

#### 5.4.4 Optical Evidence of a Protocluster

The region we consider in this work is well outside the HST coverage of the GOODS-N. Thus, spectroscopic followup is extremely incomplete, even for relatively bright objects, compared to the GOODS/CANDELS portion of the field. Within a 5' radius of the mean position of all seven bright SMGs, there are 316 (2949) sources with R magnitudes brighter than 22 (25), of which only 3 (8) objects have a published spectroscopic redshift in the multiband catalog of Hsu et al. (2019), with none at z > 2.

In M. Rosenthal et al., in preparation, we will use our Keck/MOSFIRE spectroscopy of optical-NIR sources in the northwest region of the GOODS-N, together with our existing and upcoming NOEMA data, to characterize the  $z \approx 3.14$  protocluster. For now, we use the multiband catalog of Hsu et al. (2019) to see whether evidence of an optical overdensity is present based on photometric redshifts only. We restrict to objects with Kron R magnitudes brighter than 25 and R magnitude errors fainter than 26.75, corresponding to a  $> 5\sigma$  detection. We further restrict to regions where the per-pixel J-band flux uncertainties are less than twice the median rms in the central part of the field. This results in the loss of 139 arcmin<sup>2</sup> of the  $JHK_s$  survey area but also removes the bulk of spurious or extremely noisy sources near the edge of the field. Over the redshift interval  $3.1 < z_{phot} < 3.2$ , we find a mean density of 0.58 galaxies per arcmin<sup>2</sup>. However, when we perform a similar analysis in an area of radius 4' centered on the bright SMG overdensity, we find a mean density of 0.89 galaxies per arcmin<sup>2</sup>. The total number of objects in the overdense region is 45 compared with an expected value of 29.

We next compare the distribution of the number of sources in 1' square cells in the full field with that in an 8' square area centered on the SMGs (64 cells). A one-tailed Mann-Whitney test of these two samples yields a p value of 0.0014, which implies that

they are not drawn from the same distribution and that the optical-NIR overdensity is statistically significant.

For visualization purposes, we show in the top panel of Figure 5.6 a 2D histogram of the source density in this narrow photometric redshift interval. This density map has been "smoothed" using a Gaussian kernel density estimate with  $2' \times 2'$  bins. We note a clear maximum in the density of optical sources that is coincident with the grouping of bright SMGs.

As an additional check, we examine the spatial distribution of candidate Lyman Break Galaxies (LBGs) across the extended GOODS-N in the bottom panel of Figure 5.6. We use the color criteria of Capak et al. (2004) to select LBGs in the redshift interval  $2.9 < z_{phot} < 3.3$ . While the photometric redshift interval is too broad to constrain the number of LBGs that may belong to a single, coherent structure at  $z \approx 3.14$ , we nevertheless note that the maximum density of LBGs is again coincident with the (projected) overdensity of bright SMGs (see the bottom panel of Figure 5.6).

Finally, we note that the  $\sim 0^\circ.07 \times 0^\circ.07$  angular extent of our extremely bright SMG overdensity is intermediate in size compared to other high-redshift, SMG-rich protoclusters in the literature. For example, this structure is quite compact compared to the z=1.99 structure in the GOODS-N (Chapman et al. 2009, 0°.17 × 0°.17), the SSA22 protocluster at z=3.1 (Steidel et al. 1998, 0°.33 × 0°.50), and the z=5.18 HDF850.1 overdensity (Walter et al. 2012, 0°.10 × 0°.13). However, it is more extended than the GN20 overdensity (Pope et al. 2005; Daddi et al. 2009a,b, 0°.01 × 0°.01) and the Distant Red Core (Oteo et al. 2018; Ivison et al. 2020, 0°.02 × 0°.02), both at  $z\sim4$ . We defer a fuller discussion of the total SFR, stellar mass, halo mass, and physical extent to M. Rosenthal et al., in preparation.

## 5.5 Summary

We report the results of a millimeter spectroscopic campaign with NOEMA to measure redshifts for three of the 850  $\mu$ m-brightest SMGs in the extended GOODS-N, which lie in a close (projected) grouping. We determined unambiguous spectroscopic redshifts for two of our three targets using the NOEMA data alone (GN-CL-1 at z=4.42 and GN-CL-3 at z=3.13) and for the remaining target using both NOEMA and Keck/MOSFIRE spectroscopy (GN-CL-2 at z=3.15). With nearly identical redshifts, GN-CL-2 and 3 are likely part of a single system and may signpost an overdensity of galaxies at  $z\approx3.14$ . More importantly, there are three more bright, neighboring SMGs which, based on number counts and simple probability estimates, are extremely likely to belong to the same structure, constituting a protocluster of short-lived SMGs in the high-redshift Universe. Finally, our best-fit SEDs suggest that GN-CL-1, one of the brightest SCUBA-2 850  $\mu$ m sources in the extended GOODS-N field, is an extremely FIR-luminous, high-redshift dusty starburst with  $\sim 10^{11}$  M $_{\odot}$  already formed when the Universe was only 1.4 Gyr old.

We thank the anonymous referee for a useful report that helped us to improve the manuscript. We gratefully acknowledge support for this research from a Wisconsin Space Grant Consortium Graduate and Professional Research Fellowship (L.J.), NASA grant NNX17AF45G (L.L.C.), the William F. Vilas Estate (A.J.B.), and the Kellett Mid-Career Award from the University of Wisconsin-Madison Office of the Vice Chancellor for Research and Graduate Education with funding from the Wisconsin Alumni Research Foundation (A.J.B.).

This work is based on observations carried out under project number W19DG with the IRAM NOEMA Interferometer. IRAM is supported by INSU/CNRS (France), MPG (Germany) and IGN (Spain). L. Jones thanks Vinod Arumugam for many helpful

discussions on the reduction and processing of NOEMA observations.

 $\label{eq:Facilities: Subaru (Suprime-Cam), JCMT (SCUBA-2), SMA, NOEMA, Herschel,} \\ \text{JVLA}$ 

Software: astropy (Astropy Collaboration et al. 2018)

#### A Statement of Work

Here are briefly outlined the contributions of all listed authors for this publication, in order of their listing in the journal article.

- Logan H. Jones: Led data reduction, redshift identification, and submillimeter clustering analysis; primary contributor to the writing of this manuscript.
- Michael J. Rosenthal: Fitted emission lines and SEDs of target sources; significant contributor to the writing of this manuscript.
- Amy J. Barger: Performed statistical test of, and provided brief text on, the optical clustering; suggested tests of the methodology; proofreading and revisions.
- Lennox L. Cowie: Led reduction of Keck/MOSFIRE data that confirmed the redshift of GN-CL-2; suggested tests of the methodology; proofreading and revisions.

#### References

Astropy Collaboration, Price-Whelan, A. M., Sipőcz, B. M., et al. 2018, AJ, 156, 123

Ashby, M. L. N., Willner, S. P., Fazio, G. G., et al. 2013, ApJ, 769, 80

Barger, A. J., Cowie, L. L., Chen, C.-C., et al. 2014, ApJ, 784, 9

Boquien, M., Burgarella, D., Roehlly, Y., et al. 2019, A&A, 622, A103

Bothwell, M. S., Smail, I., Chapman, S. C., et al. 2013, MNRAS, 429, 3047

Bruzual, G. & Charlot, S. 2003, MNRAS, 344, 1000

Capak, P., Cowie, L. L., Hu, E. M., et al. 2004, AJ, 127, 180

Capak, P. L., Riechers, D., Scoville, N. Z., et al. 2011, Nature, 470, 233

Carilli, C. L. & Walter, F. 2013, ARA&A, 51, 105

Casey, C. M., Corray, A., Capak, P. et al. 2015, ApJL, 808, 33

Casey, C. M. 2016, ApJ, 824, 36

Chabrier, G. 2003, PASP, 115, 763

Chapman S. C., Blain A. W., Smail I., & Ivison R. J., 2005, ApJ, 622, 772

Chapman, S. C., Blain, A., Ibata, R., et al. 2009, ApJ, 691, 560

Charlot, S. & Fall, S. M. 2000, ApJ, 539, 718

Chen, C.-C., Smail, I., Ivison, R. J., et al. 2016, ApJ, 820, 82

Cowie, L. L., Barger, A. J., Hsu, L.-Y., et al. 2017, ApJ, 837, 139

da Cunha, E., Walter, F., Smail, I. R., et al. 2015, ApJ, 806, 110.

Daddi, E., Dannerbauer, H., Stern, D., et al. 2009a, ApJL, 694, 1517

Daddi, E., Dannerbauer, H., Krips, M., et al. 2009b, ApJL, 695, 176

Draine, B. T., Aniano, G., Krause, O., et al. 2014, ApJ, 780, 172

Dudzevičiūtė, U., Smail, I., Swinbank, A. M., et al. 2020, MNRAS, 494, 3828

Elbaz, D., Dickinson, M., Hwang, H. S., et al. 2011, A&A, 533, A119

Gehrels, N. 1986, ApJ, 303, 336

Giavalisco, M., Ferguson, H. C., Koekemoer, A. M., et al. 2004, ApJ, 600, L93

Gómez-Guijarro, C., Riechers, D. A., Pavesi, R. et al. 2019, Apj, 872, 117

Grogin, N. A., Kocevski, D. D., Faber, S. M., et al. 2011, ApJS, 197, 35

Hill, R., Chapman, S. C., Scott, D., et al. 2020, MNRAS, 495, 3124

Hsu, L.-T., Lin, L., Dickinson, M., et al. 2019, ApJ, 871, 233

Ivison, R. J., Biggs, A. D., Bremer, M., et al. 2020, MNRAS, 496, 4358

Koekemoer, A. M., Faber, S. M., Ferguson, H. C., et al. 2011, ApJS, 197, 36

Long, A. S., Cooray, A., Ma, Jingzhe, et al. 2020, ApJ, 898, 133

Miller, T. B., Chapman, S. C., Aravena, M., et al. 2018, Nature, 556, 469

Morrison, G. E., Owen, F. N., Dickinson, M., et al. 2010, ApJS, 188, 178

Neri, R., Cox, P., Omont, A., et al. 2020, A&A, 635, A17

Noll, S., Burgarella, D., Giovannoli, E., et al. 2009, A&A, 507, 1793

Oteo I., Ivison, R. J., Dunne, L., et al., 2018, ApJ, 856, 72

Pope, A., Borys, C., Scott, D., et al. 2005, MNRAS, 358, 149

Riechers, D. A., Hodge, J. A., Pavesi, R. et al. 2020, ApJ, 895, 81

Simpson, J. M., Swinbank, A. M., Smail, I., et al. 2014, ApJ, 788, 125

Simpson, J. M., Smail, I., Swinbank, A. M., et al. 2019, ApJ, 880, 43

Solomon, P. M. & Vanden Bout, P. A. 2005, ARA&A, 43, 677

Spilker, J. S., Marrone, D. P., Aguirre, J. E., et al. 2014, ApJ, 785, 149

Steidel, C. C., Adelberger, K. L., Dickinson, M., et al. 1998, ApJ, 492, 428

Toft, S., Smolčić, V.; Magnelli, B. et al. 2014, ApJ, 782, 68

Tadaki, K., Iono, D., Yun, M. S., et al. 2018, Nature, 560, 613

Thomas D., Maraston C., Schawinski K., et al. 2010, MNRAS, 404, 1775

Walter, F., Decarli, R., Carilli, C., et al. 2012, Nature, 486, 233

Wang, W.-H., Cowie, L. L., Barger, A. J., Keenan, R. C., & Ting, H.-C. 2010, ApJS, 187, 251

Yang, G., Xue, Y. Q., Luo, B. et al. 2014, ApJS, 215, 27

Zhou, L., Elbaz, D., Franco, M., et al. 2020, A&A, 642, A155

# Chapter 6

# **Summary and Future Prospects**

Understanding the interplay between star formation, environment, and the enrichment of the interstellar medium with dust and metal-rich gas is fundamental to a modern picture of galaxy evolution. The buildup of enriched gas affects the ionizing luminosity of massive stars, the efficiency with which ionizing photons escape their home galaxy to interact with the IGM, and the ability of gas to cool and form new stars – all relevant to determining when cosmic reionization unfolded and how the first galaxies came to be. Later, as dark matter halos continue to collapse and cosmic star formation intensity increases, the growth of large structures may be signposted by the presence of massive (and massively star-forming) dust-obscured galaxies. As first stated in the abstract of this dissertation, the research presented in this dissertation has aimed to help answer two questions on the formation and evolution of the dustiest galaxies on the one hand and the most dust-free on the other. These are:

1) What are the intermediate- to high-redshift analogs to the sources that reionized the universe at very early times?; and 2) As a function of redshift and/or environment, how common are massively star-forming, dust-obscured galaxies?

## 6.1 Direct and Indirect Searches for Sources of Ionization

In Chapters 2 and 3, I presented the results of two searches for candidate sources of LyC radiation from galaxies in the redshift range z=2.5-3. These works focused primarily on the direct photometric detection of ionizing photons from individual sources. Compared to indirect searches of LyC emitters (via high-ionization nebular lines and other tracers of hard radiation fields), such an approach is relatively uncommon due to a scarcity of sufficiently-deep observations in the appropriate photometric band, a lack of reliable spectroscopic redshifts, or both. These works circumvent both of these issues by synthesizing deep F275W imaging from the Hubble Deep UV Legacy Survey of the GOODS fields (Oesch et al. 2018) with the extremely complete spectroscopic catalogs on those regions. Key findings from these works, and their implications for the future of the field, include the following:

- Of the 11 candidate sources of LyC emission we identified across each of the GOODS fields at z > 2.35, only five have no clear evidence in their optical spectra for contamination by foreground galaxies. Of these, one is an X-ray-bright AGN (discussed below) and four are star-forming galaxies. In J21a, we also note the presence of an additional star-forming LyC candidate in the GOODS-North (which did not meet the more stringent detection criteria we used in J18), for a total of five such sources.
- An averaging analysis of all galaxies with spectroscopic redshifts between 2.35 and 3.05 in the GOODS fields reveals that the total F275W signal in this sample is dominated by the five LyC-emitting candidates mentioned above. This mirrors the results of Fletcher et al. (2019), who found in an independent sample that detections of LyC photons happen either quite strongly in individual sources or not at all, even

in deep stacks.

- After correcting for the opacity of the IGM to LyC photons, the sum of the five star-forming candidates' F275W flux output matches, within errors, the inferred energy density of the extreme-UV background at  $z \sim 2.5$ . This implies that galaxies alone could maintain an ionized IGM at these redshifts, in contrast to some recent measurements which suggest a dominant contribution by AGN. However, we caution that the measured ionizing emissivity of star-forming galaxies may increase with the inclusion of even fainter F275W sources, or decrease with a confirmation of foreground contamination in our candidate LyC emitters (via, perhaps, NIR spectroscopy).
- We confirmed in J18 the existence of a LyC-luminous AGN, which we have labelled GN-UVC-1. It appears to be the only one of its kind in the GOODS fields at z ~ 2.5. However, detailed modeling by Smith et al. (2020) suggests that its accretion properties and UV-through-optical SED are typical of AGN at similar redshifts. This object may provide a unique sandbox in which the astronomy community can thoroughly test models for the production and escape of ionizing photons from AGN near the peak epoch of their activity.

Finally, I want to summarize the state of a separate project that, while not sufficiently complete to present as part of this dissertation, will provide an independent method for searching for analogs to reionization-era galaxies. The basis for this work is the Hawaii EROsita Ecliptic-pole Survey (HEROES; PI G. Hasinger), a large imaging program of the North Ecliptic Pole field (NEP). HEROES consists of  $\sim 40-50~\rm deg^2$  of imaging from Hyper SuprimeCam (HSC) on the 8 m Subaru Telescope on Mauna Kea in the grizY broadbands plus two narrowbands (NBs), centered on the 8160 and 9210 Å atmospheric windows. Additional imaging in the U and J bands from the Canada-France-Hawaii telescope covers

a subset of this area.

One of the primary science drivers of HEROES, especially the inclusion of the NB imaging, was to identify and spectroscopically confirm a relatively large population of candidate ultra-luminous Lyman- $\alpha$  emitters at z=5.7 and 6.6 (Songaila et al. 2018; Taylor et al. 2020, 2021) via a flux density excess in an NB relative to its nearest underlying broadband. Of course, any nebular line that is sufficiently luminous may cause such an excess if the source lies in one of several narrow redshift intervals. The NB filter at 9210 Å, for example, is sensitive to high equivalent-width  $H\alpha$  emission at  $z\approx0.4$ , the O[III]+H $\beta$  complex at  $z\approx0.84-0.89$ , and O[II] at  $z\approx1.47$ . Intermediate-redshift ELGs are the most common sources of contamination for Lyman- $\alpha$  surveys, but provide interesting science cases in their own right. Some such cases include characterization of extremely low-metallicity galaxies, which are excellent analogs to reionization-era galaxies; constraining the existence of a gas-phase metallicity floor, which would encode information about the enrichment of the IGM across time; and the evolution of optical line luminosity functions across redshift space (e.g., Sobral et al. 2015).

I used the HEROES imaging set to select photometric NB-excess galaxy candidates with unusual broadband – narrowband colors, with a slight emphasis on the higher-redshift band (e.g., z' – NB921 > 1; the criteria for the NB816-selected sample is similar). After additional filtering to remove sources whose NB photometry is contaminated by cosmic rays and other artifacts, we are left with a sample of ~10,000 sources with NB921 < 23.5 mag and signal-to-noise ratio > 5 in NB921. I then followed up a subset of bright ( $\lesssim 22$  mag) candidate sources with the multi-object spectrometer Hydra on the 3.5 m WIYN telescope. Sources with unusual broadband colors (e.g., a boost in z' relative to the neighboring i and Y bands) are used to fill out unused fibers in our Hydra configurations. To date, I have obtained spectroscopic redshifts for approximately 300 NB sources in the greater NEP with

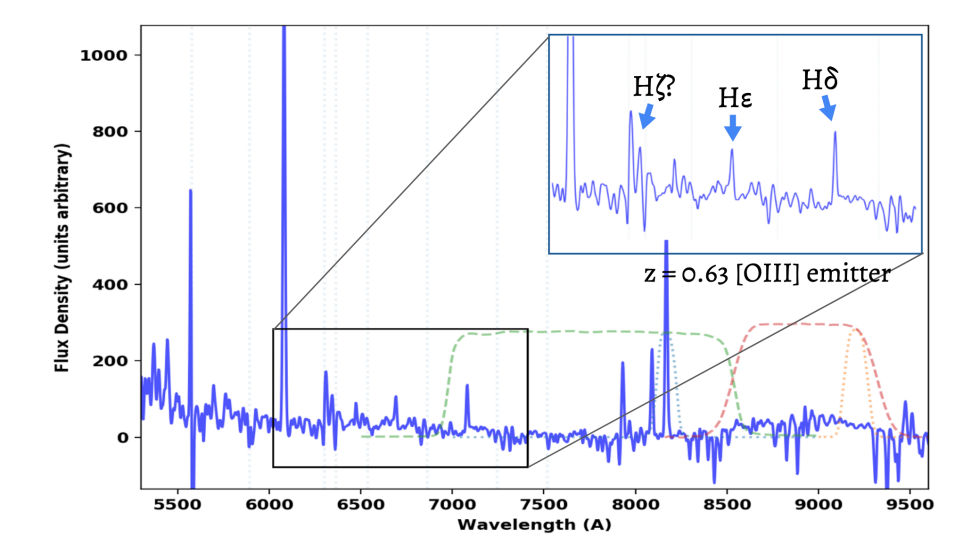


Figure 6.1: A WIYN/Hydra spectrum of an ELG at z = 0.63. The dashed green and red curves show the relative response of the Subaru/HSC i and z' filters, while the dotted blue and orange curves show the response of the NB816 and NB921 filters. The [OIII] doublet and strong Balmer lines out to at least H $\epsilon$  are clearly visible; higher-order Balmer lines are labeled in the inset image. The flux density in the narrowband is dominated by [OIII] $\lambda$ 5007, leading to an apparent excess relative to the much broader i band.

Hydra; these tend to be the brightest NB sources, since poor weather and seeing generally wash out the more numerous faint (NB921 > 21.5) emitters even with our integration times of 2.5 - 3 hours. An example WIYN/Hydra spectrum of a bright NB816 source is shown in Figure 6.1.

A journal article describing the spectroscopic observations and source catalog is in preparation, but additional analysis is needed before publication. Likely next steps include a comparison of the emission line equivalent width as derived from the spectra vs. from the photometry. If the two measurements are in reasonable agreement, this will allow me to estimate line equivalent widths for all NB-excess sources in the HEROES dataset, instead of only those with spectroscopic followup. The above step will increase the usable sample size by at least an order of magnitude, enabling statistical measures of emission line luminosity distributions for each of our subsamples (specifically,  $H\alpha$  emitters at  $z \approx 0.4$ 

and O[III]+H $\beta$  emitters at  $z \approx 0.85$ ). This, in turn, will yield a robust constraint on the star formation rate per unit volume from NB-selected ELGs near the peak of cosmic star formation activity.

# **6.2** A Protocluster of Rare Galaxies at z = 3.14

In Chapter 5, I presented the discovery of a new overdensity of galaxies on the outskirts of the well-studied GOODS-N field. This region is signposted by a (projected) grouping of seven extremely bright ( $S_{850} > 8$  mJy) submillimeter galaxies on scales of  $\sim$ a few arcminutes, with inferred star formation rates in excess of  $1000 \,\mathrm{M}_{\odot} \,\mathrm{yr}^{-1}$  each. Given the uncertainty of how SMGs "turn on" nearly simultaneously in dense environments, and given their nature as sites of very rapid stellar mass growth, an accurate characterization of these sources, their origins, and their ultimate fates demands reliable redshift identifications.

Followup of the three brightest SMGs in the GOODS-N outskirt region with NOEMA confirms that at least two lie at nearly identical redshifts. Meanwhile, a comparison of the spatial distribution of galaxies with photometric redshifts  $z_{phot} \sim 3.14$  near the projected SMG overdensity vs. the central region of the GOODS-N betrays the presence of an overdensity of UV-selected galaxies at the same position. This is confirmed quantitatively through the use of a one-tailed Mann-Whitney test (p = 0.0014) on the density distribution of galaxies in these two regions. All of these lines of evidence point to the presence of a previously unknown protocluster at  $z \approx 3.14$  that is relatively rich in rare galaxies. While we have carried out a few nights of optical-NIR spectroscopy on this region with Keck/LRIS and Keck/MOSFIRE, a more accurate census of UV-selected galaxies that belong to the protocluster will require additional observations. (I note that the redshift of the structure is highly appropriate for Lyman- $\alpha$  emitter searches, making it an attractive and effective option.)

The manuscript on which Chapter 5 is based was primarily a discovery work, with a full characterization of the protocluster and its members deferred to future papers (M. Rosenthal et al., in prep.) after the collection of additional data. However, in the following, I summarize the key findings from this initial analysis and possible next steps for understanding the role of environment on the life and death of an SMG.

- Our NOEMA observations determined unambiguous spectroscopic redshifts for two of the three SMGs we targeted; the remaining source's redshift was later confirmed by NIR spectroscopy with Keck/MOSFIRE. The SMG GN-CL-1, the brightest SCUBA-2 source in the greater GOODS-N field, is revealed to be a HyLIRG-like galaxy at z = 4.42, with an SED-derived instantaneous SFR of ~3900 M<sub>☉</sub> yr<sup>-1</sup>. GN-CL-1 may also be quite massive, with an inferred stellar mass of order 10<sup>11</sup> M<sub>☉</sub> already in place when the universe was a mere 1.4 Gyr old. A more detailed photometric, spectroscopic, and morphological characterization of this object may be fruitful for understanding the extremes of extragalactic star formation and massive galaxy evolution at early times.
- The remaining two SMGs lie at very similar redshifts, with GN-CL-2 at z=3.148 and GN-CL-3 at z=3.132. If their 3D separation is due purely to the Hubble flow, this would imply a separation of 2.7 proper or 14.6 comoving Mpc. The full physical size and kinematics of the overdensity are yet to be determined. However, our MOSFIRE observations of galaxies with  $z_{phot} \sim 3$  in the protocluster field suggests an angular extent of at least  $\sim 0.07 \times 0.07$ , intermediate in size to otherwise similar structures that have been reported in the literature (see the summary and analysis by Casey 2016).
- Additional NOEMA observations of three other  $S_{850} > 8$  mJy SCUBA-2 sources in

the protocluster field have been carried out and reduced since the submission of J21b to the Astrophysical Journal. These data will be published in M. Rosenthal et al., in prep. Two sources have one strong millimeter emission line apiece. While a unique redshift identification cannot be made for either SMG, the observed frequencies of the lines rule out the possibility that either belongs to the  $z\approx 3.14$  structure. The remaining SCUBA-2 source is actually a pair of SMGs, which were only resolvable with the use of interferometry; its nature as a multiple source is confirmed through SMA observations at higher frequencies and comparable spatial resolution. Both components are at the redshift of the protocluster,  $z\sim 3.14$ , but slightly offset from one another in velocity. Their  $\sim 4''$  angular separation implies that they lie a mere  $\sim 30$  kpc apart. Unlike the two protocluster members reported in J21b, which are single sources at the resolution of the NOEMA and SMA data, these galaxies may be in the early to middle stages of a merger.

• In summary, this newly-confirmed protocluster contains three luminous SMG systems and an unknown number of optically-selected galaxies and fainter SMGs, all near the apparent peak epoch of SMG activity in the universe. As noted in Chapters 4 and 5, several triggering and quenching mechanisms have been put forward as the processes that govern the lifetime of an SMG and the growth of massive galaxies (e.g., merger activity (Toft et al. 2014) or accretion of fresh gas (Tadaki et al. 2018)). The relative abundance of dusty starbursts in this field will help astronomers differentiate the relative importance of each of these processes. Future analyses of the SMGs and their possible triggering and quenching mechanisms might include comparisons of their gas depletion timescales, outflow rates, or their stellar and gas/dust morphologies.

#### References

Casey, C. M. 2016, ApJ, 824, 36

Fletcher, T. J., Tang, M., Robertson, B. E., et al. 2019, ApJ, 878, 87

Jones, L. H., Barger, A. J., Cowie, L. L., et al. 2018, ApJ, 862, 142

Jones, L. H., Barger, A. J., & Cowie, L. L. 2021a, ApJ, 908, 222

Jones, L. H., Rosenthal, M. J., Barger, A. J., & Cowie, L. L. 2021b, ApJ, 916, 46

Oesch, P. A., Montes, M., Reddy, N., et al. 2018, ApJS, 237, 12

Sobral, D., Mathee, J., Best, P. N., et al. 2015, MNRAS, 451, 2303

Songaila, A., Hu, E. M., Barger, A. J., et al. 2018, ApJ, 859, 91

Smith, B. M., Windhorst, R. A., Cohen, S. H., et al. 2020, ApJ, 897, 41

Toft, S., Smolčić, V.; Magnelli, B. et al. 2014, ApJ, 782, 68

Tadaki, K., Iono, D., Yun, M. S., et al. 2018, Nature, 560, 613

Taylor, A. J., Barger, A. J., Cowie, L. L., et al. 2020, ApJ, 895, 132

Taylor, A. J., Cowie, L. L., Barger, A. J., et al. 2021, ApJ, 914, 79